

ROBUST STATOR INSULATION PROGNOSIS TECHNIQUE FOR
INVERTER-DRIVEN MACHINES

By

William Robert Jensen

A DISSERTATION

Submitted to
Michigan State University
in partial fulfillment of the requirements
for the degree of

Electrical Engineering - Doctor of Philosophy

2019

ABSTRACT

ROBUST STATOR INSULATION PROGNOSIS TECHNIQUE FOR INVERTER-DRIVEN MACHINES

By

William Robert Jensen

Stator insulation degradation is one of the most common causes for failure in an electric machine. As wide bandgap device become more popular for inverter topologies, electrical stress increases and insulation failure becomes a more significant concern. Short circuits formed from degraded insulation can quickly lead to a catastrophic failure. A technique to detect when insulation is degraded, well before the formation of a short circuit, allows the machine to be safely powered-down. In this work, an online technique to detect insulation degradation and provide a failure prognosis is proposed. The proposed technique does not require high-frequency sampling or additional sensors as these requirements are costly. Accelerated thermal degradation of stator insulation is performed experimentally and the results show a trend in the measured current that can be used for prognosis.

Inverter switching devices also degrade over their lifetime. A switching device that experiences gate oxide degradation produces features in the measured current that can mask changes due to insulation degradation. In this work, an online technique to detect gate oxide degradation in inverter switching devices is proposed. Accelerated gate oxide degradation of silicon and silicon-carbide MOSFETs shows that there are two features in the current that appear as the device degrades. Experimental results verify that one of the features in the current can be detected using steady-state voltage commands. Detecting degradation using quantities that are already calculated in the controller eliminates the need for additional sensor or high-frequency sampling.

An algorithm to improve the robustness of the insulation failure prognosis is proposed. As gate oxide degradation can mask insulation degradation, it can also lead to an underestimation of remaining useful life. Also, as there are many sources of stress that degrade insulation, a change in the rate of degradation due to differences in applied stress or in the insulation system can significantly impact the insulation lifetime. The proposed technique improves robustness of the insulation failure prognosis by first separating between insulation and switching device degradation. Once it is determined that the insulation is degrading, the remaining useful life is predicted using the proposed algorithm that is robust to varying rates of degradation as well as variations in the insulation system. Data sets from experimental insulation degradation are used to compare the accuracy and robustness of the proposed stator insulation prognosis algorithm.

To my wife Gabriela and parents Jan and Steve

ACKNOWLEDGMENTS

I would like to express my sincere appreciation to Dr. Shanelle Foster, whose constant guidance, advice and motivation made it possible for me to complete my PhD and helped me develop as an engineer and researcher. I also want to wish a special thanks Dr. Elias Strangas, Dr. Bingsen Wang and Dr. Guoming Zhu for their insights and guidance to improve the quality of this dissertation.

I would like to thank to my colleagues from the Electrical Machines and Drives Laboratory, Cristián López-Martínez, Dr. Reemon Haddad, Dr. Andrew Babel, Dr. Rodney Singleton, Anmol Aggarwal, Shaopo Huang, Orwell Madovi, Tiraruek Ruekamnuaychok, Steve Hayslett, Matt Meier, Shubham Shedge, Prathima Nuli, Ibrahim Allafi, Tia Smith, Josh Ward and Heinrich Eickhoff. This work would not be possible without their advice and assistance. I would like to offer a special thanks to Thang Pham, whose generous assistance was instrumental for me to complete this work. I also want acknowledge Dr. No-mar González-Santini, Dr. Ameer Janabi, Dr. Allan Taylor and Dr. Ujjwal Karki for the assistance they provided.

I would also like to thank Brian Wright, Meagan Kroll, Laurie Rashid, Roxanne Peacock, Gregg Mulder and Michelle Stewart from the ECE department at Michigan State University for all of their assistance.

Additionally, I want to thank the James Dyson Foundation for their financial support during my study.

I want to express my deep gratitude to my parents Jan and Steve, siblings Ben and Bonnie for their strong support and assistance for me in preparing this work. I also want to express my appreciation to my father-in-law Jesús and mother-in-law Eloísa, as well as

Jesús, Patricia, Anamaría and Jorge, for their encouragement and support.

This work, and all of my studies, would not have been possible without the love, patience and much-needed support from my wife Gabriela. Her encouragement was crucial in completion of this work. I also want to thank Enzo, for providing comfort as I completed this work.

TABLE OF CONTENTS

LIST OF TABLES	ix
LIST OF FIGURES	xii
KEY TO ABBREVIATIONS	xviii
Chapter 1 Introduction	1
1.1 Objectives and contributions	2
1.2 Organization	4
Chapter 2 Insulation Degradation	5
2.1 Insulation model	9
2.2 Simulation results	14
Chapter 3 Insulation Degradation Detection Technique	17
3.1 Proposed technique	20
3.2 Experimental setup	22
3.2.1 Simulated degradation	22
3.2.2 Accelerated thermal degradation	23
3.2.3 Machines under test	26
3.2.4 Failure criteria	28
3.2.5 Data acquisition	29
3.3 Experimental results	32
Chapter 4 Online Gate Oxide Degradation Detection	36
4.1 Background	36
4.2 Current Techniques	38
4.3 Effects of gate oxide degradation	40
4.4 Accelerated degradation test	42
4.4.1 Test bed	43
4.4.2 Effects of gate oxide degradation	46
4.5 Proposed technique	52
4.6 Online detection experiment	55
4.6.1 Experimental setup	58
4.6.2 Results with simulated degradation	60
4.7 Detection at higher switching frequencies	62
Chapter 5 Robust Insulation Failure Prognosis Algorithm	65
5.1 Background	65
5.1.1 Extended Kalman Filter	67

5.1.2	Particle Filter	69
5.2	Prognosis	73
5.2.1	Metrics of accuracy	76
5.2.2	Results	78
5.2.3	Computational effort analysis	81
5.2.4	Reduced sampling rate	83
5.3	Evaluation of robustness	84
5.3.1	Inaccurate training data	85
5.3.2	Varying rate of degradation	87
5.3.3	Different insulation system	88
5.4	Failure threshold	89
5.5	Proposed prognosis algorithm	91
Chapter 6 Fault Separation		96
6.1	Proposed technique for fault separation	96
Chapter 7 Conclusion and Future Work		101
Bibliography		104

LIST OF TABLES

Table 2.1	Thermal class designations for insulation systems	6
Table 2.2	Parameters of the insulation machine modeled	15
Table 3.1	List of standard insulation tests with their drawbacks	18
Table 3.2	Ratings of PMSM used to collect leakage current measurements . . .	22
Table 3.3	Operating point at which leakage current is measured	22
Table 3.4	Number of turns between different labeled terminals	23
Table 3.5	Component operating parameters used in analog peak detector circuit	26
Table 3.6	Ratings of the machines used in accelerated thermal degradation testing	27
Table 3.7	Visible geometric differences between the stators and insulation in the two batches of motors used in accelerated degradation experiments where Batch 2 motors are the higher efficiency designs	28
Table 3.8	Temperatures and duration applied for accelerated thermal degradation tests	33
Table 3.9	Sampling rate of oscilloscope to measure current across in-series resistor and to measure output of peak detector circuit	35
Table 4.1	Values of parameters used in simulation	43
Table 4.2	Properties of the IRF520 power MOSFET and C3M0280090D SiC MOSFET	44
Table 4.3	Details of components and setup information for power Si MOSFET accelerated degradation testing	46
Table 4.4	Details of components and setup information for SiC MOSFET accelerated degradation testing	46
Table 4.5	Different load types and the features measured when the MOSFET applied voltage across each	46

Table 4.6	Experimental changes in turn-on transient characteristics from Si power MOSFET	50
Table 4.7	Table of SiC MOSFET results	51
Table 4.8	Simulated operating point for comparing calculated duty cycles with different delay times	57
Table 4.9	Experimental steady-state operating conditions	59
Table 4.10	Parameters of PMSM used for experimental validation	60
Table 4.11	Percent change in calculated duty cycle for each voltage vector with 100 <i>nsec</i> and 500 <i>nsec</i> delay added in high-side switch of phase A	61
Table 4.12	Percent change in calculated duty cycle for each voltage vector with 500 <i>nsec</i> delay added in high-side switch of specified phase	62
Table 4.13	Simulated operating point for comparing calculated duty cycles with different delay times	63
Table 4.14	Comparison of normalized change in duty cycles with different delay and switching frequency (f_s) simulated	64
Table 5.1	Initial trend parameters and settings used in EKF and PF to estimate RUL for Machines 2 and 3	79
Table 5.2	Accuracy of RUL estimated using EKF and PF for Machines 2 and 3	80
Table 5.3	Accuracy of last 25% of estimated RUL using EKF and PF for Machines 2 and 3	80
Table 5.4	Steps required to implement the EKF	81
Table 5.5	Steps required in implementing the PF	81
Table 5.6	Required memory to implement the EKF	82
Table 5.7	Required memory to implement the PF	82
Table 5.8	Comparison of EKF and PF computational cost with $N_s = 2379$	82

Table 5.9	Comparison of the rate of decrease from the peak-to-peak trend, positive peak trend and analog circuit output trend for the last 70 hours of life from Machine 4	84
Table 5.10	Accuracy of RUL estimated using EKF and PF without using accurate training data for Machines 2 and 3	85
Table 5.11	Accuracy of last 25% of RUL estimated using EKF and PF without accurate training data for Machines 2 and 3	87
Table 5.12	Accuracy of RUL estimated using EKF and PF for Machines 1 over the whole lifetime and the last 50% of life, where data sets from Machines 2 and 3 are used for training	88
Table 5.13	Accuracy of RUL estimated using EKF and PF for Machine 5 over the whole lifetime and the last 60% of life, where data sets from Machines 2 and 3 are used for training	89
Table 5.14	Accuracy of RUL estimated using EKF, PF and proposed algorithm for Machines 2 with and without accurate training data	92
Table 5.15	Accuracy of RUL estimated using EKF, PF and proposed algorithm for Machines 3 with and without accurate training data	93
Table 5.16	Accuracy of RUL estimated using EKF, PF and proposed algorithm for Machines 1 using data sets from Machines 2 and 3 as training . .	93
Table 5.17	Accuracy of RUL estimated using EKF, PF and proposed algorithm for Machines 5 using data sets from Machines 2 and 3 as training . .	95

LIST OF FIGURES

Figure 2.1	Effect of thermal stress on dielectric strength [1]	9
Figure 2.2	Effect of voltage stress on time to reach 5 th of 10 failures [1]	9
Figure 2.3	Simplified model of groundwall insulation between energized conductor in the stator slot and the grounded back iron	10
Figure 2.4	As insulation degrades, physical changes lead to a decrease in overall area of material around conductors	11
Figure 2.5	Transmission line model of one phase winding implemented in Simulink, where the capacitance and resistance to ground represents the insulation	11
Figure 2.6	Voltage measured from phase-to-ground at the terminal and near the neutral point in a simulated inverter-driven, three-phase winding . .	11
Figure 2.7	One of the several transmission-line models, used to represent a phase winding, used for analyzing the change in leakage current overshoot	12
Figure 2.8	Output shows varying overshoot magnitudes as ζ varies where input to system is step response	14
Figure 2.9	One slot of random-wound induction machine with insulation included	15
Figure 2.10	Simulated voltage applied to healthy and degraded winding insulation transmission line model and leakage current responses. Insulation impedance is decreased by 50% in this simulation.	15
Figure 2.11	Model of one phase winding with turn-to-turn insulation modeled as parallel resistance and capacitance	16
Figure 2.12	Leakage current transient response shows 3.57% decrease at voltage transient in simulation when turn-to-turn insulation impedance decreases by 50%	16
Figure 3.1	Winding schematic with 15nF capacitor inserted across 14 turns . .	23
Figure 3.2	Environmental chamber used to degrade the insulation where electrical connections can be made through the side of the chamber	25

Figure 3.3	Experimental setup for measuring leakage current	25
Figure 3.4	Experimental measurement setup with peak detector shown	26
Figure 3.5	Healthy images of insulation in machines from two different batches, where the winding and amount of insulation between the two batches are visually quite different	27
Figure 3.6	Images of missing insulation in Machine 1, where the lighter area in the winding is bare copper, after failure	29
Figure 3.7	Leakage current measurement on left, where zooming in and examining the leakage current at the voltage rise on the right shows the transient oscillation and the extraction of the leakage current overshoot, I_{leak}	30
Figure 3.8	Raw signal and signal after noise is removed from experimental leakage current of machine with healthy insulation	30
Figure 3.9	Insulation current overshoot at different levels of thermal degradation where a decrease in the peak-to-peak value is measured	31
Figure 3.10	Output signals from the leakage current measured across an in-series resistor and the analog peak detector	31
Figure 3.11	Experimental measurement of leakage current with and without an additional $15nF$ capacitor inserted between turns	32
Figure 3.12	Trend in leakage current overshoot magnitude from healthy to failure in all nine machines	34
Figure 3.13	Trend in leakage current and peak detector output during testing of Machine 4	35
Figure 4.1	Illustration of physical effect of gate oxide degradation in MOSFET	37
Figure 4.2	Changes in turn-on transient voltages with gate oxide degradation .	38
Figure 4.3	Available current measurements in an inverter-driven machine. Leakage current to ground creates an imbalance in the three-phase currents.	40
Figure 4.4	Circuit used in simulation to quantify change in leakage current transient response with voltage applied at a variable dV/dt	41

Figure 4.5	Simulation result showing decrease in applied dV/dt to a motor phase causes a decrease in peak-to-peak overshoot in the leakage current. The green arrows indicate when the voltage reached its final value, showing the difference in rise time.	41
Figure 4.6	Gate-to-source voltage in healthy (subscript 1) and degraded (subscript 2) condition. With a higher threshold voltage, the time when the MOSFET is conducting, t_{on} , occurs further from the initial gate signal rise	42
Figure 4.7	Simulated circuit used to measure change in phase current rise as MOSFET threshold voltage increases	42
Figure 4.8	Change in threshold voltage leading to a delay in current rise with inductive load	43
Figure 4.9	HEF circuit to apply electrical stress to the gate of the MOSFET	44
Figure 4.10	Experimental circuit used to apply stress and measure transient characteristics by switching connections on MOSFET leads	45
Figure 4.11	Example signals collected from the oscilloscope before and after noise was removed	47
Figure 4.12	Gate-to-source voltage waveforms for healthy device and after several periods of HEF testing	47
Figure 4.13	Leakage current waveforms after several periods of HEF testing	48
Figure 4.14	Drain current vs V_{gs} to measure V_{th}	48
Figure 4.15	Delay in current rise after several periods of HEF testing	49
Figure 4.16	Current rise and V_{gs} from healthy and degraded SiC MOSFET where figure on right is zoomed-in view of green box area on left plot	50
Figure 4.17	LTSpice simulation using C3M0280090D model provided from Wolfspeed where the low DC voltage used is $5V$ and the high DC voltage is $900V$	51
Figure 4.18	Example current control diagram	52
Figure 4.19	SVPWM voltage vectors with $\alpha - \beta$ reference	55

Figure 4.20	Examining dead time in one phase leg of an inverter and how a delay in current rise can have an effect similar to additional dead time . . .	56
Figure 4.21	With additional dead time, or delay, in top side switch and positive current flow, the error in output voltage increases	57
Figure 4.22	SVPWM duty cycles from simulated machine with different delay added to high side switch of phase A	58
Figure 4.23	Gate signals to high and low side phase A switches used to add delay in turn-on to represent gate oxide degradation	59
Figure 4.24	V_{AB} voltage applied with and without a $100nsec$ delay and the resulting current in phase A. With an added delay, there is an increasing error in the current.	60
Figure 4.25	Normalized difference in controller-calculated duty cycles for all voltage vectors with delay added in high side switch of phase A	61
Figure 4.26	Comparing normalized duty cycle duration with same delay added to high side switch in all three phases where only phase A and B currents are measured	62
Figure 4.27	Normalized duration for each SVPWM voltage vector with different delay added to $A+$ switch at different switching frequencies	63
Figure 4.28	Output voltage decrease depends on the percentage of the switching period that the delay occupies	64
Figure 5.1	After initial estimates area made, this flow chart outlines the iterative process trajectory tracking using the EKF	69
Figure 5.2	General iterative particle filter process visually displayed where the dots represent one particle	73
Figure 5.3	RUL estimated using EKF compared to actual RUL from three sets of experimental data	74
Figure 5.4	Example cumulative distribution function used in re-sampling particles in PF process. A random value between 0 and 1 is sampled N times from the CDF and the particle associated with that value is added to the new population.	74

Figure 5.5	Example trend in leakage current overshoot with peak, failure threshold and estimated time of failure t_{EF} labeled	75
Figure 5.6	Process of estimating RUL where EKF or PF used to estimate β	76
Figure 5.7	Example PDF showing how confidence intervals are calculated from the distribution of t_{EF} calculated from each algorithm	78
Figure 5.8	RUL estimated using EKF and PF compared to actual RUL from two sets of experimental data with 20% confidence intervals provided	79
Figure 5.9	RUL estimated using EKF and PF compared to actual RUL from last 25% of actual lifetime with 20% confidence intervals shown	80
Figure 5.10	Prognosis comparison using peak-to-peak and positive peak magnitude from Machine 2	83
Figure 5.11	Machine 4 RUL from data collected from oscilloscope and analog circuit compared with the actual RUL	84
Figure 5.12	RUL estimated using EKF and PF compared to actual RUL from two sets of experimental data	86
Figure 5.13	RUL estimated using EKF and PF without accurate training data compared to last 25% of actual RUL with 20% confidence intervals provided	86
Figure 5.14	RUL estimated using EKF and PF compared to actual RUL of Machine 1 where data sets from Machines 2 and 3 are used for training	87
Figure 5.15	RUL estimated using EKF and PF compared to actual RUL of Machine 5 where data sets from Machines 2 and 3 are used for training	89
Figure 5.16	Highlighting the difference in leakage current overshoot trends between two machines with similar ratings and different insulation systems	90
Figure 5.17	Algorithm for the proposed prognosis algorithm where $X\%$ is 1% and t_x is the last two time steps	91
Figure 5.18	Comparison of proposed prognosis algorithm applied to Machine 2 data when accurate training is and is not available used to tune the algorithm	92

Figure 5.19	Comparison of proposed prognosis algorithm applied to Machine 3 data when accurate training is and is not available used to tune the algorithm	93
Figure 5.20	Proposed prognosis algorithm applied to Machine 1 using tuning from Machines 2 and 3, where Machine 1 degraded at a different applied temperature	94
Figure 5.21	Proposed prognosis algorithm applied to Machine 5 using tuning from Machines 2 and 3, where Machine 5 had a different insulation system	94
Figure 6.1	Effect that degrading switching device has on the RUL estimates from the EKF and PF	97
Figure 6.2	Effect injecting a 20% decrease in overshoot magnitude has on the RUL estimates from the EKF and PF. 20% is lower than the decrease that was found experimentally, and also shows a significant underestimation in RUL.	97
Figure 6.3	Proposed technique to improve the robustness of the insulation failure prognosis	98
Figure 6.4	V_{gs} from degraded switching device shows increase in Miller plateau as leakage current decreases	99
Figure 6.5	Switching device applying voltage across insulation of Machine 10 shows no significant change in Miller plateau voltage while the leakage current overshoot rises and decays, indicating that a healthy device and degraded insulation is present	100

KEY TO ABBREVIATIONS

EKF Extended Kalman Filter

RUL Remaining Useful Life

PF Particle Filter

CI Confidence Interval

WBG Wide Band Gap

HP Horse Power

HEF High Electric Field

MSE Mean Squared Error

PDF Probability Density Function

CDF Cumulative Distribution Function

FFT Fast Fourier Transform

Si Silicon

SiC Silicon-Carbide

IGBT Insulated Gate Bi-polar Transistor

MOSFET Metal-Oxide-Semiconductor Field-Effect Transistor

FEA Finite Element Analysis

PD Partial Discharge

SVPWM Space Vector Pulse-Width Modulation

PWM Pulse-Width Modulation

Chapter 1

Introduction

A growing interest in electrification across industries will lead to an increase in use of electric machines and drives. Electric machines are susceptible to a variety of different faults [2]. The majority of faults are found to occur in the stator. Around 25% of these stator faults are caused by degraded insulation in low-voltage machines. For high-voltage machines insulation degradation causes around 50% of the reported failures. There are many sources of stress that lead to short circuits and impact the lifetime of the insulation in an electric machine. The advent of wide bandgap (WBG) devices brings a concern to the reliability of insulation in inverter-driven machines as these devices add voltage stress to the insulation that reduces the lifetime by an unknown amount and leads to an increase in unexpected failures.

For some applications, maintaining or improving system reliability is critical. In these applications, sacrificing reliability for electrification is not acceptable. Systems require preventative maintenance and condition monitoring tests, where the machine is removed from operation, to avoid unexpected failures. Additional downtime for maintenance or repair in an application that operates continuously, such as manufacturing or drilling applications, is costly.

Online and non-invasive condition monitoring techniques are ideal as they detect degradation without additional measurements while the machine is in normal operation; thus avoiding additional downtime that an offline test requires. An online technique that does not require additional sensors or high frequency sampling is even more beneficial where such

additional requirements can make the cost of implementation prohibitively expensive.

1.1 Objectives and contributions

As insulation degrades, short circuits form. Regardless of their classification, all insulation systems are susceptible to the formation of short circuits and have a finite lifetime. Shorts can be found between two conductors, two phases or between the energized winding and the grounded back iron. Typically, short circuits begin between two conductors and tend to propagate quickly into a more serious, low-impedance short. Detecting an incipient fault and taking mitigating action can avoid failure [3]; however, more advanced knowledge of insulation degradation before a failure occurs is beneficial to schedule downtime for repair or replacement. In this work, an online technique to detect insulation degradation using measurements that are already available in an inverter-driven machine control system without high frequency sampling is proposed.

Inverters that employ WBG devices can operate at higher switching frequencies with lower in switching losses; and for that reason, WBG devices are becoming more common in inverter designs. However, WBG devices operate with shorter voltage rise and fall times that increase the dV/dt applied to the terminals of the machine and lead to an increase in the voltage stress on the insulation.

While WBG devices add stress to the insulation, these devices also degrade over their lifetime. Switching devices, WBG devices or not, are responsible for 34% of failures in inverter-drives [4]. Signatures in the current measurements that indicate switching device degradation mimic the signatures produced when insulation degrades [5]. When using electrical signals for detecting insulation faults or degradation, the ability to separate between

switching device and insulation effects adds robustness to the overall reliability assessment of the inverter-driven machine. In this work, an online technique to detect switching device degradation in an inverter-driven machine is proposed. In addition to the proposed online insulation and switching device degradation techniques, this work proposes a method to separate between degradation of the two components to achieve a more robust assessment of the insulation health.

While detecting degradation can provide the operator knowledge of an unhealthy component before it fails, a prognosis can provide an estimate of the remaining useful life (RUL). Predicting RUL allows the operator to adequately schedule when to properly power-down the machine before failure occurs. Accurate failure prognosis improves reliable operation of electric machines; however, the prognosis needs to be robust to variability of applied stress during operation and different insulation systems. In this work, a robust, online insulation failure prognosis technique for inverter-driven machines is proposed.

From the stated objectives, the contributions of the proposed work are:

1. A technique for online insulation failure prognosis at a reduced sampling rate and without additional sensors
2. An online technique to detect gate oxide degradation in inverter switching devices using voltage commands
3. A technique to separate between insulation degradation and switching device degradation using current measurements
4. An insulation failure prognosis algorithm that is robust to errors in training data, varying rates of degradation and variations in insulation systems

1.2 Organization

Background on insulation materials, sources of insulation degradation and a brief review of standard insulation condition monitoring tests are provided in Chapter 2. Additionally, an electrical model of insulation is provided for later development of a prognosis technique. Chapter 3 outlines the proposed online, non-invasive technique to detect insulation degradation. Current techniques from literature are reviewed and the advantage of the proposed technique is highlighted. Experimental results are used to validate the proposed technique. In Chapter 4, the online method to detect gate oxide degradation in inverter switching devices is presented. Background information on gate oxide degradation, current methods proposed for detecting gate oxide degradation and experimental results that illustrate the proposed precursors for detecting gate oxide degradation are provided. Algorithms to estimate insulation RUL are presented in Chapter 5. Each algorithm is applied to experimental data sets of insulation under accelerated thermal degradation. Accuracy and robustness of each algorithm is compared, and a more robust algorithm for insulation failure prognosis is proposed. Knowledge of the effects that gate oxide degradation and insulation degradation produce in the current measurements of an inverter-driven machine are combined in Chapter 6 to propose a process to improve the robustness of the insulation failure prognosis. Concluding remarks and notes on potential future work are provided in Chapter 7.

Chapter 2

Insulation Degradation

Stator insulation is categorized as conductor or groundwall insulation [6]. Conductor insulation isolates the winding conductors from each other while the groundwall insulation separates the energized conductors from the grounded case and back iron. All insulation materials in an electric machine need to be resistant to moisture and resilient against foreign contaminants and chemicals. However, each type of insulation has different desired characteristics. The required mechanical strength of the groundwall insulation is typically higher than that of the conductor insulation material. Groundwall insulation is between sharp iron edges of the stator slots and the conductors and therefore needs to resist being physically broken down from vibration forces generated during operation [7]. Conductor insulation is generally thinner than the groundwall insulation to fit more copper in the stator slots. As conductors in the same slot that are of the same phase do not have a large voltage difference, the insulation between these conductors can be thin. This insulation is also closest to the copper winding, which operates at the highest temperature, and therefore needs to be thermally conductive.

Based on the requirements, some of the most common groundwall insulation materials include mica, polyester film and aramid paper. Common conductor insulation materials include polyester or epoxy resins or varnishes.

Insulation materials have different maximum temperature limits, for continuous operation, that determine the thermal class rating. Different insulation thermal class definitions

Table 2.1 Thermal class designations for insulation systems

Class Designation	Maximum temperature ($^{\circ}C$)	Material
Y	90	-
A	105	-
E	120	-
B	130	Polyester film Mica with shellac binder
F	155	Epoxy and polyester resin Mica with epoxy binder
H	180	Mica with Silicon binder
-	200	-
-	220	Aramid paper
-	250	-

are provided in Table 2.1, and the common materials with maximum operating temperatures associated with that class are listed [6]. Most of the common materials are Class B, F, or H, where the aramid paper operates at higher temperatures.

Insulation degradation is caused by “TEAM” stresses, thermal, electrical, ambient and mechanical [7]. Ambient stress can be caused by debris or other abrasive particles from the environment or cooling system reaching the insulation. High humidity or oil, from the bearings or cooling system, are also ambient stress that can chemically react with the insulation material and cause degradation. Oil, for example, can penetrate mica and cause it to separate. Moisture, when combined with an elevated temperature, causes some insulation materials to break down. Materials within -ester groups, such as Mylar polyester, or -imide groups, such as Kapton polyimide, are prone to hydrolysis [6, 8]. Mechanical stresses are caused by the forces experienced in the machine during operation. These forces create vibrations that can cause loose conductors to move and lead to increased wear on the insulation. The rate at which ambient and mechanical stress degrade insulation, however, is not as well understood.

Thermal stress in addition to mechanical stress accelerates degradation. Thermal cycling causes the insulation and stator iron material to expand and contract, where the rate of thermal expansion is different in the two materials. This thermal expansion along with vibrations leads to physical breakdown of insulation in the stator slots.

Thermal stress creates oxidation and cross-linking, chemical processes that occur above a certain threshold temperature [9]. High temperature weakens chemical bonds in the insulation material to the point of breaking. Oxidation occurs when oxygen joins the insulation's polymer chain at the broken bond. Cross-linking is when other molecules or polymers join at the broken bond. Each process makes the insulation more brittle, and any layered insulation will lose its bonding strength and deteriorate. The change in insulation lifetime due to thermal stress is generally represented by an Arrhenius model, shown in Equation (2.1) [10]. However, at a lower temperatures, below the threshold for oxidation, no significant thermal degradation occurs [11].

$$k = Ae^{\frac{E_a}{RT}} \quad (2.1)$$

Partial discharges (PDs) are one of the most common causes of electrical stress on insulation. A PD is a spark that occurs in air pockets or on the surface of the insulation. In this process, electrons and ions bombard the insulation. For insulation made of organic materials, the electrons and ions cause chemical bonds to break and slowly deteriorate the insulation.

Similar to PDs, voltage surges applied on the phase terminals create electrical stress on the insulation. Inverter pulse-width modulation (PWM) pulses create this stress, even in low-voltage machines. The voltage pulses cause electrons from surface imperfections on the

copper conductors to pass into the insulation. Over time, this process causes enough bonds in the insulation to break and the insulation to fail.

The risk for insulation failure to occur from electrical stress increases when WBG devices are employed in an inverter-drive. WBG devices have a short voltage rise time which increases the applied dV/dt to the load. Higher voltage stress caused by the WBG devices in the inverter-drive can decrease the lifetime of the insulation by an unknown amount of time. WBG devices can operate at higher frequencies; however, high frequency does not significantly degrade insulation [12]. While high frequency switching may be implemented with WBG devices, the increase in terminal voltage from the quicker voltage rise degrades the insulation more significantly than the frequency.

Insulation material datasheets typically provide information regarding the change dielectric strength at different operating temperatures. A decrease in dielectric strength from thermal degradation can lead to earlier failure when WBG devices used as switching devices in an inverter-driven machine. WBG devices apply voltage with quicker rise times which causes higher voltage stress on the insulation with lower dielectric strength. An example plot is shown in Figure 2.1. The curve shown is from the datasheet of Nomex 410 insulation paper, as it is a common insulation material used [7]. The decrease in dielectric strength with temperature is logarithmic, represented by Equation (2.2).

$$\text{Dielectric Strength} = 10^{\left(\frac{8262}{273+^{\circ}C} - 11.44\right)} \quad (2.2)$$

Voltage across the insulation, along with temperature, have a significant effect on lifetime [12]. Changes in insulation lifetime due to voltage stress is also specified on the material datasheet. The effect of voltage stress on operating lifetime for Nomex 410 is provided in

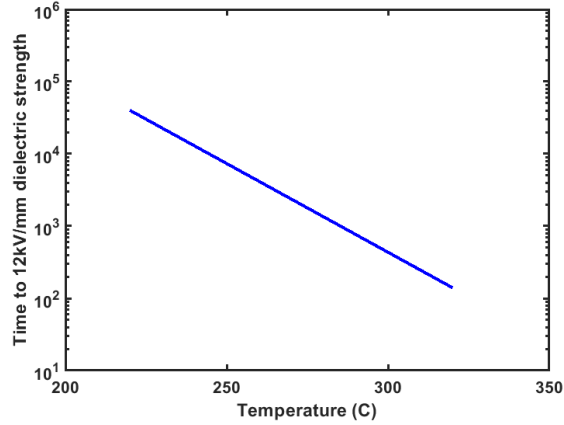


Figure 2.1 Effect of thermal stress on dielectric strength [1]

Figure 2.2 [1].

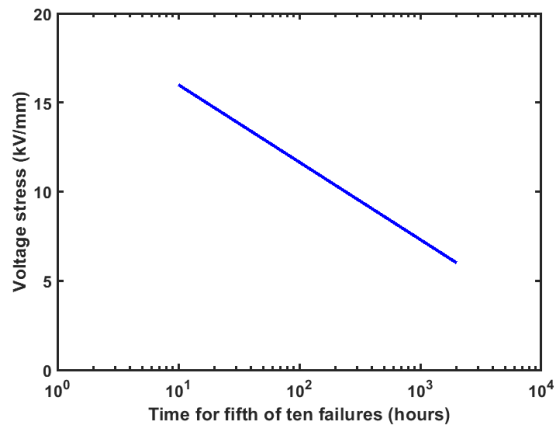


Figure 2.2 Effect of voltage stress on time to reach 5th of 10 failures [1]

2.1 Insulation model

Insulation can be represented as an impedance, a resistance and capacitance, between two conductors. A simplified model of groundwall insulation is shown in Figure 2.3. Along with the dimensions of the insulation, the resistivity of the material determines the resistance and

the dielectric constant determines the capacitance value, shown in Equations (2.3) and (2.4).

$$C = \frac{A\epsilon_0\epsilon_r}{d} \quad (2.3)$$

$$R = \frac{\rho l}{A} \quad (2.4)$$

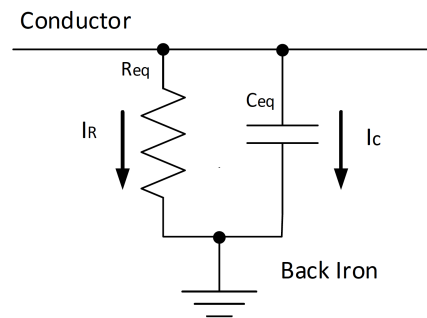


Figure 2.3 Simplified model of groundwall insulation between energized conductor in the stator slot and the grounded back iron

Physical changes as insulation degrades lead to a change in its equivalent impedance. Particulates and moisture evaporate from material when exposed to high temperatures, resulting in an overall decrease in material, shown in Figure 2.4. This can lead to change in capacitance, as described by Equation (2.3) where a decrease in area A decreases the capacitance. Generally, capacitance is known to decrease as insulation degrades. However, the capacitance will increase within 100 hours of high temperature exposure [11]. Other sources of stress, such as partial discharges or vibrations, that cause the insulation material to physically break also cause changes in the equivalent capacitance. The physical changes in insulation during degradation are directly related to the capacitance.

Winding impedance is represented as a series of transmission line models as shown in Figure 2.5. The impedance mismatch between the cables and motor winding along with a high dV/dt voltage pulse produces a significant reflected voltage at the terminals of the

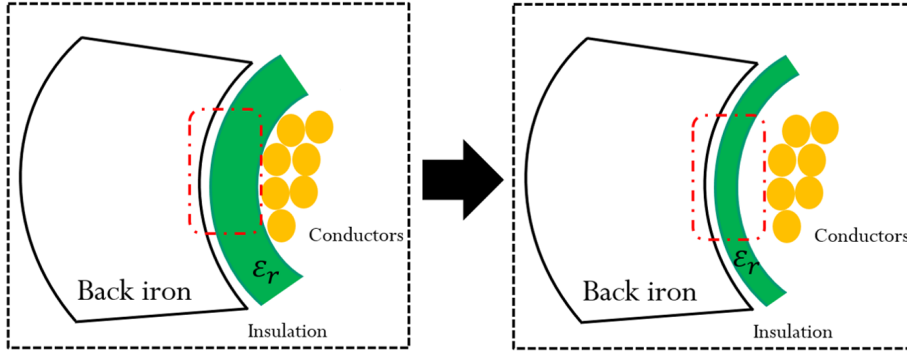


Figure 2.4 As insulation degrades, physical changes lead to a decrease in overall area of material around conductors

machine [13]. The reflected voltage is highest at the terminals and is distributed unevenly throughout the winding, as shown in Figure 2.6.

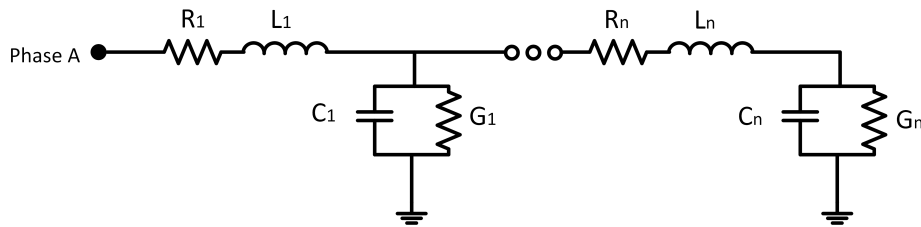


Figure 2.5 Transmission line model of one phase winding implemented in Simulink, where the capacitance and resistance to ground represents the insulation

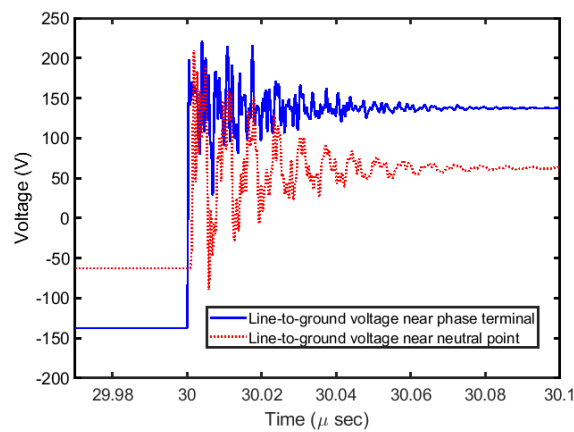


Figure 2.6 Voltage measured from phase-to-ground at the terminal and near the neutral point in a simulated inverter-driven, three-phase winding

Assuming that the applied inverter voltage can be represented by a step function, applied

to the transmission-line section shown in Figure 2.7, the transient response in the leakage current can be derived.

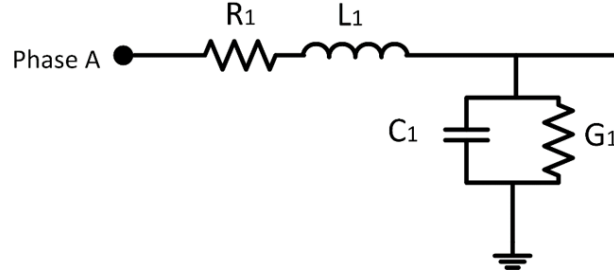


Figure 2.7 One of the several transmission-line models, used to represent a phase winding, used for analyzing the change in leakage current overshoot

The impedance of this model from phase to ground is derived in the Laplace domain as

$$Z = R_1 + sL_1 + \frac{\frac{G_1}{sC_1}}{G_1 + \frac{1}{sC_1}} \quad (2.5)$$

and can be simplified to obtain the impedance Z .

$$Z = R_1 + sL_1 + \frac{G_1}{sC_1G_1 + 1} \quad (2.6)$$

The current through this impedance is shown in Equation (2.7).

$$I = \frac{V}{Z} = V \frac{1}{R_1 + sL_1 + \frac{G_1}{sC_1G_1 + 1}} \quad (2.7)$$

The denominator can be represented as a second-order polynomial, the coefficients A_1 and A_2 are given in Equation (2.9) and Equation (2.10) respectively.

$$I = V \frac{1}{s^2 + A_1s + A_2} \quad (2.8)$$

$$A_1 = \frac{R_1}{L_1} + \frac{1}{C_1 G_1} \quad (2.9)$$

$$A_2 = R_2 + G_1 \quad (2.10)$$

The transfer function between the current and voltage, shown in Equation (2.8), can be represented as a general second-order transfer function given in Equation (2.11).

$$\frac{\omega_0^2}{s^2 + 2\zeta\omega_0 s + \omega_0^2} = \frac{1}{Z} \quad (2.11)$$

The damping term, ζ , is related to the overshoot in the transient response. Equation (2.12) gives ζ in terms of the transmission-line impedance, derived from Equation (2.7).

$$\zeta = \left(\frac{1}{C_1 G_1} + b_1 \right) b_2 \quad (2.12)$$

where

$$b_1 = \frac{R_1}{L_1} \quad (2.13)$$

and

$$b_2 = \frac{1}{2\sqrt{R_1 G_1}} \quad (2.14)$$

The damping term is inversely related to the overshoot magnitude, as shown in Figure 2.8.

Assuming that there are no other paths to ground present, the leakage current in the system is only current through the insulation. This indicates that the insulation capacitance and resistance are directly proportional to the overshoot magnitude in the leakage current. The overshoot magnitude at the switching transient in the leakage current can then be used as the signature to indicate degrading insulation.

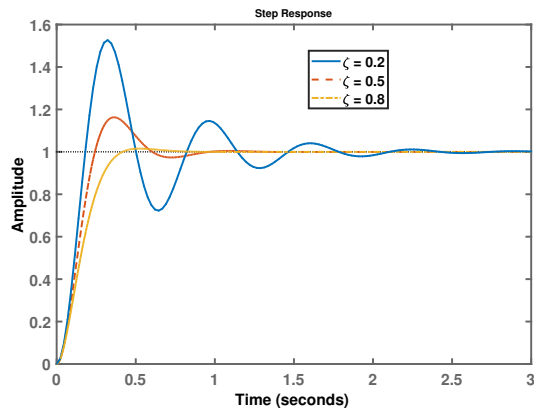


Figure 2.8 Output shows varying overshoot magnitudes as ζ varies where input to system is step response

2.2 Simulation results

A stator slot is modeled in electrostatic Finite Element analysis (FEA), Q3D extractor, shown in Figure 2.9. Ratings for the machine and parameters of the insulation materials used in simulation are provided in Table 2.2. The conductor coating and slot liner are included in the model. Although the number and location of conductors in the slot are not accurate, dimensions of the slot and conductors match the real machine. The capacitance and conductance between the conductors and the back iron from the simulation are used to approximate the impedance of the insulation used in the transmission-line model of one phase of a stator winding, shown in Figure 2.5. To mimic inverter excitation, DC voltage is applied across the transmission-line model using the voltage rise time from a MOSFET device provided in [14].

Capacitance and resistance values of the insulation in the transmission-line model are decreased to represent degraded insulation. Figure 2.10 shows the leakage current at the switching transient in the case of a healthy and unhealthy insulation model. When comparing the current waveforms, the magnitude of the overshoot in the transient response of the leakage

Table 2.2 Parameters of the insulation machine modeled

Parameter	Value
Voltage	460V
Power Rating	$\frac{1}{2}$ HP
Poles	4
Slots	24
Slot Linear Relative Permittivity (ϵ_r)	3.5
Slot Linear Bulk Resistivity	1×10^{12}
Wire Coating Relative Permittivity (ϵ_r)	3.6
Wire Coating Bulk Resistivity	1×10^{13}

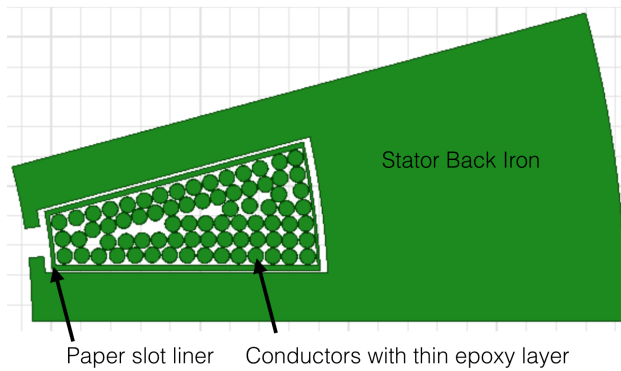


Figure 2.9 One slot of random-wound induction machine with insulation included

current decreases as the insulation degrades.

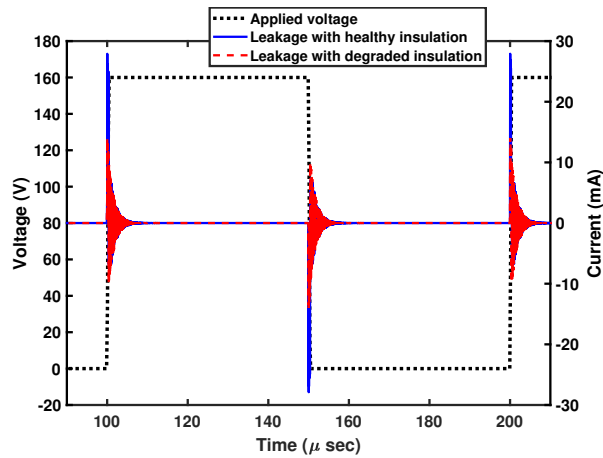


Figure 2.10 Simulated voltage applied to healthy and degraded winding insulation transmission line model and leakage current responses. Insulation impedance is decreased by 50% in this simulation.

The transmission-line model of the insulation is updated to include insulation impedance

between turns and phases [15], shown in Figure 2.11. Decreasing the capacitance and resistance of the turn insulation also produces a decrease in the magnitude of the transient overshoot, as shown in Figure 2.12. Detecting degradation of turn insulation in addition to degradation of groundwall insulation is ideal as turn-to-turn short circuits tend to occur before a short to ground.

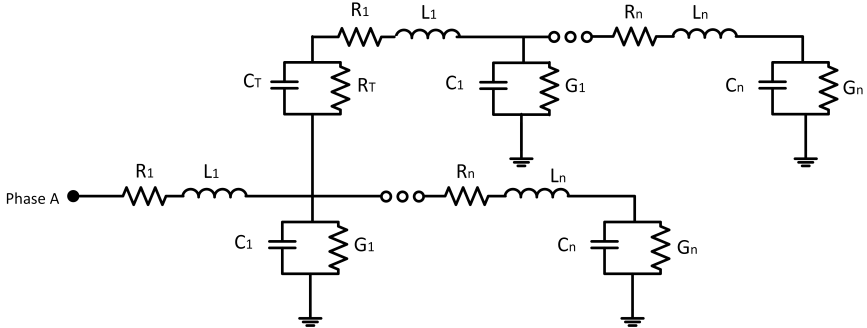


Figure 2.11 Model of one phase winding with turn-to-turn insulation modeled as parallel resistance and capacitance

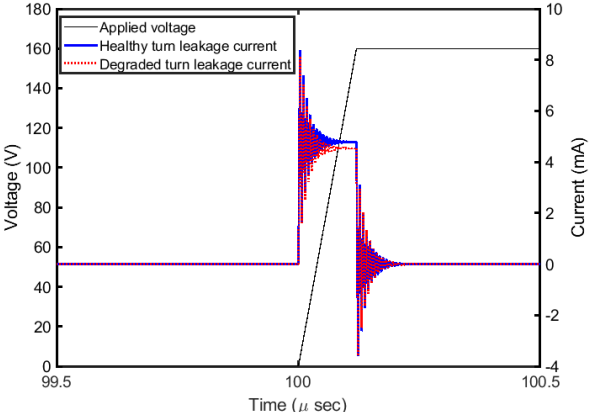


Figure 2.12 Leakage current transient response shows 3.57% decrease at voltage transient in simulation when turn-to-turn insulation impedance decreases by 50%

Chapter 3

Insulation Degradation Detection

Technique

There are several available standard tests that are commonly used for detecting insulation degradation. Some of these tests along with their drawbacks are provided in Table 3.1 [16–18].

Partial discharges are quick events that require special equipment to perform high-frequency sampling, which can be prohibitively expensive. However, measuring partial discharges is commonly used for detecting insulation degradation in high-voltage machines [17], performed offline or online. PD events are difficult to determine due to any noise present in the measurements [19]. Experience is required to establish a reliable threshold to distinguish a partial discharge event from measurement noise.

Due to the difficulty in accurately assessing the condition of the entire insulation system, some maintenance protocols combine tests to better decide when to replace or remove a machine from operation [20]. In such a protocol, tests to detect existing faults and assess the condition of the groundwall insulation are performed first, followed by tests to assess the phase-to-phase and turn-to-turn strength of the insulation. A failure threshold for these tests is set based on experience. The frequency at which these tests are performed is also set based on experience. While these maintenance protocols are robust methods to avoid unexpected failures, the tests involved do not provide a failure prognosis and require a significant amount

Table 3.1 List of standard insulation tests with their drawbacks

Test	Offline/Online test	Disadvantage
Winding resistance	Offline	Only detects existing shorts between turns
Inductive impedance	Offline	Only detects existing shorts between turns
Insulation resistance	Offline	Dependent on winding temperature
Surge test	Offline	Can be destructive
DC high potential	Offline	Can be destructive
AC high potential	Offline	Can be destructive
Polarization index	Offline	Performed offline
Dissipation factor	Offline	Performed offline
Temperature monitoring	Online	Requires additional sensors
Vibration monitoring	Online	Requires additional sensors
High frequency impedance	Online	Requires additional sensors
Air gap flux signature	Online	Requires additional sensors
Zero sequence voltage monitoring	Online	Requires access to neutral

of data and expertise to set a failure threshold.

Several non-standard online insulation condition monitoring techniques are present in literature. In [21], a technique that assess insulation quality using common mode current measurements is presented. High sensitivity current transducers, as described in [2], are used to measure phase currents. From the phase currents, the leakage current is calculated and the dissipation factor and capacitance of the insulation are calculated. Dissipation factor is the ratio of capacitive current to resistive current through the insulation and provides an indication of a change in the material properties. Degradation is detected from an increase in the dissipation factor or decrease in capacitance. While this technique is demonstrated to work well online, it requires special current transducers for accurate leakage current measurement.

A method to perform standard tests, such as Insulation Resistance and Dissipation Factor, to monitor the insulation health in an inverter-driven machine without disconnecting the machine is available [22]. This method uses the inverter to apply voltage that generates leak-

age currents to assess a change in the condition of the insulation. Measuring leakage current by sampling voltage drops over two measuring resistors at a high frequency can also provide information regarding the insulation health [23]. Detecting degradation in groundwall and phase-to-phase insulation separately, using Dissipation factor, resistance and capacitance, can also be performed online in an available technique [24].

A fast Fourier transform (FFT) of the common-mode voltage and leakage current are used to calculate the impedance of the insulation [25]. The dissipation factor and capacitance are calculated. Results of the capacitance trends show a consistent decay from healthy values at different rates of degradation.

An online method to monitor insulation degradation only using current measurements is introduced in [26]. This method samples phase current at 40Msa/sec and uses the amplitude spectrum for detecting degradation. An FFT is calculated from healthy insulation and used as a reference. A statistical indicator is calculated by comparing the amplitude spectrum of each current FFT. In [27], several thermal cycles are performed and the statistical indicator remains unchanged until failure occurs. Small changes in insulation capacitance can be detected using this statistical indicator. This method is noninvasive and uses available current measurements to detect insulation degradation.

These techniques are able to detect insulation degradation online in an inverter-driven machine; however, each has disadvantages. Some techniques require additional sensors or special, high-sensitivity sensors to detect the feature of degradation. Less-expensive sensors are explored for one technique, but results in inconsistent trends in the degradation feature [28]. High frequency sampling of current or voltage measurements is used in some techniques, which requires more expensive equipment. Experiments used to validate the available techniques are performed with simulated degradation in some cases. An FFT to

detect insulation degradation may not be the most robust feature. In addition to require high-frequency sampling, the frequency content in the voltage and current can be affected by other sources, such as a degrading switching device [5].

3.1 Proposed technique

An online method that does not require additional sensors or high frequency sampling to monitor insulation degradation is desired. The proposed technique meets these objectives where the magnitude of the peak-to-peak overshoot in the leakage current is the unique feature proposed to monitor insulation degradation. Monitoring insulation health using a peak-to-peak magnitude is advantageous over other features, such as an FFT, as it can be measured at a lower sampling frequency.

In an inverter-driven machine, phase currents are typically required for control. Industrial systems that employ three-phase machines may only use two current sensor to reduce the cost of measuring all three phase currents. In this case, the system is assumed to have balanced currents and the third current is calculated. However, as insulation degrades, the machine may no longer be in balanced operation and leakage current is present.

With current in all phases measured, both the phase and leakage currents are assumed to be available online. The sum of all phase current measurements is zero in a balanced system. Any non-zero sum is the leakage current as shown in Equation (3.1). When all phase currents are measured during operation, the summation of the currents provides the leakage current measurement online.

$$I_a + I_b + I_c = I_{leak} \tag{3.1}$$

In proposed technique, the leakage current feature for detecting degradation is only the peak-to-peak magnitude; analysis of the frequency content is not necessary. However, the required sampling rate to capture the peak magnitude of the leakage current overshoot may be significantly high for practical online implementation. In order to ensure the peak value is measured, Nyquist's sampling theorem requires that the signal needs to be sampled at two-times the frequency that is desired to be captured. Oscillation of the leakage current varies between machines as the impedance of the insulation, which determines the leakage current oscillation frequency, is not equal between machines. Regardless of the exact sampling frequency required for measuring the peak in a particular machine, reducing the required sampling rate is desired.

Reduction of the required sampling frequency using a low-cost analog circuit to measure the overshoot magnitude is proposed. Since only the peak value is required for detecting insulation degradation, holding this value for a longer duration allows for a sampling rate reduction to obtain the information required to detect insulation degradation. In this work, a circuit to follow a signal, detect when a peak is reached, and hold the peak value for a longer duration is proposed for online detection of insulation degradation.

Thermal degradation experiments are used to validate the ability of the proposed leakage current feature to monitor insulation health. Simulating degradation, by inserting capacitors between turns or ground, is used to demonstrates the difference expected change in the feature of degradation in other techniques. However, measuring the feature of degradation using applied stress provides the overall trend expected in the feature of degradation from healthy to failure. Measuring the trend where insulation is experiencing physical changes is a more realistic method to evaluate the proposed feature for detecting degradation.

3.2 Experimental setup

Two experimental setup are developed for measuring leakage current. A simulated degradation experiment is used to demonstrate the ability to measure leakage current online using current sensors. The second setup is to collect leakage current while insulation is thermally degraded from healthy to failure.

3.2.1 Simulated degradation

An inverter-driven permanent magnet synchronous machine (PMSM) operating at a steady state speed and current command is used to measure leakage current. Motor parameters and the experimental operating point are provided in Table 3.2 and Table 3.3 respectively.

Table 3.2 Ratings of PMSM used to collect leakage current measurements

Parameter	Value
Rated power	4.8kW
Rated torque	45Nm
Rated speed	750rpm
Rated voltage	480V _{ll}
Rated current	25A

Table 3.3 Operating point at which leakage current is measured

Operating point	Value
Speed	300RPM
Current	2.15A

In [26], insulation degradation is simulated by placing capacitors between turns in the winding. The increase in capacitance between turns creates an increase in the insulation capacitance. The selected PMSM has access to locations between different turns in the phase A winding. Table 3.4 lists the available number of turns between the different labeled point

Table 3.4 Number of turns between different labeled terminals

Terminals	Number of turns
AN1 to AN2	120
ANT1 to ANT2	15
ANM1 to ANM2	14
ANB1 to ANB2	1

in the phase A winding [29]. Leakage current is recorded without additional capacitance and with a $15nF$ capacitor inserted in parallel with 14 turns, as shown in Figure 3.1.

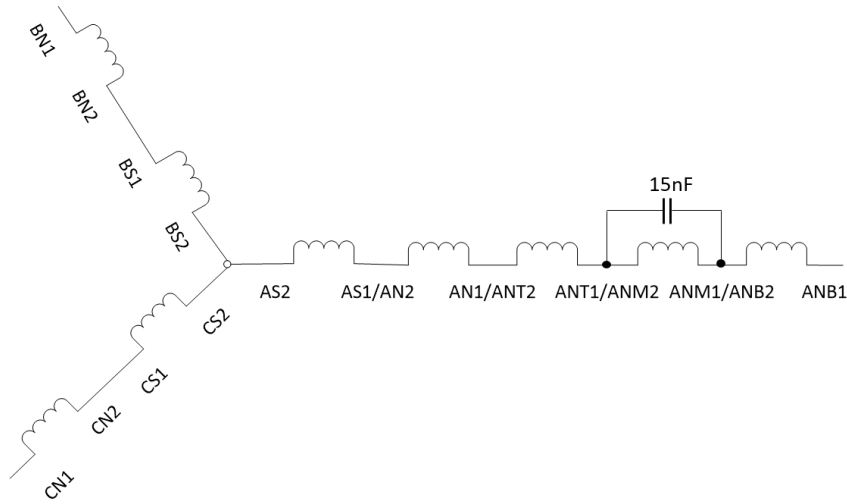


Figure 3.1 Winding schematic with $15nF$ capacitor inserted across 14 turns

An oscilloscope is used to measure the three-phase currents and the leakage current is processed from this data. The sampling rate on the oscilloscope used to measure this current is $500MHz$.

3.2.2 Accelerated thermal degradation

Accelerated degradation tests are performed to monitor the trend in leakage current overshoot as insulation degrades. Experiments are performed using the stator of a three-phase induction machine to evaluate insulation system of an electric machine. In these tests, the

machine is not in operation when leakage current is measured. Voltage is applied directly over the insulation and leakage current is measure directly.

The goal of the experiment is to apply high dV/dt voltage pulses, to mimic inverter excitation, and measure the leakage current at the switching transient while the insulation degrades. Thermal stress is selected to accelerate the degradation of the insulation. Other sources of stress, voltage, ambient or mechanical, are expected to decrease the equivalent resistance and capacitance of the insulation as well; which will produce a similar decreasing trend in leakage current overshoot. However, thermal stress is applied uniformly throughout the winding which is desired to achieve experiments that are repeatable.

Accelerated thermal degradation is expected to cause a decrease in insulation capacitance and resistance; however, an initial increase in overshoot magnitude is found to occur within 100 hours of thermal degradation [11]. This increase in capacitance can be caused by an initial volume increase from thermal expansion, as the material absorbs heat, or it can also be due to an increase in dielectric of the material due to an oxide layer forming at the interface of the copper and insulation. Other sources of stress may not cause the initial increase in leakage current overshoot but the decay is expected regardless of source of stress.

Tests are performed with the machine placed in an environmental chamber set to a high temperature. The end bells, bearings, rotor and shaft are all removed and only the stator of the machine is placed in the chamber, due to its limit size. Electrical connection can be made to the phase leads through the side of the chamber while it is set to a high temperature, as shown in Figure 3.2.

The experimental setup to apply voltage pulses and record leakage current is shown in Figure 3.3. One-phase, $120V_{rms}$ AC voltage is rectified to 160V DC and a MOSFET pulses this voltage to mimic inverter PWM excitation. The voltage is applied between one phase



Figure 3.2 Environmental chamber used to degrade the insulation where electrical connections can be made through the side of the chamber

lead and the case of the machine where the other two phase leads are open.

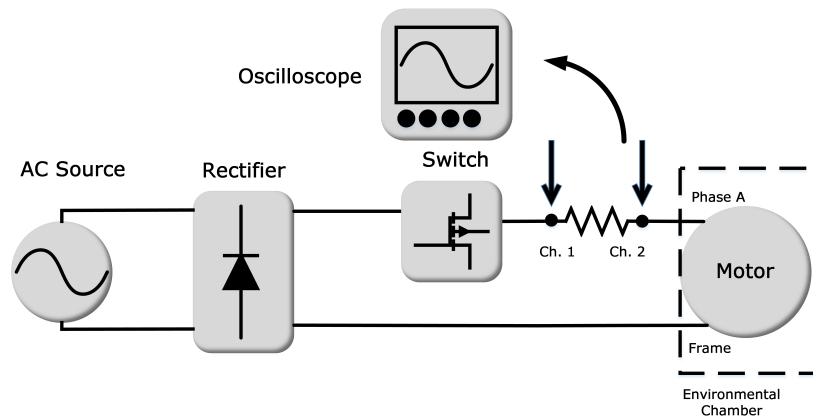


Figure 3.3 Experimental setup for measuring leakage current

The only path between phase and case is through the insulation, so the experimental setup directly measures leakage current. An oscilloscope is used to measure leakage current by measuring the voltage drop across a series resistor. Voltage pulses are applied continuously and the oscilloscope is triggered to save data every five minutes for the entirety of the test. As insulation degradation is a slow process, continuous sampling of leakage current is not

Table 3.5 Component operating parameters used in analog peak detector circuit

Component	Description
Op-amp slew rate	$900V/\mu sec$
Diode reverse recovery time	$4nsec$
Capacitor	$47pF$

necessary as a significant change in insulation health does not appear instantly.

An analog peak detector circuit that consists of an op-amp with a high slew rate, a diode and a capacitor is implemented during accelerated degradation testing, shown in Figure 3.4. The capacitor voltage is taken as the output of the peak detector circuit. The output is recorded and compared to the leakage current trend in order to determine if a lower sampling rate can be used to detect insulation degradation. Details regarding this circuit are provided in Table 3.5.

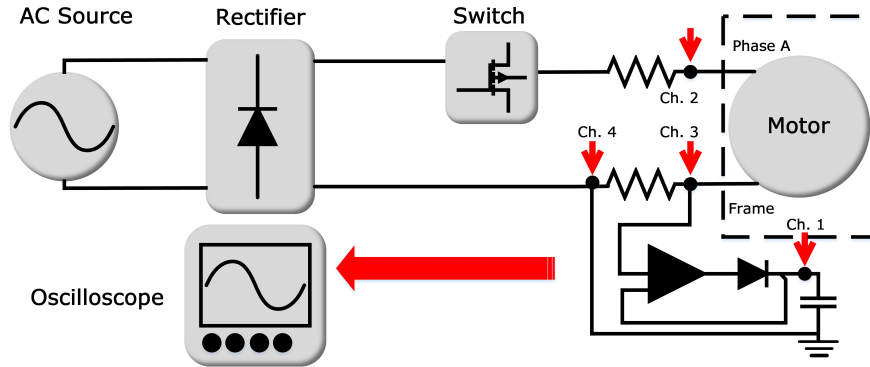


Figure 3.4 Experimental measurement setup with peak detector shown

3.2.3 Machines under test

Machines that fit in the environmental chamber are selected for accelerated degradation testing. Ratings of the selected machines are provided in Table 3.6. All of the machines are off-the-shelf and from the same manufacturer, but are not identical. Information regarding the insulation material in each machine is not available.

Table 3.6 Ratings of the machines used in accelerated thermal degradation testing

Parameter	Value
Power	1/2hp
Voltage	460V
Current	0.85A
Frequency	3450rpm
Insulation thermal class	F

Machines are from two different batches; four are from Batch 1 and the other five are from Batch 2. Visually, the insulation in the slot and end winding of the stator is different between the two batches of machines, as shown in Figure 3.5.

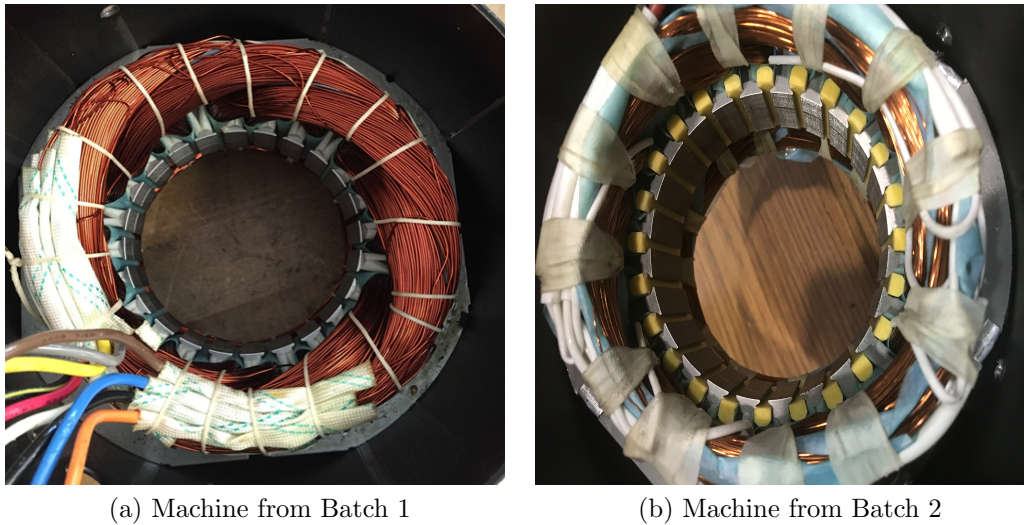


Figure 3.5 Healthy images of insulation in machines from two different batches, where the winding and amount of insulation between the two batches are visually quite different

Machines 5-9, from Batch 2, have conductors with smaller diameter, more insulation paper material separating the phases in the end winding and wedges in the slot near the air gap. Measuring some geometric parameters show that the diameter of the conductors from Batch 2 machines is 22.6% smaller than that of Batch 1, shown in Table 3.7. This measurement is of one conductor with the insulation included, so it is unknown if the conductor insulation is significantly different or if its just a smaller copper diameter that creates this

difference. Total slot area is also smaller in the Batch 2 machines, where the slot height is 26.7% smaller than the slot height of Batch 1 machines. With smaller conductor diameter, there may be the same number of turns in each slot even with the reduced slot size, but that is also unknown.

Table 3.7 Visible geometric differences between the stators and insulation in the two batches of motors used in accelerated degradation experiments where Batch 2 motors are the higher efficiency designs

Parameter	Batch 1 Value	Batch 2 Value
Slot height	16.46mm	12.07mm
Phase insulation thickness	0.25mm	0.15mm
Conductor diameter	0.53mm	0.41mm
Slot opening	2.74mm	2.41mm
End winding height	35.56mm	33.25mm

These geometric differences, along with the unknown difference in the materials, cause the insulation impedance to be different between the machines. It can also cause the rate at which the insulation degrades to differ between machines. Even changes in insulation properties that result from uniform applied thermal stress on identical test samples show a wide distribution [30]. Therefore, when insulation is not identical, the resulting impedance change between samples is likely to have a wide distribution.

3.2.4 Failure criteria

A daily visual inspection of the insulation is used to determine failure. Temperature of the environmental chamber is lowered to room temperature every day for this inspection and is set again to the high temperature if the insulation has not failed. Conventional insulation tests such as the High Potential or Surge test were not performed to determine failure, as these tests can cause significant degradation and premature failure. The only degradation

desired in these experiments is from high temperatures, for the tests to be repeatable.

Since the stator is the only part placed in the environmental chamber, and the end bells are removed, the conductors and insulation system are easily visible for inspection. Failure is determined in each machine by visually locating conductors with missing insulation. Figure 3.6 shows an image of the end winding of each machine where missing insulation is found.

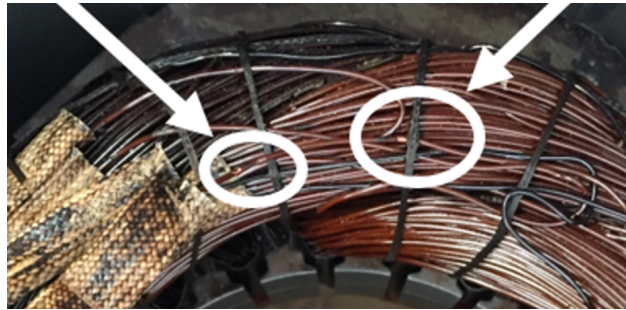


Figure 3.6 Images of missing insulation in Machine 1, where the lighter area in the winding is bare copper, after failure

3.2.5 Data acquisition

Nine machine stators undergo accelerated thermal degradation of the insulation and the trend in leakage current magnitude is obtained from each. The trend from healthy to failure consists of periodic measurements of the overshoot in the leakage current at the voltage rise time. The peak-to-peak value in the transient response of the leakage current, as shown in Figure 3.7, is taken as one data point.

Measurements from the oscilloscope contain a significant amount of noise. Wavelet de-noising is used to remove noise to obtain a smooth waveform for analysis without adding a phase shift, as shown in Figure 3.8. Daubechies 4 wavelet with 4 levels is selected for de-noising.

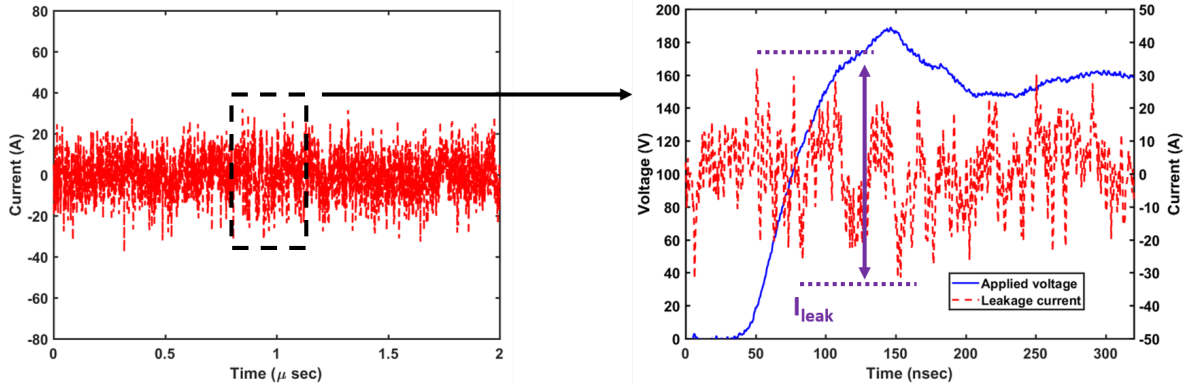


Figure 3.7 Leakage current measurement on left, where zooming in and examining the leakage current at the voltage rise on the right shows the transient oscillation and the extraction of the leakage current overshoot, I_{leak}

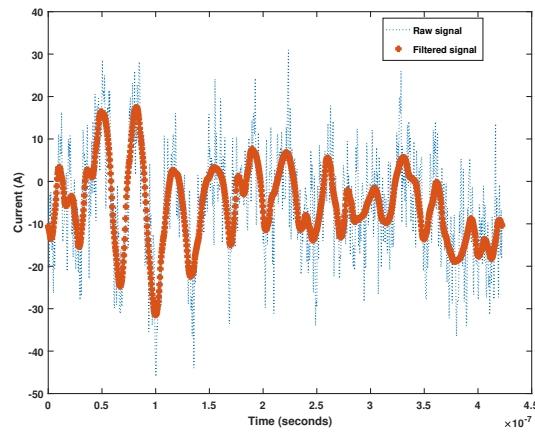


Figure 3.8 Raw signal and signal after noise is removed from experimental leakage current of machine with healthy insulation

After de-noising, the peak-to-peak magnitude of the overshoot in the transient response is the feature recorded to monitor degradation. A decrease in overshoot magnitude is found as the insulation degrades, shown in Figure 3.9.

The leakage current and peak detector output are each recorded using an oscilloscope with a high sampling rate. Figure 3.10 shows the waveform of the applied voltage, voltage across the in-series resistor and analog peak detector output. The peak detector output voltage increases in magnitude after the voltage pulse. The output voltage from the peak detector is not a DC value; rather, it increases as the voltage increases and decreases after

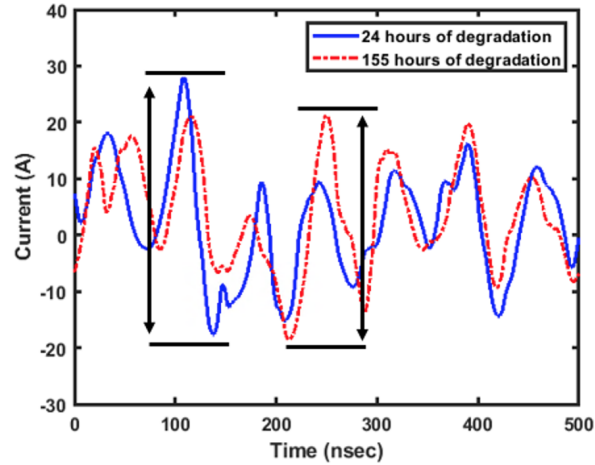


Figure 3.9 Insulation current overshoot at different levels of thermal degradation where a decrease in the peak-to-peak value is measured

the peak. As the peak detector circuit uses a capacitor on the output, the voltage level that is output depends on the size of this capacitor. A larger capacitance hold the output voltage longer without a significant decay; however, the larger capacitance charges slowly which results in a lower output voltage. Output from the peak detector shows that the increase in magnitude after the rise in the applied voltage is held for a sustained duration, shown in Figure 3.10, allowing for a lower sampling rate to measure the magnitude.

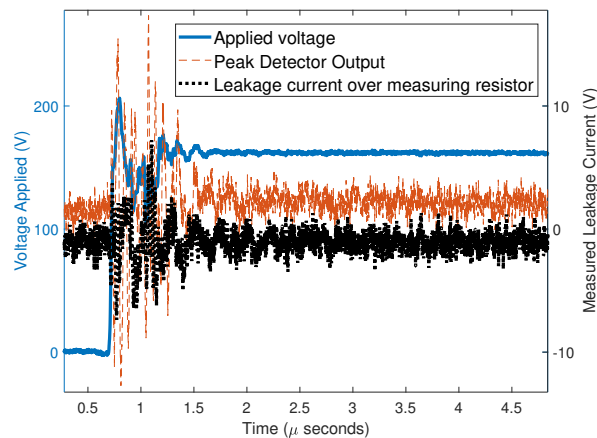


Figure 3.10 Output signals from the leakage current measured across an in-series resistor and the analog peak detector

The output of the peak detector is down-sampled at different rates in order to find the sampling rate that can show the same trend as the leakage current that is used to detect insulation degradation.

3.3 Experimental results

Simulated degradation by inserting a capacitance between produces a change in leakage current. The peak-to-peak overshoot in the leakage current with additional capacitance is larger than the overshoot without additional capacitance, shown in Figure 3.11. With this measurement technique, leakage current can be measured online to detect insulation degradation.

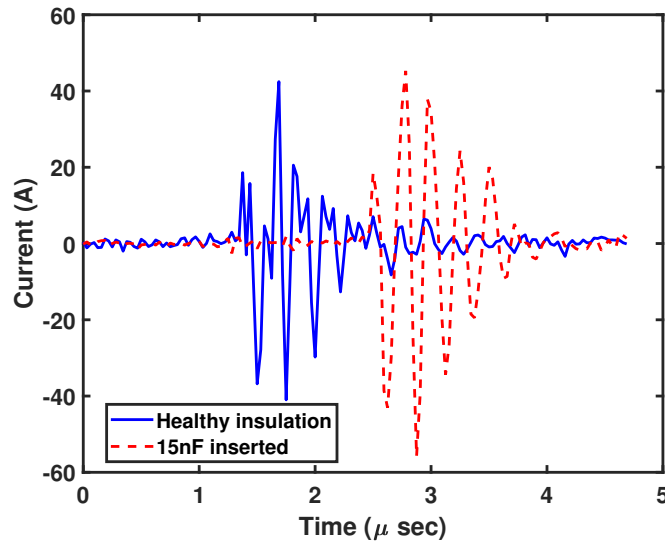


Figure 3.11 Experimental measurement of leakage current with and without an additional $15nF$ capacitor inserted between turns

The temperature and period of time that it is applied to each machine is provided in Table 3.8. Machines 1-4 are all from the same batch and the insulation in each machine is assumed to be similar. The same high temperature is applied to Machine 2 and 3 and the

time of failure is comparable. Machine 1 degraded at a lower temperature for a longer period of time and therefore has a higher time of failure. Machines 5-9 are from a different batch of machines that has differences in the insulation and geometry. These differences likely cause the significant difference in time to failure found in Machine 4.

Table 3.8 Temperatures and duration applied for accelerated thermal degradation tests

Machine	Applied temperature and duration
Machine 1	250°C for 488 hours
	260°C for 151 hours
Machine 2	260°C for 439 hours
Machine 3	260°C for 513 hours
Machine 4	260°C for 426 hours
Machine 5	260°C for 218 hours
Machine 6	260°C for 345 hours
Machine 7	260°C for 329 hours
Machine 8	260°C for 48 hours
	250°C for 235 hours
Machine 9	260°C for 20 hours
	250°C for 174 hours

Results generally show a similar trend in leakage current overshoot magnitude, as shown in Figure 3.12. In several machines, an initial rise in overshoot followed by a decay until the magnitude returns to a value near the healthy overshoot magnitude is measured. The resulting trend in overshoot magnitude from the machines is not a smooth exponential decay. However, the results show that the peak-to-peak value in the leakage current transient response can be used for detecting insulation degradation. The overall trend of reaching an initial peak followed by an exponential decay can be used for condition monitoring.

The peak detector is implemented in one accelerated degradation experiment and Figure 3.13 shows the last 70 hours of the leakage current overshoot measured from oscilloscope and from the output of the peak detector circuit. A comparison of sampling rate of the ana-

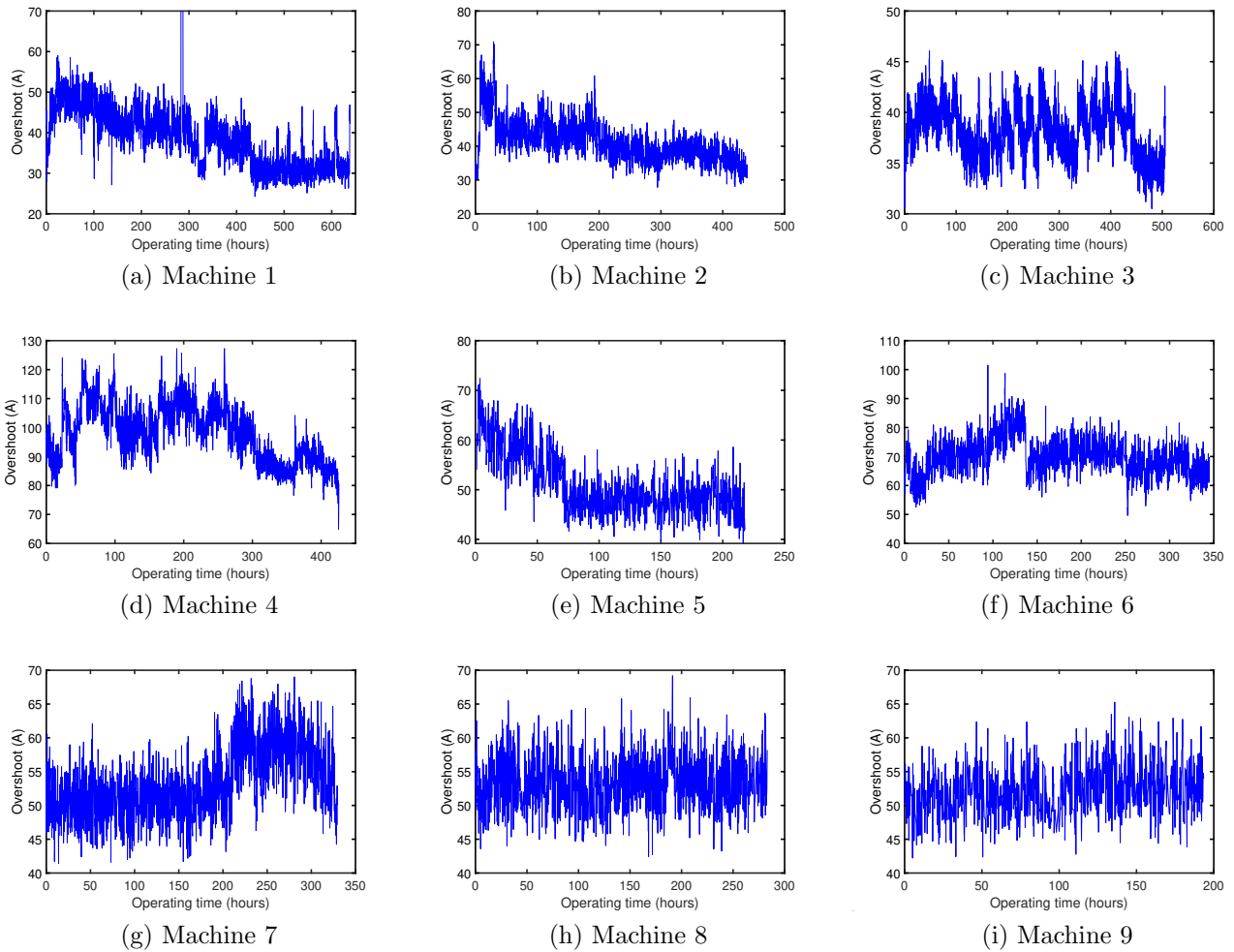


Figure 3.12 Trend in leakage current overshoot magnitude from healthy to failure in all nine machines

log peak detector output and the current through the in-series resistor, provided in Table 3.9, shows a significant reduction in the required sampling rate. A similar decay in magnitude until failure is shown in each measurement, indicating that the peak detector circuit can be used for detecting insulation degradation.

Table 3.9 Sampling rate of oscilloscope to measure current across in-series resistor and to measure output of peak detector circuit

	Sampling rate	Reduction
In-series resistor	1.0GHz	-
Analog circuit	10MHz	100×

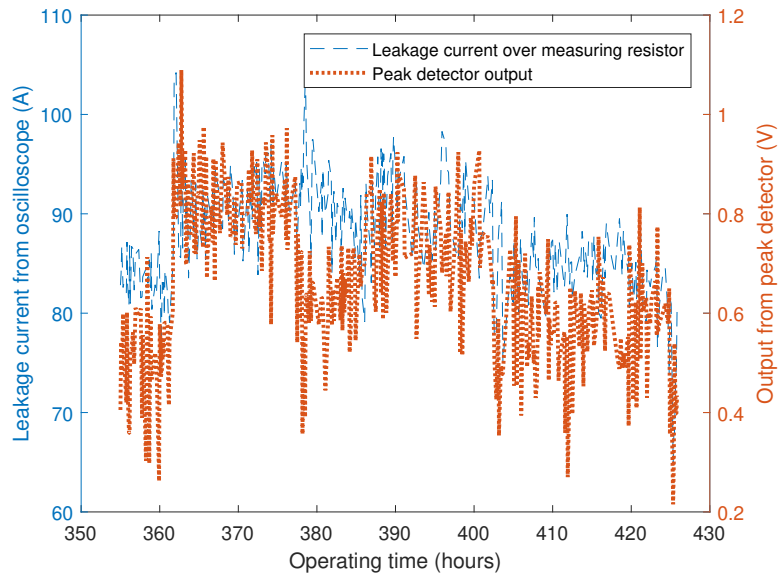


Figure 3.13 Trend in leakage current and peak detector output during testing of Machine 4

Chapter 4

Online Gate Oxide Degradation

Detection

There are reliability issues associated with the switching devices in an inverter-driven machine. Degradation of the gate oxide insulation layer occurs from excessive thermal or electrical stress in MOSFETs and IGBT switching devices [31,32]. As a result, the characteristics of the turn-on voltages of these switching devices vary as degradation progresses. An online technique to detect these turn-on transient changes in an inverter-drive is proposed. The technique detects gate oxide degradation in switching devices without additional sensors or high-frequency sampling.

4.1 Background

Although gate oxide degradation produces similar affects in MOSFETs and IGBTs, this work focuses on the affects in MOSFETs. Gate oxide degradation occurs slowly over the MOSFET's lifetime and is exacerbated by high temperature or high electric field stress [33]. In an N-type MOSFET, the device enters the on-state with a positive voltage between the gate and source, allowing current to flow, shown in Figure 4.1. Defects in the interface between the SiO_2 insulator and Si or SiC semiconductor layers, in the form of oxygen vacancies in the silicon lattice structure, cause negatively charged ions to become “trapped”

in this interface, as shown in Figure 4.1b [33,34].

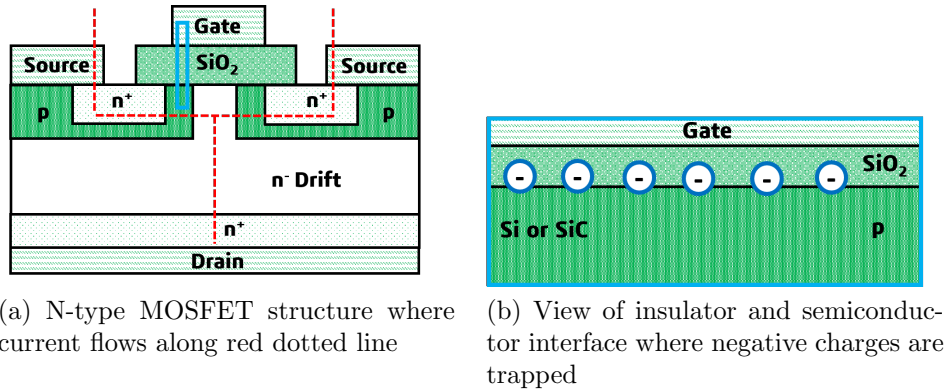


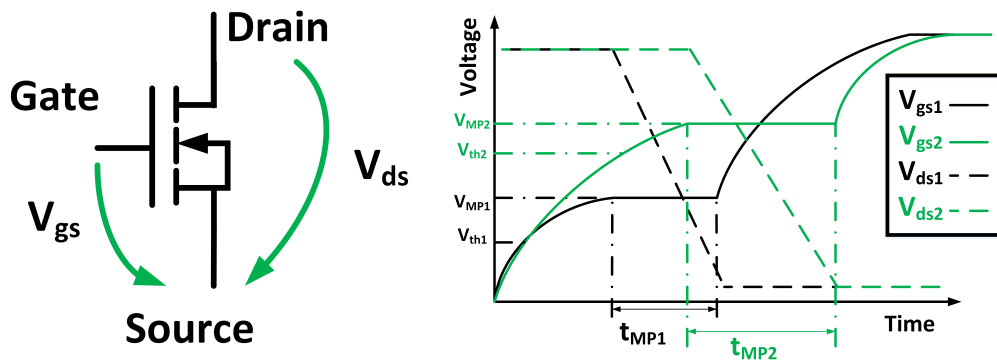
Figure 4.1 Illustration of physical effect of gate oxide degradation in MOSFET

In Si and SiC devices, the interface between the oxide and semiconductor near the gate is vulnerable to accumulating charged particles. However, gate oxide degradation occurs differently in Si and SiC MOSFETs. Si MOSFETs initially accumulate charge in the oxide layer [35]. A high positive electric field on the gate creates oxide-trapped positive charges. Negative charges then accumulate in the interface region. These two interactions cause the turn-on transient characteristics, such as threshold voltage, Miller plateau voltage and time, to decrease initially and then increase [36].

SiC MOSFETs do not accumulate charges in the oxide but in the defects in the near-interface oxide traps [34]. This is the region near the SiC-oxide interface. Defects in this region are well known and result in an accumulation of electrons near the gate. With only negative charges accumulating as a positive electric field is applied to the gate, the threshold voltage and Miller plateau voltage are found to increase with degradation. Over time, as the negative charge accumulates at the near-oxide interface in Si or SiC devices, the positive voltage required for the MOSFET to enter the on-state increases thereby increasing the threshold voltage (V_{th}) of the device.

Figure 4.2b shows typical MOSFET turn-on gate-to-source (V_{gs}) and drain-to-source

(V_{ds}) voltage waveforms for a healthy device and one that has degraded gate oxide. Over time, in both Si and SiC devices, the threshold voltage, Miller plateau voltage and duration increase, as shown in Figure 4.2b. The change in threshold voltage causes a delay in the current rise through the device. As the Miller plateau duration increases, the time it takes for V_{ds} to drop from the blocking voltage to the on-state voltage increases, which decreases the dV/dt of the voltage applied to the load.



(a) MOSFET voltage definitions (b) MOSFET turn-on transient voltage waveforms

Figure 4.2 Changes in turn-on transient voltages with gate oxide degradation

Inverters used for motor-drives commonly employ IGBT switching devices. IGBTs typically cannot achieve switching frequencies that MOSFETs can, but they typically have higher power ratings than Si MOSFETs and are cheaper than SiC MOSFETs. Gate oxide degradation also occurs in IGBTs, and similar changes in the V_{MP} , t_{MP} and V_{th} result [32].

4.2 Current Techniques

There are techniques available to detect MOSFET gate oxide degradation by measuring characteristics of device. However, they require removing the device from the circuit or additional sensors, invasive measurements or high frequency sampling.

Degradation of the gate oxide layer in Si and SiC devices can be detected through monitoring the on-state resistance, threshold voltage V_{th} , gate or drain leakage current and gate-to-source impedance [31, 34, 36–40]. Degradation in the gate oxide also changes some of the characteristics in the turn-on gate-to-source voltage (V_{gs}) such as the level and duration of the Miller plateau voltage [36]. While these characteristics can effectively indicate gate oxide degradation, they all require additional measurements and sensors that are not typically available in an inverter-drive application.

There are techniques proposed for online detection of gate oxide degradation. In [41], an analog circuit to monitor gate leakage current is proposed. A technique that measures on-state resistance online using an adjustable gate driver and an additional resistor to measure drain current is also available [42]. While each method can accurately measure robust precursors of gate oxide degradation while the MOSFET is in operation, they require additional hardware on each individual device as well as additional sensors. The additional requirements in these solutions may not be practical for all applications.

Current rise is discussed as a method to detect MOSFET gate oxide degradation in [43]. An analog circuit is developed to capture the gate signal and delay in current rise. This technique, however, would require additional circuits on each inverter switch. It also uses high frequency sampling in order to measure the delay time. In an inverter-driven machine, these additional requirements may not be practical for all applications where cost is a significant factor.

4.3 Effects of gate oxide degradation

An inverter-driven, current-controlled machine typically requires phase current sensors for control. It cannot be assumed that voltage or temperatures sensors are available to assist with diagnostics as these sensors are not required for operation and are not always available. Voltages and currents on the pins of each switching device also are not typically available as this requires an excessive number of additional sensors. It is more useful to detect gate oxide degradation in a feature of the phase current, since these measurements do not require additional sensors or invasive measurements. When current sensors are available on all phases, as shown in Figure 4.3, leakage current can be estimated.

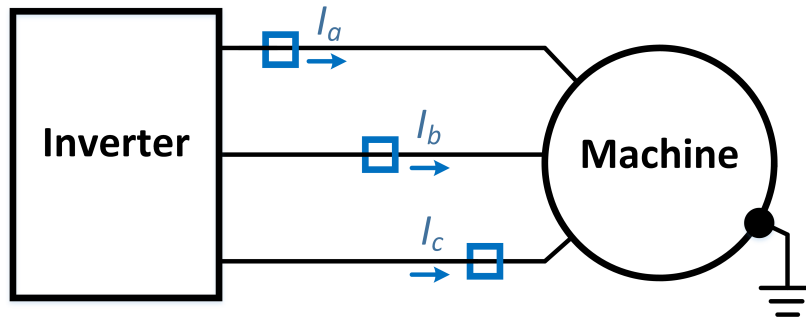


Figure 4.3 Available current measurements in an inverter-driven machine. Leakage current to ground creates an imbalance in the three-phase currents.

Gate oxide degradation in inverter switching devices leads to a couple of changes in features that are measurable in the phase currents. An applied voltage with high dV/dt creates a transient response in the leakage current. The leakage current takes a path to ground through parasitic impedance from the inverter or machine, shown in Figure 4.3. When the dV/dt of the applied voltage decreases, the overshoot magnitude of the leakage current transient response decreases. The circuit shown in Figure 4.4 models the current path from one phase terminal to machine ground. As shown in Figure 4.5, the change in the magnitude of the overshoot is found to be proportional to the change in the voltage rate of

rise.

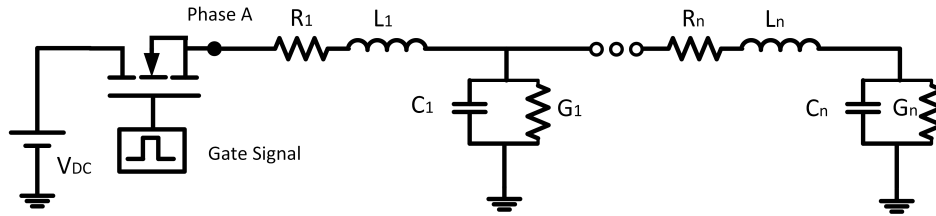
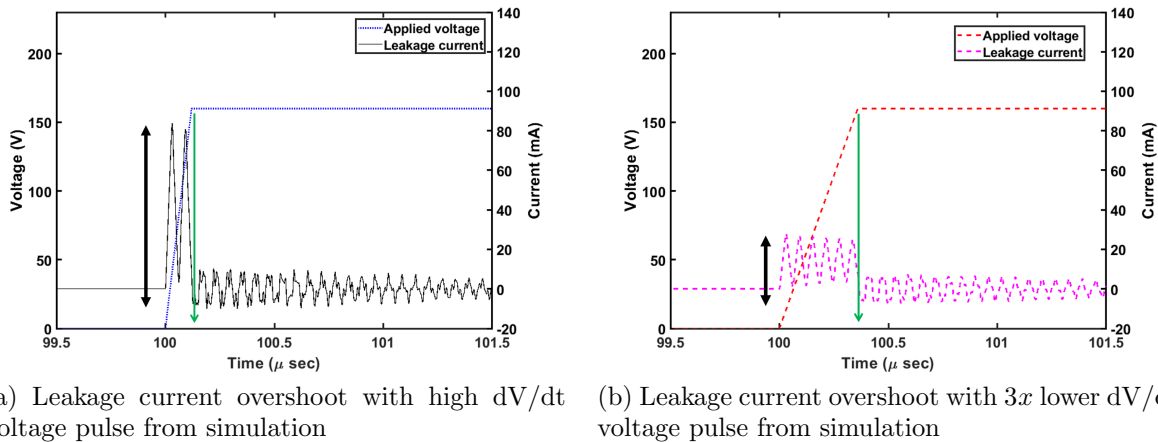


Figure 4.4 Circuit used in simulation to quantify change in leakage current transient response with voltage applied at a variable dV/dt



(a) Leakage current overshoot with high dV/dt voltage pulse from simulation (b) Leakage current overshoot with $3x$ lower dV/dt voltage pulse from simulation

The other feature in the phase current that is present when MOSFET gate oxide degradation occurs is a delay in the phase current rise. Switching device gate oxide degradation leads to an increase in threshold voltage. As the gate signal rises at the same rate, the time it takes to reach the larger threshold voltage increases, as shown in Figure 4.6. Current does not flow through the device until the threshold voltage is reached; therefore, the delay in reaching the threshold voltage creates a delay in the rise of the current to the machine phase.

The circuit in Figure 4.7 with passive component and voltage values listed in Table 4.1 are used to demonstrate the rise delay. The load models an inductive phase winding of an

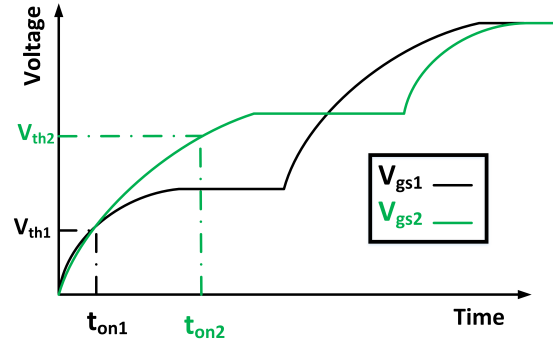


Figure 4.6 Gate-to-source voltage in healthy (subscript 1) and degraded (subscript 2) condition. With a higher threshold voltage, the time when the MOSFET is conducting, t_{on} , occurs further from the initial gate signal rise

electric machine. The threshold voltage of the simulated MOSFET can be modified. The device parasitic capacitance along with the gate resistance determine how quickly the gate voltage rises. To more accurately model the delay time, the gate signal rate of rise is found experimentally and used in the simulated model. The results show a $35nsec$ delay in the time when the current begins to flow through the load when the threshold voltage doubles from $4V$ to $8V$, shown in Figure 4.8.

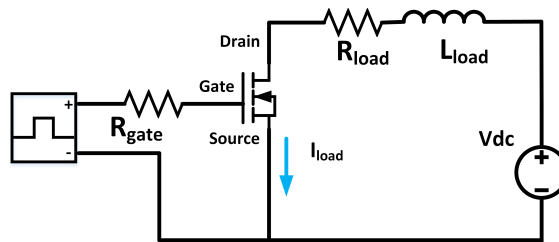


Figure 4.7 Simulated circuit used to measure change in phase current rise as MOSFET threshold voltage increases

4.4 Accelerated degradation test

SiC and power Si MOSFET devices are experimentally degraded to quantify changes in the turn-on transient current features. The IRF520 power MOSFET and C3M0280090D

Table 4.1 Values of parameters used in simulation

Parameter	Value
Gate resistance R_{gate}	10Ω
Phase resistance R_{load}	2Ω
Phase inductance L_{load}	$20mH$
Insulation capacitance C_{Ins}	$250 \times 10^{-12}F$
Insulation resistance R_{Ins}	$5 \times 10^5\Omega$

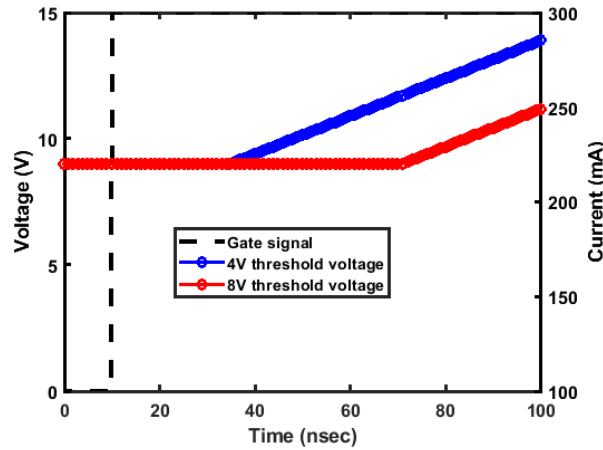


Figure 4.8 Change in threshold voltage leading to a delay in current rise with inductive load

SiC MOSFET devices, properties of each provided in Table 4.2, are selected for accelerated degradation testing [44, 45]. Stress is applied to the gate oxide and then the turn-on voltage and current waveforms are captured at different time intervals to evaluate changes. The phase-to-case connection from a real induction machine stator is used as the load for accurate leakage current measurement. Resistive and inductive loads are also used in order to capture device turn-on transient characteristics such as the Miller effect, threshold voltage and phase current rise time.

4.4.1 Test bed

The devices are degraded using a High Electric Field (HEF) circuit, shown in Figure 4.9. With this circuit, the drain and sources of the device are shorted and a voltage higher than

Table 4.2 Properties of the IRF520 power MOSFET and C3M0280090D SiC MOSFET

Property	IRF520	C3M0280090D
V_{DS}	100V	900V
$R_{DS(on)}$	0.27 Ω	0.28 Ω
I_D	9.2A	11.5A
Threshold voltage V_{th} range	2V – 4V	1.8V – 3.5V
Drain current when device in on-state	250 μ A	1.2mA
Turn-on delay	8.8nsec	26nsec
Rise time t_r	30nsec	10nsec
Input capacitance C_{iss}	360pF	150pF
Output capacitance C_{oss}	150pF	20pF
Reverse transfer capacitance C_{rss}	34pF	2pF

the rated gate voltage is applied between the gate and source.

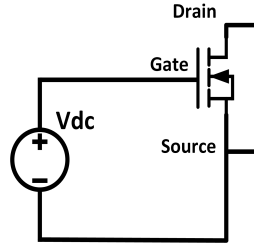
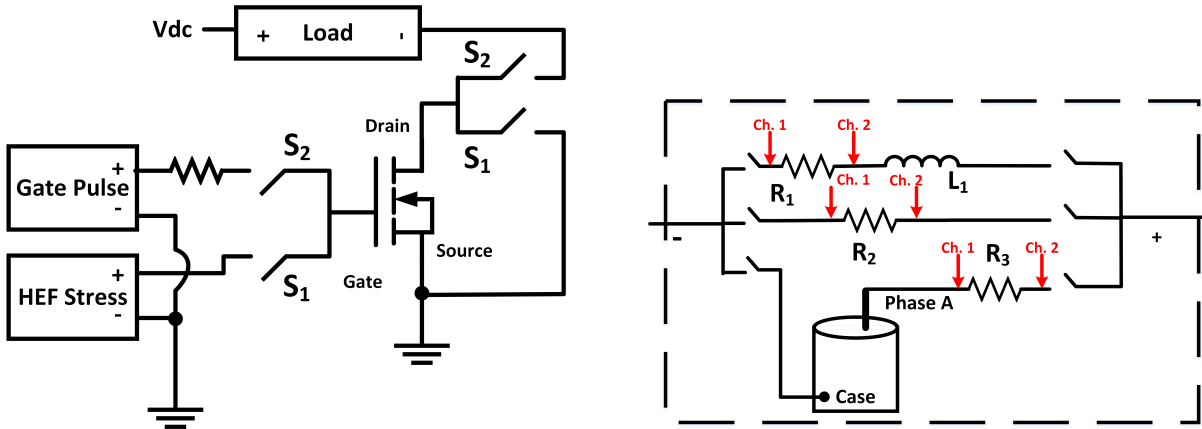


Figure 4.9 HEF circuit to apply electrical stress to the gate of the MOSFET

Electrical stress is selected to degrade the MOSFETs for repeatability. The devices are at ambient temperature during all periods of applied electrical stress. The applied voltage across the gate and source is selected to be 65V for the power Si MOSFETs as this voltage is found to degrade but not instantly damage gate oxide [36, 39]. A lower voltage, 37V, is selected to degrade SiC MOSFETs as these devices are more susceptible to gate oxide degradation due to their typically thinner oxide layer and larger number of defects in the oxide-semiconductor interface [34]. In addition to different voltages used to degrade the different devices, the HEF stress is also applied for a different duration when degrading each device in order to detect changes in the turn-on transient voltages and currents.

To measure the turn-on characteristics after each interval of HEF stress, the circuit shown

in Figure 4.10 is used. The load in Figure 4.10a is selected as one of the three shown in Figure 4.10b. With the switches labeled S_1 closed the HEF stress is applied and with S_2 closed the test pulses are applied over the desired load. The switches are used to connect the MOSFET leads between applied stress and the load without discharging the accumulated charge on the gate.



(a) Experimental circuit used for applying high voltage stress and measuring device transient characteristics and leakage current waveforms

(b) Three load types used in measuring changes in the turn-on transient waveforms

Figure 4.10 Experimental circuit used to apply stress and measure transient characteristics by switching connections on MOSFET leads

The values of the voltage and passive elements used for accelerated degradation of power Si MOSFETs are provided in Table 4.3. Experiments involving the SiC MOSFETs used different voltages and passive elements, provided in Table 4.4.

An oscilloscope measures the voltage drop across the series-connected resistors in the different loads in order to collect current measurements. The information collected with each load type is described in Table 4.5. The probes of the oscilloscope were placed on either side of R_1 , R_2 and R_3 to measure current when those loads are used.

Leakage current changes are assessed by using a machine as a load, shown in Figure 4.10b. Phase A is connected to the DC voltage and the case is connected to the drain of the

Table 4.3 Details of components and setup information for power Si MOSFET accelerated degradation testing

Parameter	Value
Gate drive voltage	10V
Gate resistance R_g	10 Ω
V_{DC} on resistive and inductive loads	5V
V_{DC} for phase-to-case connection load	20V
Phase resistance R_1	10 Ω
Phase inductance L_1	1mH
Resistive load R_2	2k Ω
Series resistance R_3	0.1 Ω
Oscilloscope sampling rate	1Gz

Table 4.4 Details of components and setup information for SiC MOSFET accelerated degradation testing

Parameter	Value
Gate drive voltage	20V
Gate resistance R_g	100 Ω
V_{DC} on load	50V
Resistive load R_2	1k Ω
Oscilloscope sampling rate	500MHz

Table 4.5 Different load types and the features measured when the MOSFET applied voltage across each

Load type	Measurement
Resistive-Inductive	Current rise delay
Resistive	V_{th} , V_{MP}
Phase-to-case connection	Leakage current, V_{ds}

MOSFET. Any current through this path therefore is through the insulation.

4.4.2 Effects of gate oxide degradation

Test pulses are applied after several one-hour intervals of HEF stress and the turn-on transient waveforms are captured. Experimental waveforms from the power Si MOSFETs are denoised using Daubechies D4 wavelet at the 6th level, as shown in Figure 4.11, in order to

obtain smooth waveforms to quantify the changes in voltages and currents.

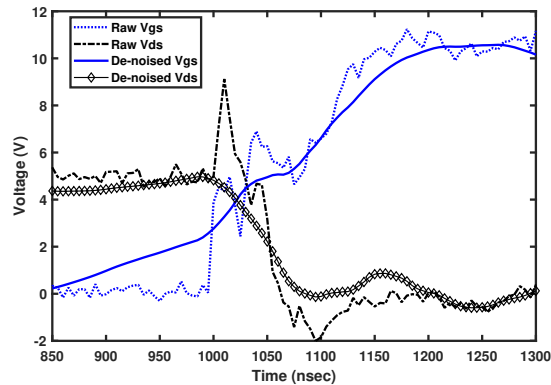


Figure 4.11 Example signals collected from the oscilloscope before and after noise was removed

The Miller plateau voltage magnitude and duration change with HEF stress is shown in Figure 4.12. A significant increase in both precursors, the voltage and duration, result after eight hours of gate oxide degradation.

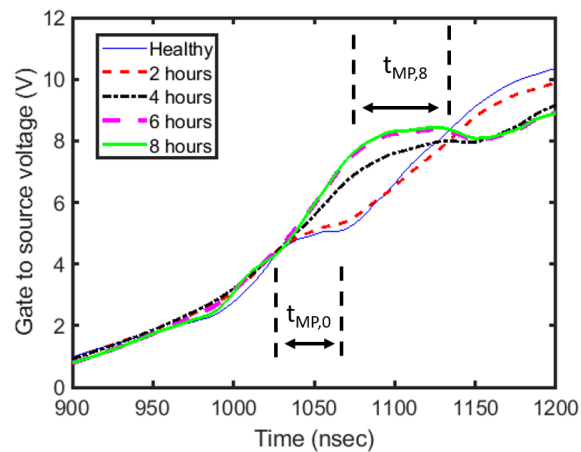


Figure 4.12 Gate-to-source voltage waveforms for healthy device and after several periods of HEF testing

Voltage across the device drops from the blocking voltage to the on-state voltage during the Miller plateau. As the Miller plateau increases, the applied dV/dt decreases. The peak-to-peak overshoot magnitude in the leakage current then decreases as the applied dV/dt

decreases, as shown in Figure 4.13.

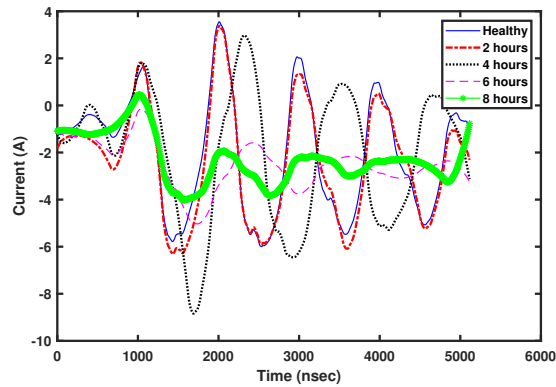
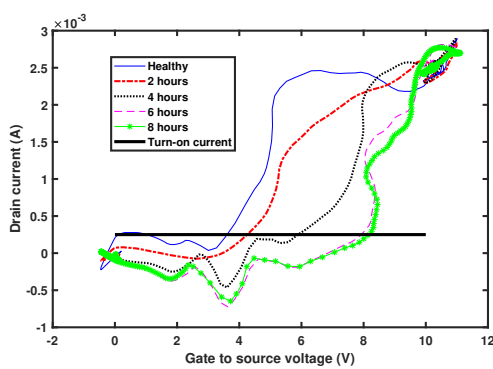
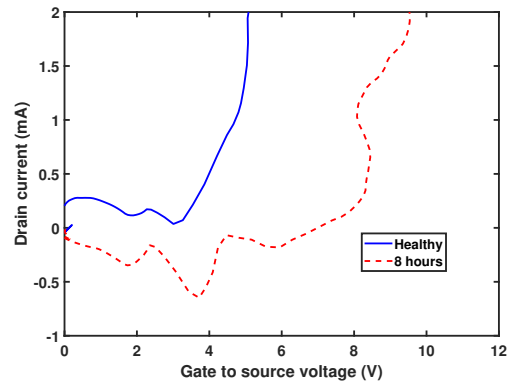


Figure 4.13 Leakage current waveforms after several periods of HEF testing

The value of V_{gs} where the current sharply rises is taken to be the turn-on threshold voltage of the device. The datasheet for the IRF520 specifies a drain current of $250\mu A$ as the current level when the threshold is reached. The voltage at the point when this current level is reached is then taken as the threshold voltage. Figure 4.14a shows a steady increase in V_{gs} level when the drain current begins to rise. Results after eight hours of HEF stress show an increase of nearly $4 V$ in V_{th} , shown in Figure 4.14b.



(a) Threshold voltage from healthy to failure

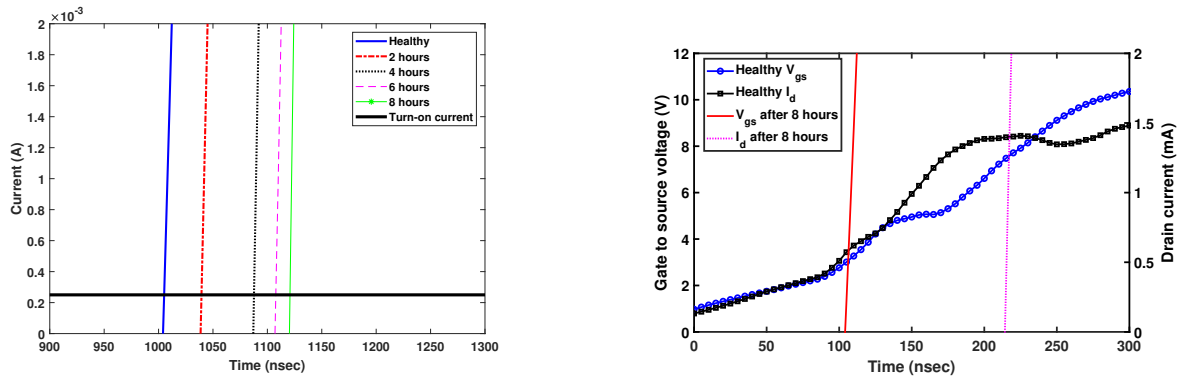


(b) Threshold voltage in healthy condition and at failure

Figure 4.14 Drain current vs V_{gs} to measure V_{th}

Following the increasing threshold voltage trend, the delay in phase current rise also

increases, shown in Figure 4.15a. When plotting the drain current with the V_{gs} , shown in Figure 4.15b, The gate voltage level required before current flows to the load is higher after gate oxide degradation, shown in Figure 4.15b.



(a) Current rise after several periods of HEF stress where the solid line indicates the current level at which the device is considered to be in the on state

(b) Current rise with V_{gs} to show magnitude of gate voltage required for device to be to conduct current

Figure 4.15 Delay in current rise after several periods of HEF testing

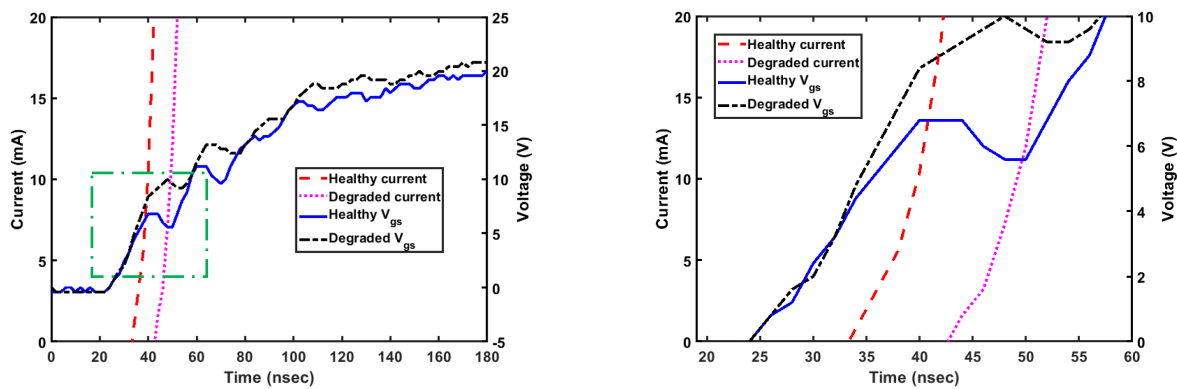
Quantified changes in voltage and current precursors of gate oxide degradation from the Si power MOSFETs are provided in Table 4.6. Precursors in the voltages and currents all show significant change after eight hours of accelerated degradation. Threshold voltage and delay in current rise each increased steadily after each hour of applied HEF stress while the Miller plateau duration and leakage current overshoot did not show a significant decrease until several hour of degradation have passed.

Voltage and current precursors of SiC MOSFETs after accelerated degradation show a similar trend as the Si power MOSFETs. Figure 4.16a shows the V_{gs} and drain current of a healthy and degraded SiC MOSFET. Two changes are visible when examining the Miller plateau region more closely, shown in Figure 4.16b. First, the device with degraded gate oxide shows an increase in Miller plateau voltage while the duration of the Miller plateau remains unchanged. Second, the current rise through the degraded device occurs later than

Table 4.6 Experimental changes in turn-on transient characteristics from Si power MOSFET

HEF applied time (hr)	V_{th}	V_{MP}	V_{ds} Fall (nsec)	I_{pp}	I	Delay (nsec)
0	2.97	5.89	78.3	9.7	10.5	
1	3.65	5.85	80	11.0	28.7	
2	5.3	6.63	167	10.0	66.3	
3	6.06	6.99	167	10.3	79.3	
4	6.46	7.78	173	11.5	103.1	
5	7.93	7.9	227	6.8	114.7	
6	8.55	8.39	278	5.3	136	
7	8.46	8.43	283	5.1	136.7	
8	8.63	8.57	290	4.4	140	

the current through the healthy device. The change in current rise occurring before a change in Miller plateau duration is found in both Si power MOSFETs and SiC MOSFETs.



(a) Current rise and V_{gs} from healthy and degraded SiC MOSFET

(b) Zoomed-in view of current rise and V_{gs}

Figure 4.16 Current rise and V_{gs} from healthy and degraded SiC MOSFET where figure on right is zoomed-in view of green box area on left plot

SiC accelerated degradation results are quantified in Table 4.7. A lower voltage is used to degrade the SiC MOSFET and a longer duration of applied stress is required in order to measure a significant change in turn-on transient voltage and current precursors. As the results show, the threshold voltage has significantly increased to double the healthy value and the delay in current rise shows a corresponding change.

Table 4.7 Table of SiC MOSFET results

HEF applied time (hr)	V_{th}	I	Delay (nsec)	V_{ds} Fall (nsec)	V_{MP}
0	4.4	10.0	14.0	14.0	6.1
2	4.4	10.0	14.0	14.0	6.4
5	4.8	10.0	12.0	12.0	8.17
8	5.2	12.0	14.0	14.0	9.4
13	8.8	20.0	16.0	16.0	9.48

Some inverter-drives may operate with a variable DC link voltage, which changes the V_{ds} that the device applies to the load. A Spice model, provided by Wolfspeed, is used to evaluate the effect of V_{ds} on current rise, threshold voltage, the Miller plateau voltage. As shown in Figure 4.17, threshold voltage change and delay are not affected by magnitude of DC voltage level. The time of current rise does not change when V_{ds} magnitude increases, although, V_{gs} is impacted.

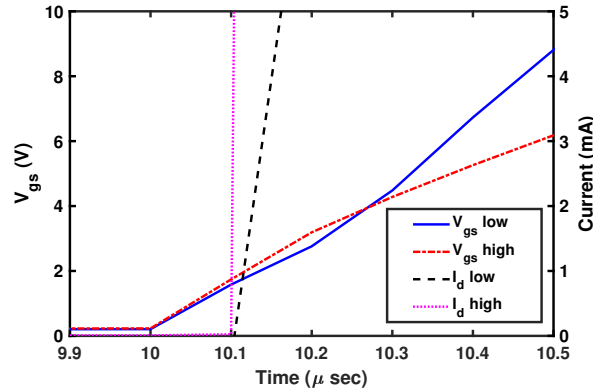


Figure 4.17 LTSpice simulation using C3M0280090D model provided from Wolfspeed where the low DC voltage used is 5V and the high DC voltage is 900V

4.5 Proposed technique

Delay creates an error in the current that is fed back to the controller. At steady-state speed and torque, the error creates a deviation in the commanded voltage. Monitoring the calculated voltage commands in the controller only requires sampling at the same rate as the main loop of the controller; thus decreasing the required sampling rate for detecting degraded switching devices.

A simple control diagram for a current-controlled PMSM is used to demonstrate the effect phase current error has on voltage commands, shown in Figure 4.18. The operating speed and commanded currents i_d^* and i_q^* are constant.

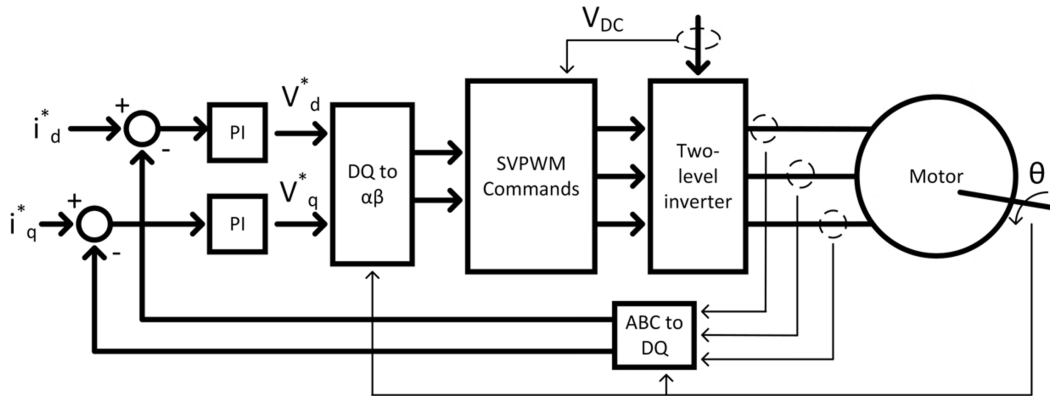


Figure 4.18 Example current control diagram

Commanded voltages are calculated from PI controllers, as shown in Equations (4.1) and (4.2), that are used to minimize the error in currents, $i_{d,e}$ and $i_{q,e}$. PI gains K_p and K_i are tuned to achieve the desired transient and steady-state performance.

$$V_d^* = K_p i_{d,e} + K_i \int i_{d,e} dt \quad (4.1)$$

$$V_q^* = K_p i_{q,e} + K_i \int i_{q,e} dt \quad (4.2)$$

Errors in the current are calculated from the measured currents $i_{d,m}$ and $i_{q,m}$ and the commanded currents, given in Equations (4.3) and (4.4).

$$i_{d,e} = i_d^* - i_{d,m} \quad (4.3)$$

$$i_{q,e} = i_q^* - i_{q,m} \quad (4.4)$$

Measured currents are calculated from the three phase currents using Clarke's and Park's transformations, Equation (4.5), where θ is the rotor position.

$$\begin{bmatrix} i_{q,m} \\ i_{d,m} \end{bmatrix} = \frac{2}{3} \begin{bmatrix} \cos(\theta) & \cos(\theta - \frac{2\pi}{3}) & \cos(\theta + \frac{2\pi}{3}) \\ \sin(\theta) & \sin(\theta - \frac{2\pi}{3}) & \sin(\theta + \frac{2\pi}{3}) \end{bmatrix} \begin{bmatrix} i_a \\ i_b \\ i_c \end{bmatrix} \quad (4.5)$$

When gate oxide degradation occurs in the high-side switching device in phase A, there is a deviation in the output current Δi_a , shown in Equation (4.6).

$$i'_a = i_a(1 - \Delta) \quad (4.6)$$

This decrease in magnitude is added to the error in q-axis current and augments it to produce $i'_{q,e}$.

$$i'_{q,e} = i_q^* - \left(i_{q,m} - \frac{2}{3} \Delta i_a \cos(\theta) \right) \quad (4.7)$$

$$i'_{d,e} = i_d^* - \left(i_{d,m} - \frac{2}{3} \Delta i_a \sin(\theta) \right) \quad (4.8)$$

The addition of i'_a causes the updated error $i'_{q,e}$ to increase and $i'_{d,e}$ to decrease. Adding $i'_{q,e}$ and $i'_{d,e}$ into Equations (4.1) and (4.2) creates an expression for the updated commands

$V_q^{*'}$ and $V_d^{*'}$, where the updated error creates a larger V_q command and more negative V_d command for the same steady-state operating point.

$$V_q^{*'} = K_p i'_{q,e} + K_i \int i'_{q,e} dt \quad (4.9)$$

$$V_d^{*'} = K_p i'_{d,e} + K_i \int i'_{d,e} dt \quad (4.10)$$

This change in V_q and V_d command is then input into the inverter modulation algorithm.

A wide variety of modulation techniques are available to apply the desired AC voltage to the machine. Space vector PWM (SVPWM) is a common modulation strategy that uses eight vectors, shown in Figure 4.19, to reach the desired V_α - V_β voltage; where the inverse Park transformation Equation (4.11) relates the $d - q$ quantities to the $\alpha - \beta$. Four voltage vectors are applied for a calculated duty cycle once every switching period. In steady-state operation, with constant voltage commands input to the SVPWM algorithm, the duty cycles for each applied voltage vector are also constant.

$$\begin{bmatrix} V_\alpha^{*'} \\ V_\beta^{*'} \end{bmatrix} = \frac{2}{3} \begin{bmatrix} \sin(\theta) & \cos(\theta) \\ -\cos(\theta) & \sin(\theta) \end{bmatrix} \begin{bmatrix} V_d^{*'} \\ V_q^{*'} \end{bmatrix} \quad (4.11)$$

When operating at the same steady-state point, an increase in $V_q^{*'}$ and decrease in $V_d^{*'}$ commands changes the SVPWM input voltage commands $V_\alpha^{*'}$ and $V_\beta^{*'}$. Assuming a constant DC link voltage, speed and current command, a change in the $\alpha - \beta$ voltage commands produces a change in the calculated duty cycles in the SVPWM algorithm. Therefore, the variation in duty cycles can be used to detect gate oxide degradation of the switching devices in the inverter-drive.

Normalized calculated duty cycles are proposed for detecting gate oxide degradation in

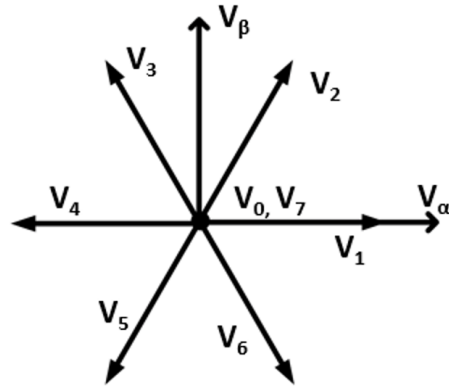


Figure 4.19 SVPWM voltage vectors with $\alpha - \beta$ reference

an inverter-drive application. Unlike V_d and V_q voltage commands, the PWM duty cycle commands are able to more easily distinguish the phase where the degraded switch is located as the individual SVPWM vectors can indicate which phase needs higher voltage at the given steady-state point. Duty cycles are already calculated in the controller and can be saved without additional sensors or higher frequency sampling. The duty cycles for the steady state operating point can also be collected and compared online.

4.6 Online detection experiment

To test effects of gate oxide degradation, stress is not applied to switching devices in a working inverter. Rather, an effect that mimics a delay in phase current rise is used to quantify the change in commanded SVPWM duty cycles.

A delay in phase current rise reduces the output current. Adding dead time to the gate signal mimics the delay. Dead time is required in the gate signals of all inverter switches to avoid shoot-through. High and low side switching devices of the same phase typically have dead time added to the rising edge of the gate signals. One phase leg of a two-level inverter is

shown in Figure 4.20a. Figure 4.20b shows example gate signals for these switches, where t_d dead time is added between the falling edge of the low-side switch and the high-side switch. If the high-side switch is experiencing gate oxide degradation, t_{delay} delay time is added to the dead time before the DC link voltage is output to phase A.

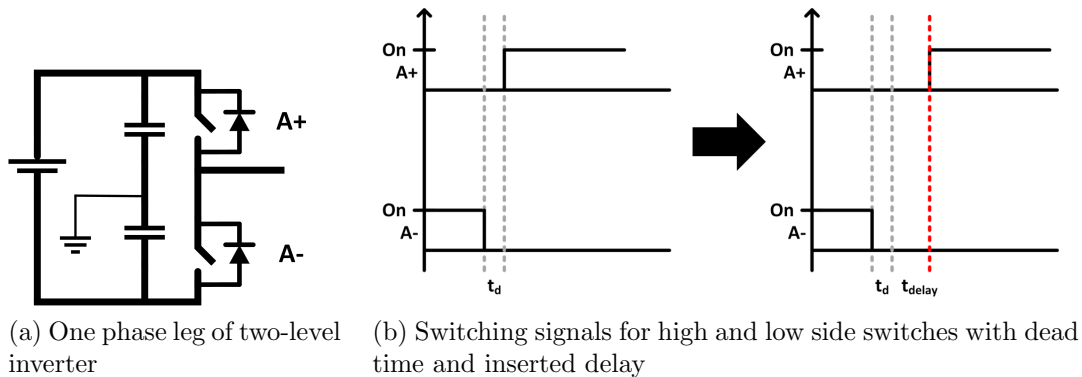
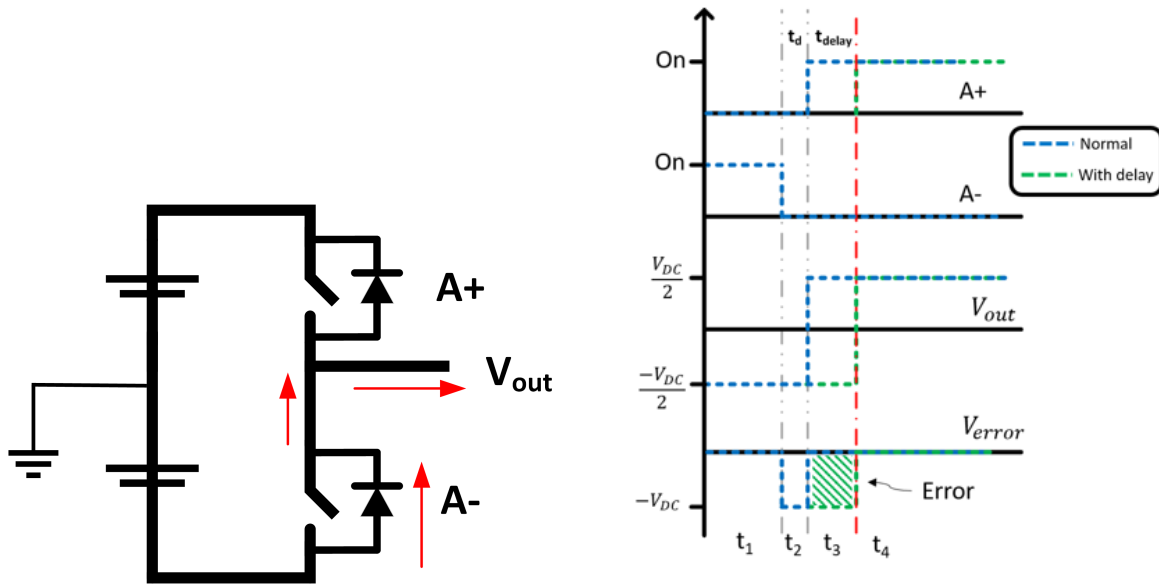


Figure 4.20 Examining dead time in one phase leg of an inverter and how a delay in current rise can have an effect similar to additional dead time

Additional delay time in when the switching device begins to conduct creates an error in output voltage. As shown in Figure 4.21, the high side switch does not begin to conduct until dead time passes, which leads to an error in V_{out} . The delay caused by gate oxide degradation leads to an application of negative voltage to V_{out} for an increased period of time, creating a larger error. Normal voltage error caused by dead time can be compensated; however, a delay due to gate oxide degradation cannot be compensated as it is unknown.

Increasing delay time in a current-controlled PMSM using SVPWM shows a measurable change in normalized duty cycle commands, shown in Figure 4.22. The duty cycle commands with no delay are recorded and used as baseline values. Normalized values are calculated using Equation (4.12), where $d_{delay,Vx}$ is the duty cycle command from the delay in vector V_x , x going from 0 to 7.

$$d_{N,Vx} = \frac{d_{delay,Vx}}{d_{base,Vx}} \quad (4.12)$$



(a) Current flow in undesired direction with additional dead time in top switch (b) Voltage error that is produced by current flow in undesired direction

Figure 4.21 With additional dead time, or delay, in top side switch and positive current flow, the error in output voltage increases

As the delay in the gate signal of the high-side switch of phase A increases, the duty cycle command for voltage vectors 1 and 2 increase. These vectors both increase voltage applied to phase A, and this increase in duty cycle compensates for the lower voltage output caused by MOSFET gate oxide degradation. Parameters of the simulated machine along with the selected operating point for quantifying duty cycle commands are provided in Table 4.8.

Table 4.8 Simulated operating point for comparing calculated duty cycles with different delay times

Parameter or operating point	Value
Rated current	25A
Operating current	20A
Rated speed	750RPM
Operating speed	300RPM
L_d	37.7mH
L_q	42.4mH
R_s	2Ω
Poles	10
V_{dc}	680V

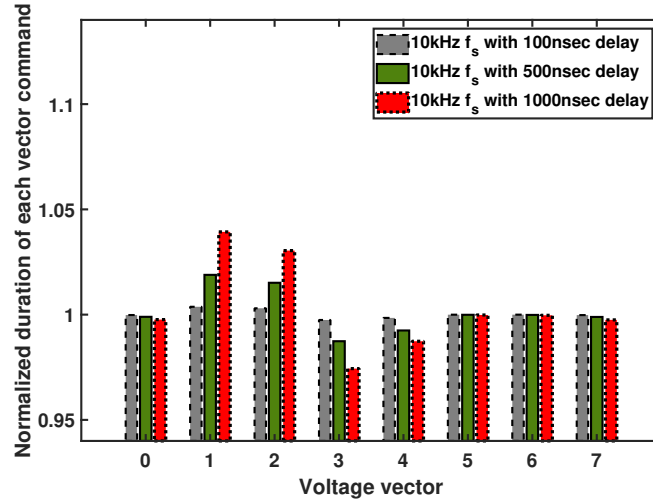


Figure 4.22 SVPWM duty cycles from simulated machine with different delay added to high side switch of phase A

Experiments are performed to quantify the effects of an increase in current rise delay by adding a specified delay to the gate signal of a switching device. Voltage commands from the controller are collected with and without a delay to show that the duty cycles can be used to detect gate oxide degradation.

4.6.1 Experimental setup

A current-controlled interior permanent magnet synchronous machine (IPMSM) driven by a three-phase inverter, similar to that shown in Figure 4.18, is used to obtain experimental data of the effects of an added delay in the gate signal of a switching device. A PMSM current controller is implemented in Real-time LabVIEW. In this controller, only two of the three phase currents are measured. The controller has the flexibility to add a delay as low as $25nsec$ in the gate signals of the switching devices. Figure 4.23 shows the gate signals output from LabVIEW to the inverter gate driver board. The signals for $A+$ and $A-$ switches without delay show the rising and falling edges occurring at the same time.

Figure 4.23 also shows that the controller can provide the correct delay to the gate signals when a $500nsec$ delay is desired between the falling edge of $A-$ and the rising edge of $A+$.

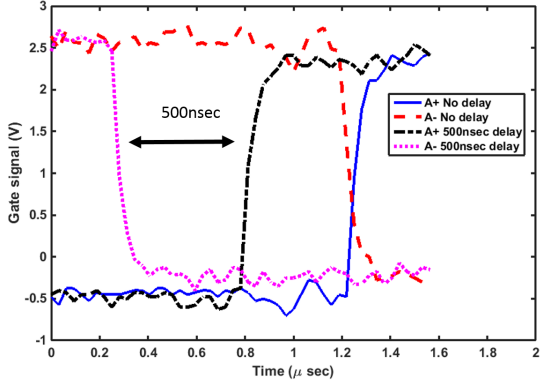


Figure 4.23 Gate signals to high and low side phase A switches used to add delay in turn-on to represent gate oxide degradation

Change in calculated SVPWM duty cycles with an added delay is experimentally recorded using a PMSM at the steady state operating point in Table 4.9. Ratings for the PMSM and inverter-drive are provided in Table 4.10.

Table 4.9 Experimental steady-state operating conditions

Operating point	Value
Current command	2.15A
Speed	300RPM
Temperature	25°C

Figure 4.24 shows a comparison of the applied voltage V_{AB} and phase A current with and without an added $100nsec$ delay to the high side switch of phase A. V_{AB} rises with a delay and is at the DC link voltage for a shorter duration. As a result, the phase A current at the same point in time is lower in magnitude due to lower voltage applied to that phase. This error in current is fed back to the PI controller, and as a result, the SVPWM duty cycles at this steady-state operating point change.

Table 4.10 Parameters of PMSM used for experimental validation

Rating	Value
Rated current	25A
Rated speed	300RPM
Phases	3
Slots	12
Poles	10
Rated voltage	480V _{ll}
Switching frequency (f_s)	10kHz
Built-in dead time	300nsec

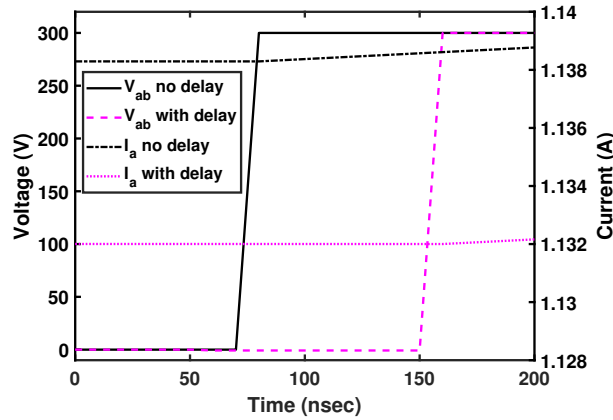


Figure 4.24 V_{AB} voltage applied with and without a 100nsec delay and the resulting current in phase A. With an added delay, there is an increasing error in the current.

4.6.2 Results with simulated degradation

Delays of 100nsec and 500nsec are added to the rising edge of the high side switch in phase A. The calculated duty cycles are recorded over ten electrical cycles in steady state operation and compared to the duty cycles at the same operating point with no added delay. Normalized duty cycle duration of vectors V_1 and V_2 increase significantly when a delay is added to the high side switch of phase A, as shown in Figure 4.25 and in Table 4.11.

Phase C current is not measured, but instead calculated assuming no leakage current from phases A and B measurements. To evaluate the effect on the controller-calculated duty cycles in the unmeasured phase, a delay is separately added to the high side switches of

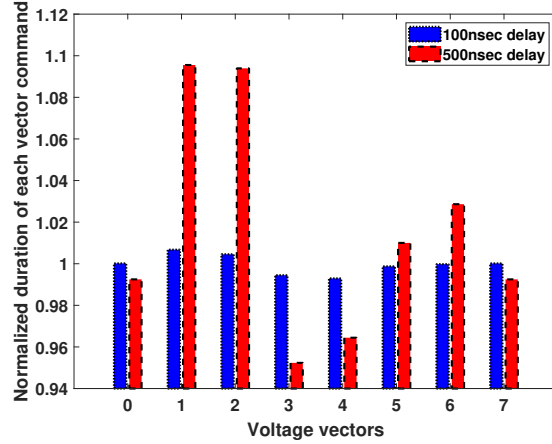


Figure 4.25 Normalized difference in controller-calculated duty cycles for all voltage vectors with delay added in high side switch of phase A

Table 4.11 Percent change in calculated duty cycle for each voltage vector with 100nsec and 500nsec delay added in high-side switch of phase A

Voltage vector	100nsec delay % Δ	500nsec delay % Δ
V_0	+0.02	-0.75
V_1	+0.67	+9.55
V_2	+0.45	+9.36
V_3	-0.55	-4.77
V_4	-0.71	-3.56
V_5	-0.13	+1.00
V_6	-0.02	+2.86
V_7	+0.02	-0.75

phases B and C. A delay in phase B produces an increase in vectors V_3 and V_4 , and a delay in phase C results in an increase in V_5 and V_6 , as shown in Figure 4.26 and Table 4.12.

This confirms that with only two measured currents, the normalized SVPWM duty cycles calculated in the controller can indicate the presence of gate oxide degradation in the switches of any of the three phases.

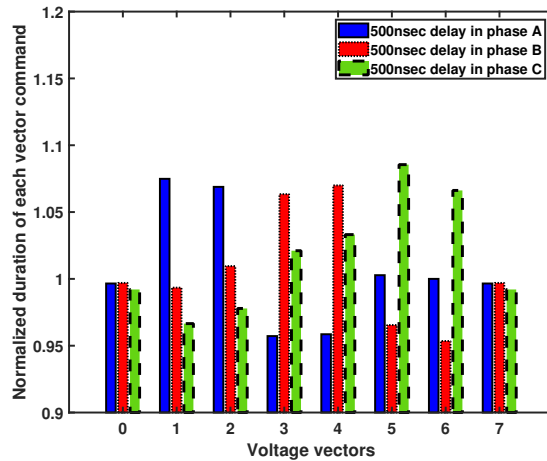


Figure 4.26 Comparing normalized duty cycle duration with same delay added to high side switch in all three phases where only phase A and B currents are measured

Table 4.12 Percent change in calculated duty cycle for each voltage vector with 500nsec delay added in high-side switch of specified phase

Voltage vector	Phase A % Δ	Phase B % Δ	Phase C % Δ
V_0	-0.35	-0.30	-0.79
V_1	+7.49	-0.66	-3.35
V_2	+6.89	+0.96	-2.21
V_3	-4.28	+6.34	+2.11
V_4	-4.14	+6.99	+3.31
V_5	+0.28	-3.45	+8.55
V_6	0	-4.65	+6.62
V_7	-0.35	-0.30	-0.79

4.7 Detection at higher switching frequencies

To investigate the significance of a higher inverter switching frequency, a current-controlled PMSM driven by a two-level inverter is modeled where the delay is added to the high side switch in phase A. Parameters of the modeled PMSM as well as the steady state operating point are provided in Table 4.13.

At 10kHz switching frequency, a 1000nsec delay is added; and at 100kHz switching frequency, a 100nsec delay is added. Figure 4.27 shows that in each case, the normalized

Table 4.13 Simulated operating point for comparing calculated duty cycles with different delay times

Parameter or operating point	Value
Current	20A
Speed	300RPM
L_d	37.7mH
L_q	42.4mH
R_s	2 Ω
Poles	10
V_{dc}	680V

change in duty cycle duration in all eight voltage vectors is similar.

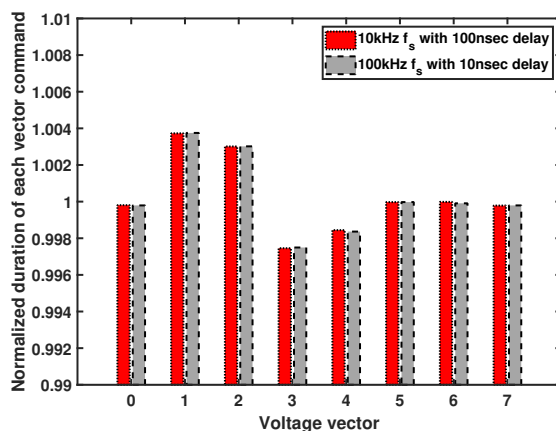


Figure 4.27 Normalized duration for each SVPWM voltage vector with different delay added to $A+$ switch at different switching frequencies

The percent change, given in Table 4.14, is similar in all vectors because the delay time occupies the same percentage of the total switching period in each case; as shown in Figure 4.28, where the switching period is described by Equation (4.13). This causes the applied voltage to decrease by the same percentage.

$$t_{sw} = \frac{1}{f_{sw}} = t_p - t_0 \quad (4.13)$$

Where

$$t_p = \frac{1}{f_s} \quad (4.14)$$

Table 4.14 Comparison of normalized change in duty cycles with different delay and switching frequency (f_s) simulated

Voltage vector	10kHz f_s with 1000nsec delay % Δ	100kHz f_s with 100nsec delay % Δ
V_0	-0.24	-0.25
V_1	+3.93	+3.98
V_2	+3.04	+3.04
V_3	-2.56	-2.56
V_4	-1.26	-1.28
V_5	-0.01	-0.02
V_6	-0.03	-0.03
V_7	-0.25	-0.25

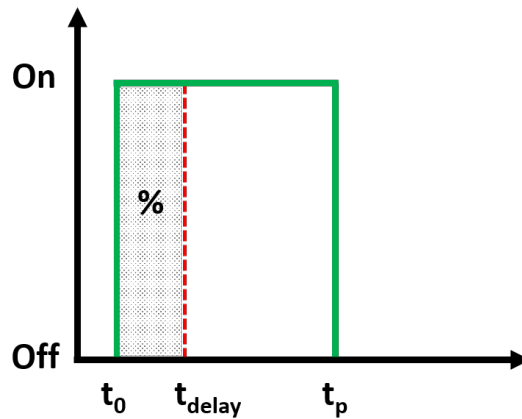


Figure 4.28 Output voltage decrease depends on the percentage of the switching period that the delay occupies

For a higher switching frequency, which is one advantage of employing MOSFET devices in an inverter-drive, a shorter delay has a more significant impact on the calculated SVPWM duty cycles. Since a shorter delay is more salient when operating at higher switching frequencies, earlier stages of gate oxide degradation can be detected when the switching frequency is higher.

Chapter 5

Robust Insulation Failure Prognosis

Algorithm

Failure prognosis is more useful than detecting degradation or the presence of a fault. An accurate RUL estimate provides the machine operator with knowledge of when failure will occur so that the machine can remain in operation for a longer period of time, avoiding unnecessary downtime, while allowing the operator to properly power-down the machine before an unexpected failure occurs. The proposed technique to detect insulation degradation online uses leakage current overshoot magnitude as the degradation feature.

5.1 Background

An online insulation degradation detection technique developed in [26,27] are shown to detect insulation failure as accurately as an offline test. However, this technique only indicates when insulation is no longer healthy; it is not clear if an RUL estimate can be obtained. In [24], the insulation capacitance, resistance and dissipation factor can be measured online and are proposed for continuous condition monitoring. While it states that tracking the proposed features can be used for prognosis, it is again not clear how this is achieved. A proposed prognosis technique in [46] uses leakage current measurements and an Extended Kalman Filter (EKF) to predict RUL. In [47], a statistical model of the insulation's lifetime

uses voltage measurements in an inverter-driven machine to estimate RUL. However, the techniques in [46, 47] both require high frequency sampling of the degradation features.

Insulation strength and the rate of degradation varies between machines. A prognosis technique must be robust with these variations in insulation lifetime.

In [25], experimental measurements of the insulation capacitance are curve-fit to an Arrhenius model and are used to predict the decrease in capacitance. RUL is estimated based on when the capacitance crosses a threshold that indicates failure. However, this proposed technique requires an expensive voltage sensor. Also, it has been suggested in [11] that the Arrhenius model for lifetime based on temperature stress is inaccurate. A prognosis based on this model, therefore, may not be robust to unexpected variations in applied stress.

In this work, insulation failure prognosis is achieved using a Bayesian filtering technique. An EKF is one Bayesian filtering technique that is capable of nonlinear state tracking. EKF has been proposed for estimating the RUL for stator insulation [46]. Parameter and state estimation using an EKF has been applied to power MOSFET failure prognosis [48], bearing RUL prediction [49] and battery state of charge [50]. Prediction using the EKF only require the value of the previous estimation, not the entire history, providing an advantage in lower required memory space. However, the accuracy and convergence of the EKF is highly dependent on the initial state estimates. In [49], initial state estimates are found from training data. Without accurate training data, where there is a significant amount of noise in the available measurements, the EKF may not be able to provide a sufficiently accurate prognosis.

Particle filters (PFs) are another Bayesian filtering technique that have been demonstrated to track noisy, highly nonlinear trajectories [51]. Parameter and state estimation using a PF has been shown to be more robust than an EKF [52]; and their use has been

demonstrated literature in estimating battery state of charge [53] and RUL of batteries [51], supercapacitors [54] and bearings [55]. While PFs can more accurately track trajectories with high degrees of nonlinearity, they typically require a high computational cost [56].

An EKF and PF are developed and applied to the data sets from the accelerated thermal degradation experiments. Accuracy of the RUL predictions and their robustness to error in initial conditions, rates of degradation and differences in insulation systems are compared.

5.1.1 Extended Kalman Filter

There are several Kalman filter variants available. The EKF is an extension of the linear Kalman filter that linearizes the state transition matrix and the output matrix in order to use a linear system of equations for prediction.

The nonlinear system model used for the EKF is shown in Equations (5.1) and (5.2). Here, x represent the state variables, F is the state transition matrix, w is the process noise covariance, v is the measurement noise covariance, H is the output matrix and z is the measured output.

$$x_k = F_{k-1}x_{k-1} + w_{k-1} \quad (5.1)$$

$$z_k = H_k x_k + v_k \quad (5.2)$$

Matrices F and H are linearized about the current values of the states using:

$$F_k = \left. \frac{\delta f}{\delta x} \right|_{x_k} \quad (5.3)$$

$$H_k = \left. \frac{\delta h}{\delta x} \right|_{x_k} \quad (5.4)$$

The uncertainty matrices, M and P , are used to update the Kalman gain, K , and the

predicted value of the state variables, as shown in Equations (5.5) to (5.8).

$$M_k = F_{k-1}P_{k-1}F_{k-1}^T + Q_{k-1} \quad (5.5)$$

$$K_k = M_k H_k^T (H_k M_k H_k^T + R_k)^{-1} \quad (5.6)$$

$$x_k = x_k + K_k(z_k - H_k x_k) \quad (5.7)$$

$$P_k = (1 - K_k H_k) M_k \quad (5.8)$$

Matrix R represents the measurement noise covariance and matrix Q represents the process noise covariance.

Unknown parameters of the nonlinear state trajectory can be included as states and the EKF can predict their true values [50]. For the nonlinear function shown in Equation (5.9), the desired state x_1 can be estimated as well as the parameters x_2 and x_3 , if they are unknown.

$$x_1 = x_2 e^{x_3 t} \quad (5.9)$$

A state matrix is then composed of all three unknowns, and the state transition can assume that these unknown parameters are constant, as shown in Equation (5.11).

$$x = [x_1, x_2, x_3]^T \quad (5.10)$$

$$f(x, t) = \begin{pmatrix} x_2 e^{x_3 t} \\ x_2 \\ x_3 \end{pmatrix} \quad (5.11)$$

The EKF process first assumes initial estimates of the states x and the posterior estimate

covariance matrix, P_0 . The forecast error covariance matrix M is updated when a prediction is made before an observation is received and the posterior estimate covariance matrix P is updated after an observation is received, as shown in Figure 5.1. When observations are no longer received, the current estimated parameters of the nonlinear function that represent the state transition are used for predicting the future trajectory of the state.

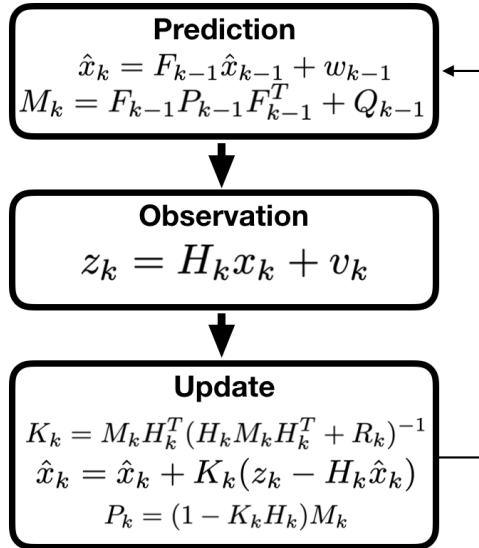


Figure 5.1 After initial estimates area made, this flow chart outlines the iterative process trajectory tracking using the EKF

5.1.2 Particle Filter

Similar to the EKF, the PF is a Bayesian filtering technique where the state transition and measurement model can be represented in the form of state equations, as shown in Equations (5.12) and (5.13).

$$x_k = f(x_{k-1}, u_k) + w_k \tag{5.12}$$

$$z_k = h(x_k) + v_k \tag{5.13}$$

In the PF, state equations are represented as probability density functions (PDFs), shown in Equations (5.14) and (5.15).

$$f(x_{k-1}, u_k) + w_k \leftrightarrow p(x_k|x_{k-1}) \quad (5.14)$$

$$h(x_k) + v_k \leftrightarrow p(z_k|x_k) \quad (5.15)$$

Where the PDF in Equation (5.14) is the prior probability distribution as it predicts the value of the state variables at the next time step before receiving a measurement. The PDF in Equation (5.15) is the likelihood function, the probability of receiving the measurement z_k given that the states have a value x_k .

From initial state estimates, a prediction of the next state is made based on the previous observations. Then, an update is made when an observation is received. The PDF for prediction is defined using the Chapman-Kolmogorov equation, shown in Equation (5.16) [56].

$$p(x_k|z_{1:k-1}) = \int p(x_k|x_{k-1})p(x_{k-1}|z_{k-1})dx_{k-1} \quad (5.16)$$

This equation shows the probability of being in x_k given that $z_{1:k-1}$ have been observed, the forecast PDF used for a priori prediction. This PDF is created by multiplying probability of being in x_{k-1} given z_{k-1} by the probability of being in x_k given the previous state was x_{k-1} , and integrating over the possible x_{k-1} states.

The posterior probability distribution, the PDF that represents the probability of transitioning to the present state after the current observation z_k is received, is desired. To calculate the posterior probability distribution, Bayes' rule, shown in Equation (5.17), is

applied.

$$p(A|B) = \frac{p(B|A)p(A)}{p(B)} = \frac{p(B|A)p(A)}{\int p(B|A')p(A')dA'} \quad (5.17)$$

Applying Bayes' rule to the state variables and measurements, the posterior probability distribution is obtained in Equation (5.18).

$$p(x_k|z_{1:k}) = \frac{p(y_k|x_k)p(x_k|z_{1:k-1})}{p(z_k|z_{1:k-1})} \quad (5.18)$$

Where

$$p(z_k|z_{1:k-1}) = \int p(z_k|x_k)p(x_k|z_{1:k-1})dx_k \quad (5.19)$$

The solution to Equations (5.18) and (5.19), however, is only conceptual. The PDF cannot be evaluated analytically due to the complex, high-dimensional integral [57]. To calculate the posterior PDF, a proposal PDF (q) is used for a priori prediction. The proposal PDF is typically the same PDF used to represent the state transition, as shown in Equation (5.20).

$$q(x_k|z_{1:k}) = p(x_k|x_{k-1}) \quad (5.20)$$

From this PDF, N number of samples are taken. These samples are referred to as the particles. When an observation is received, the distance between each particle and the observed value is calculated. A weight is assigned to each particle, where the particles closer to the observed value receive the higher weights. Weights are assigned using the expression in Equation (5.21), where v is the variance of measurement noise.

$$w_k^i = \frac{1}{\sqrt{2\pi v}} \frac{2v}{|z_k - x_k^i|} \quad (5.21)$$

For

$$i = 1 : N \tag{5.22}$$

The weights are then normalized, and the posterior PDF is created based on the weighted particles, shown in Equation (5.23).

$$p(x_k | z_{1:k}) = \sum_{i=1}^N w_k^i (x_k^i - x_k) \tag{5.23}$$

An updated prediction is obtained by re-sampling of the posterior PDF created from the weighted particles. The method to weight and re-sample the particles is important, and there are a variety of methods available in literature [56]. One typical issue is that after re-sampling, particles with a high weight duplicate themselves several times. After a few time steps, the particles with the highest weight may be the only one left. The different re-sampling methods seek to preserve diversity in the particle values.

Figure 5.2 shows a simple visual example of the PF process where the dots represent the particles. An initial distribution of N particles, with equal weight, are obtained from q . Then, when an observation is received, the particles are weighted based on their proximity, and a PDF is created from this weighted distribution. Particles with the highest weight are re-sampled to obtain N particles with equal weight again. The process then continues as a new observation is received and the weights create an updated posterior PDF for prediction.

A high-level flow chart of the PF implemented for insulation failure prognosis is provided in Figure 5.3a. The re-sampling process is described in more detail in Figure 5.3b. Weighted particles are input to the re-sampling algorithm. With the best particles maintained, and new samples created, the population of particles still contains a diverse selection for searching for more accurate parameter values while keeping the latest, most accurate particles. A

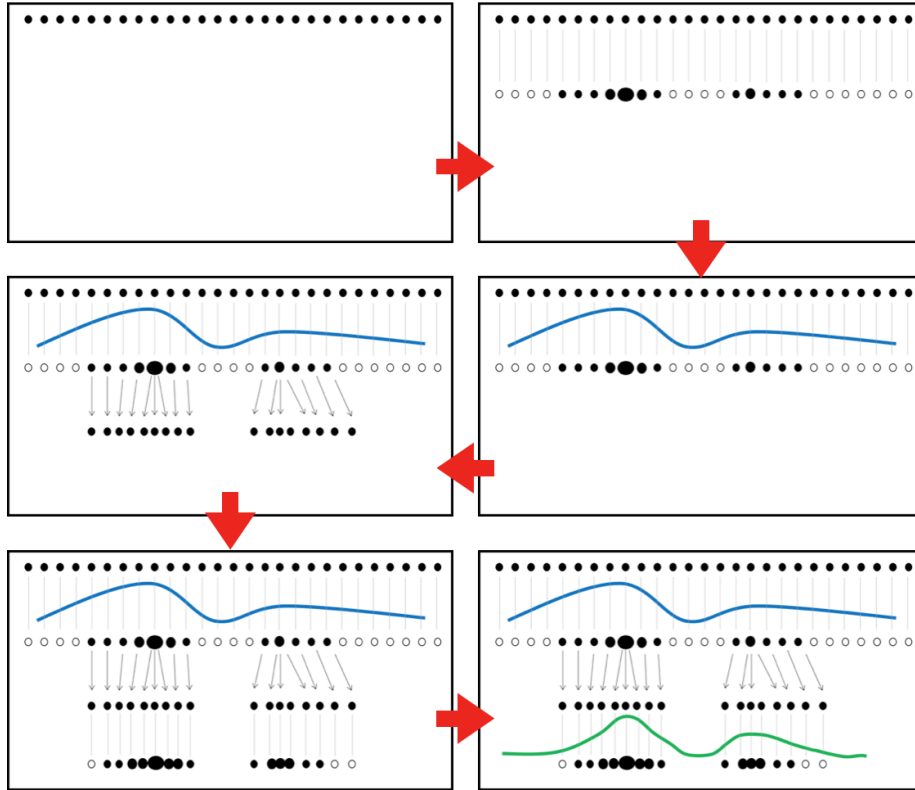


Figure 5.2 General iterative particle filter process visually displayed where the dots represent one particle

cumulative distribution function (CDF) is created from the normalized, weighted particles.

An example CDF is shown in Figure 5.4.

The selected number of particles impacts the computation effort in implementing a particle filter. Many particles can lead to quicker convergence and a more accurate prediction; however, each particle is assigned a weight and re-sampled using algorithms that can be complex in order to preserve diversity.

5.2 Prognosis

Filtering techniques are used to estimate the nonlinear model that fits the trend in the insulation degradation feature found from accelerated degradation testing. The nonlinear

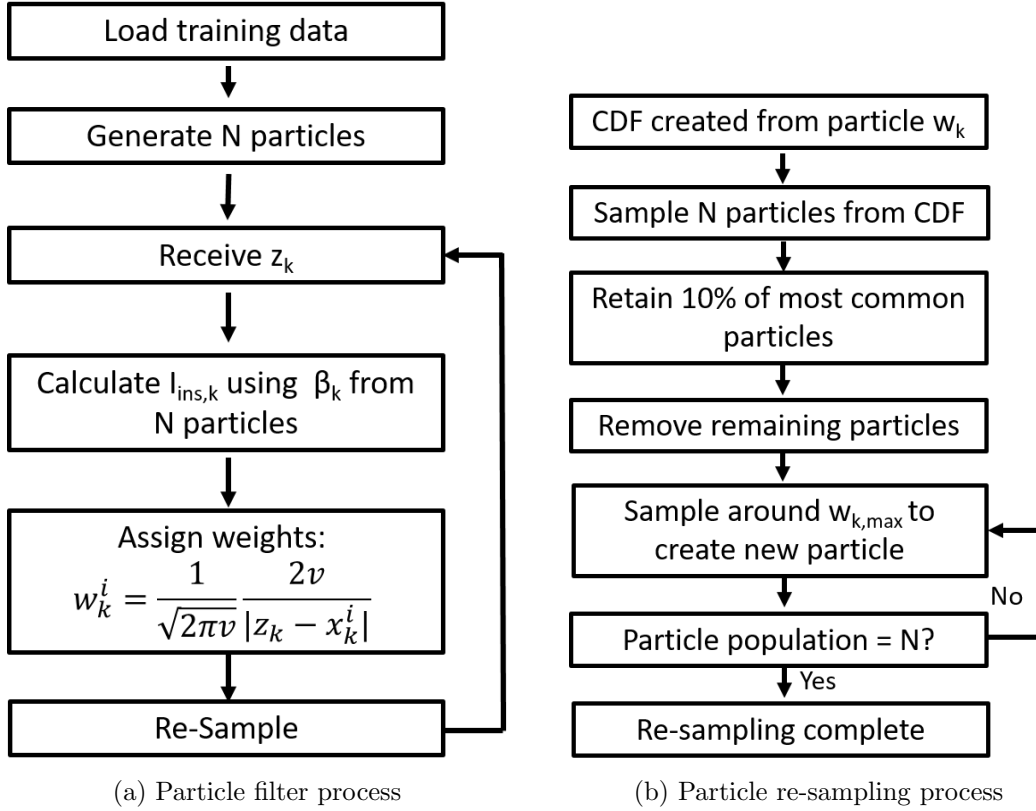


Figure 5.3 RUL estimated using EKF compared to actual RUL from three sets of experimental data

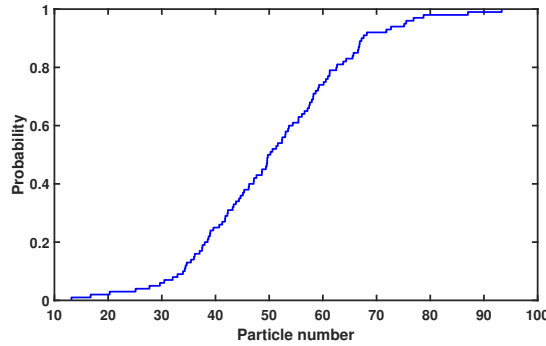


Figure 5.4 Example cumulative distribution function used in re-sampling particles in PF process. A random value between 0 and 1 is sampled N times from the CDF and the particle associated with that value is added to the new population.

model of the degradation feature is used to estimate RUL. While the nonlinear trend in the insulation current overshoot is obtained experimentally from thermal degradation, a similar trend would emerge when other sources of stress degrade the insulation.

Prognosis typically requires four available pieces of information about the system or device: a behavioral model, measurement model, degradation measurements and a failure threshold [57]. The magnitude of the overshoot in leakage current at the switching transient increases to a peak and then exponentially decays as the insulation ages, shown in Figure 3.12. This trend, shown in Figure 5.5, can be used as the behavioral model.

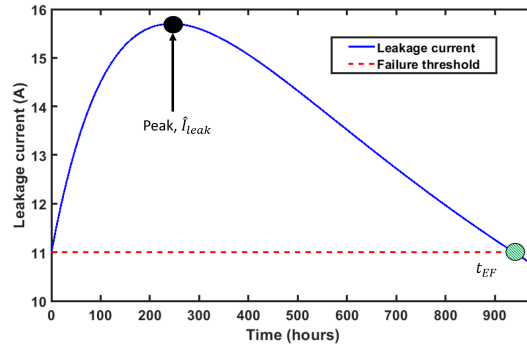


Figure 5.5 Example trend in leakage current overshoot with peak, failure threshold and estimated time of failure t_{EF} labeled

Equation (5.24) can be used to describe the behavior of the overshoot in the leakage current after the peak is reached. Here, I_{leak} is the measured overshoot magnitude, α is the peak value and β is the rate of decay. Using this behavioral model, the β value can be directly related to the changing impedance of the insulation material as it degrades.

$$I_{leak} = \alpha e^{\beta t} \quad (5.24)$$

The measurement model is used to link the degradation measurement to the behavioral model. The healthy value is taken to be the failure threshold, shown in Figure 5.5. The predicted time of failure is the point where the behavioral model intersects the failure threshold. The difference between the predicted time of estimated failure, t_{EF} , and the current time is the RUL.

The overall RUL estimation process is shown in the flow chart in Figure 5.6. Shown in Figure 5.6a, RUL estimation begins once the peak value in the leakage current trend is detected.

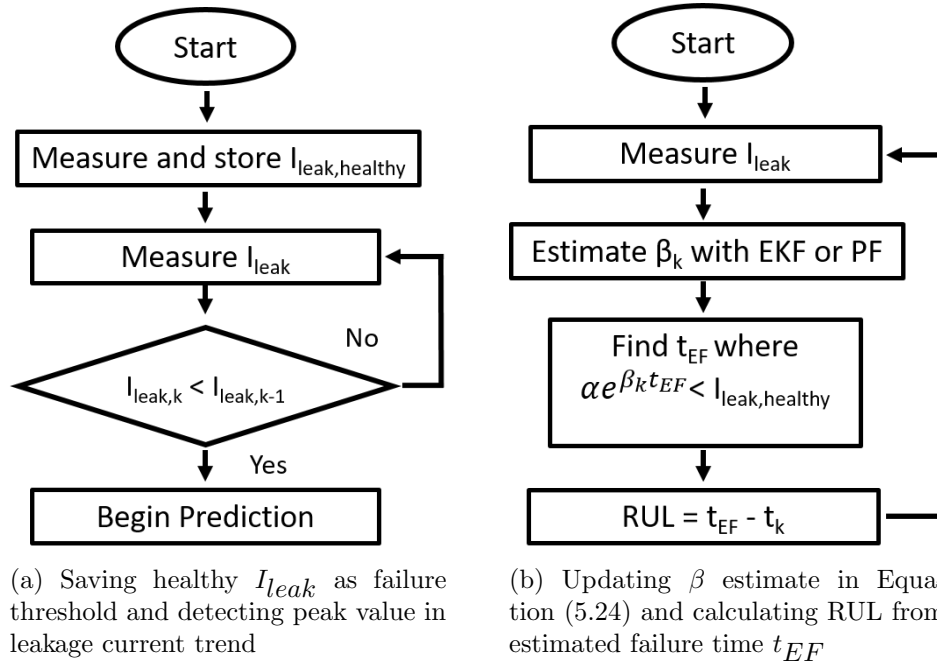


Figure 5.6 Process of estimating RUL where EKF or PF used to estimate β

Figure 5.6b shows how RUL is estimated as new I_{leak} observations are received. In this work, α is fixed; determined from the peak value and healthy leakage current as described in Equation (5.25).

$$\alpha = \hat{I}_{leak} - I_{leak,healthy} \quad (5.25)$$

β is estimated at every time k using either the EKF or PF algorithm.

5.2.1 Metrics of accuracy

The mean-squared-error (MSE), the coefficient of determination (R^2), time spent within 20% of the true RUL (t_{20}) and the 95% confidence interval (CI) produced by the RUL estimates are used to assess the accuracy of the predicted RUL.

The MSE is calculated by comparing the error between the estimated RUL (RUL_E) and true RUL (RUL_T) for every sample (N_s). This is used to quantify the error in the prediction, shown in Equation (5.26).

$$\text{MSE} = \frac{\sum_{i=1}^{N_s} (RUL_E^i - RUL_T^i)^2}{N_s} \quad (5.26)$$

The coefficient of determination, R^2 , is calculated by using Equation (5.27) [58]. In this case, the the expected model is the true RUL and the data set is the estimated RUL. A higher R^2 value indicates that the variance in the estimated RUL is low and the true RUL is a good fit for the estimated RUL.

$$R^2 = \left(\frac{n\Sigma(RUL_E * RUL_T) - (\Sigma(RUL_E)\Sigma(RUL_T))}{\sqrt{n\Sigma(RUL_E^2) - (\Sigma(RUL_E))^2} \sqrt{n\Sigma(RUL_T^2) - (\Sigma(RUL_T))^2}} \right)^2 \quad (5.27)$$

20% upper and lower band are placed on the true RUL. A count of the number of points of the estimated RUL that satisfy the inequality in Equation (5.28) is calculated. The number of samples in this count is then translated into time. Total time duration within this error band, t_{20} , quantifies the length of time that the algorithm produced an accurate prediction.

$$(RUL_T^i \times 0.8) \leq RUL_E^i \leq (RUL_T^i \times 1.2) \quad (5.28)$$

For

$$i = 1 : N_s \quad (5.29)$$

A CI represents a range where the RUL is expected to lie [59].

CIs can be determined by creating a distribution of t_{EF} values from all N_s sample points.

To compare the EKF and PF, a 95% CI is calculated from the estimated t_{EF} values, shown in Figure 5.7. This CI shows a range, an upper and lower bound, that 95% of the estimated t_{EF} values lie within. A more accurate RUL prediction is determined based on the CI containing the actual time of failure and a narrower range of the CI bounds.

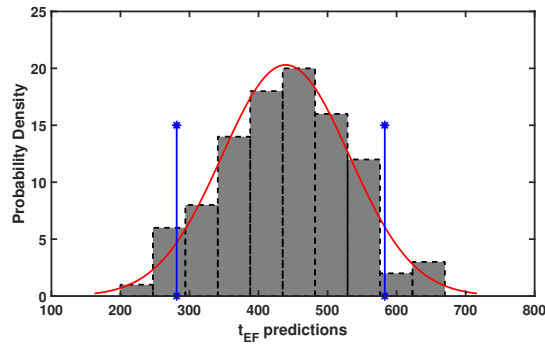


Figure 5.7 Example PDF showing how confidence intervals are calculated from the distribution of t_{EF} calculated from each algorithm

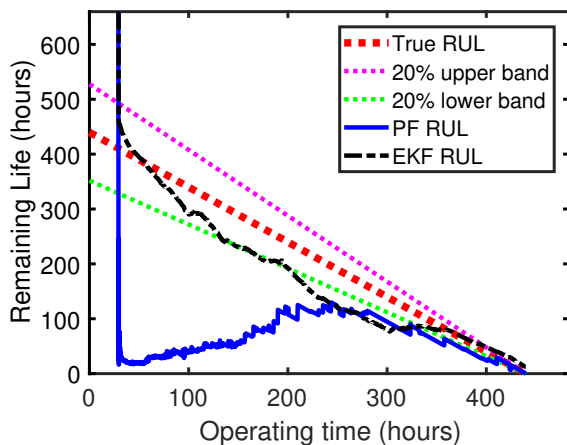
5.2.2 Results

Experimental data sets of the leakage current overshoot magnitude are used for comparing RUL estimates from the EKF and PF. Data sets from Machines 2 and 3 are compared as these machines had similar insulation systems and degraded at the same, constant temperature. Parameters used in the EKF and PF are provided in Table 5.1. The α and β values for each are calculated from fitting the trend in the experimental data after it was collected.

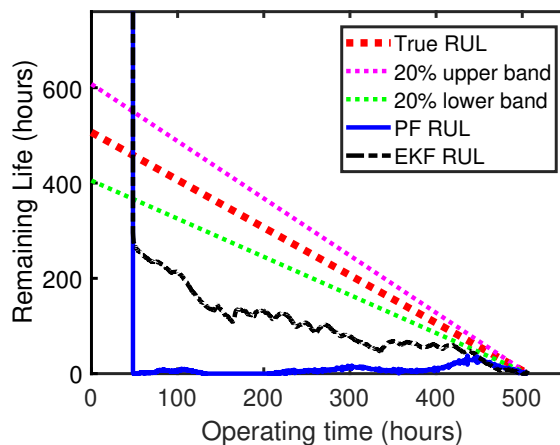
Calculated RUL from each experimental data set, provided in Figure 5.8, shows that the EKF and PF can provide a prognosis before failure occurs while the EKF shows higher accuracy over the whole lifetime of the insulation compared to the PF. Also, the RUL prediction is underestimated before failure occurs, which is better for avoiding unexpected failures but leads to the premature removal from operation.

Table 5.1 Initial trend parameters and settings used in EKF and PF to estimate RUL for Machines 2 and 3

Algorithm	Parameter	Machine 2	Machine 3
EKF	$P(0)$ Uncertainty matrix	0.01	0.01
EKF	R Measurement noise covariance	0.1	0.1
EKF	Q_{x_1} Process noise covariance	$1e^{-5}$	$1e^{-5}$
EKF	Q_{x_2} Process noise covariance	$1e^{-5}$	$1e^{-5}$
EKF	Q_{x_3} Process noise covariance	$1e^{-19}$	$1e^{-19}$
PF	Number of particles	100	100
PF	Measurement noise variance	1	1
PF	Variance of β for initial sampling	200×10^{-9}	200×10^{-9}
PF	Variance of β for re-sampling	20×10^{-9}	20×10^{-9}
EKF, PF	$\alpha(0)$	40	15.5
EKF, PF	$\beta(0)$	$-7e^{-7}$	$-3e^{-7}$



(a) Predicted RUL from EKF and PF compared with actual RUL from Machine 2



(b) Predicted RUL from EKF and PF compared with actual RUL from Machine 3

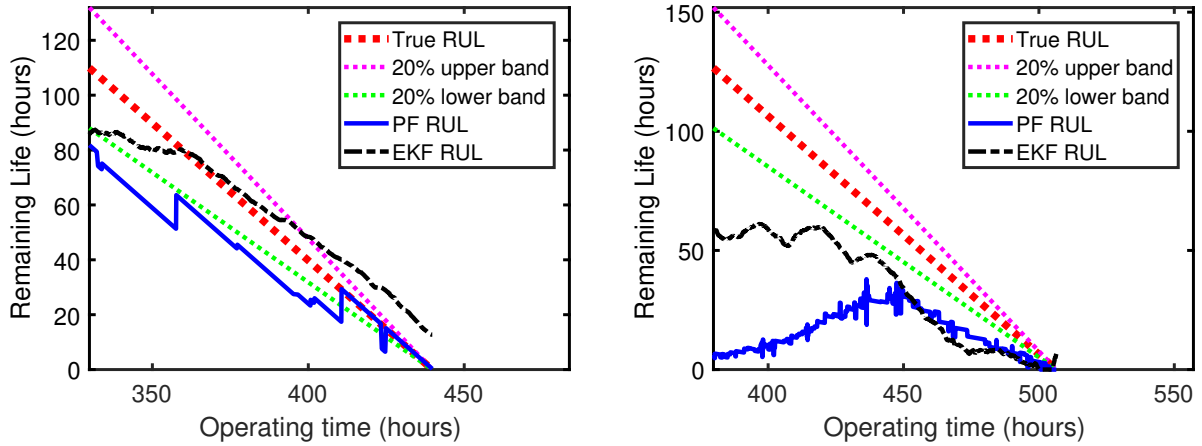
Figure 5.8 RUL estimated using EKF and PF compared to actual RUL from two sets of experimental data with 20% confidence intervals provided

The RUL estimate from the PF converges closer to the true RUL after more observations have been collected. When looking near the end of life, in Figure 5.9, the PF converges well to the true RUL. Table 5.3 quantifies accuracy towards the end of life. Close convergence to the true RUL near the end of life is important, as that is when a decision to continue operation or not can be critical. When degradation is just beginning, experience may suggest that the insulation is not immediately near failure as the PF shows; rather, more measurements are

Table 5.2 Accuracy of RUL estimated using EKF and PF for Machines 2 and 3

Machine	Algorithm	MSE	R^2	t_{20} (hr)	CI (hr)
2	EKF	1936	93.5	204.5	[371.75, 452.95]
2	PF $N = 50$	35551	0.30	5.5	[68.92, 433.8]
2	PF $N = 100$	35612	0.47	25.83	[69.7, 440]
2	PF $N = 300$	45502	0.07	24.75	[69.4, 435.1]
3	EKF	21683	90.02	0	[277.7, 491.6]
3	PF $N = 50$	67817	40.27	0.02	[16.19, 114.2]
3	PF $N = 100$	67820	40.15	0	[16.15, 116.2]
3	PF $N = 300$	67800	40.17	0.08	[16.1, 115.7]

needed to improve the prediction.



(a) Predicted RUL from EKF and PF compared with final 25% of actual RUL from Machine 2

(b) Predicted RUL from EKF and PF compared with final 25% of actual RUL from Machine 3

Figure 5.9 RUL estimated using EKF and PF compared to actual RUL from last 25% of actual lifetime with 20% confidence intervals shown

Table 5.3 Accuracy of last 25% of estimated RUL using EKF and PF for Machines 2 and 3

Machine	Algorithm	MSE	R^2	t_{20} (hr)	CI (hr)
2	EKF	97.02	98.25	65	[425.2, 453]
2	PF $N = 50$	300.45	98.44	5.5	[411.25, 433.8]
2	PF $N = 100$	361.97	97.19	25.83	[408.9, 440]
2	PF $N = 300$	337.1	96.85	24.75	[408.7, 442.25]
3	EKF	811.9	93.89	0	[458.19, 501, 14]
3	PF $N = 50$	2630	11.47	0.02	[89.57, 118.53]
3	PF $N = 100$	2633	10.2	0	[87.8, 120.1]
3	PF $N = 300$	2601	12.8	0.08	[88.8, 119.2]

5.2.3 Computational effort analysis

In the EKF, the step where the Kalman gain K is updated requires an inverse matrix calculation. The size of the K matrix depends on the number of parameters. Therefore, fewer states greatly reduces the computation cost. The steps involved in the EKF algorithm and the number of calculations per time step are listed in Table 5.4.

Table 5.4 Steps required to implement the EKF

Step Number	Description	Number of operations
1	Predict next state	1
2	Update M	1
3	Update K	1
4	Update state prediction	1
5	Update P	1

As shown in Table 5.5, the number of required operations in the PF algorithm is highly dependent on the number of particles N .

Table 5.5 Steps required in implementing the PF

Step Number	Description	Number of operations
1	Calculate I_{leak} for all particles	N
2	Record observation with added noise	1
3	Find error between observation and all particles	N
4	Assign weights to all particles	N
5	Normalize weights	1
6	Re-sample particles using weights	N
7	Create new random particles sampled around particle with highest weight	N

Each algorithm also has different memory requirements. For the EKF, the required arrays and matrices that need to be saved at every time step are provided in Table 5.6. Required memory size is also dependent on the number of state variables being estimated.

Table 5.6 Required memory to implement the EKF

Matrix or array	F_k	P_k	M_k	K_k	H_k	x_k
Size	3×3	3×3	3×3	3×1	3×1	3×3

The PF is estimating the parameters for a curve that fits well with the entire history of the observations, and therefore the entire history is required. There are N particles that are evaluated at every time step and each particle contains estimates for N_p number of parameters. Table 5.7 shows the required matrices for the PF algorithm.

Table 5.7 Required memory to implement the PF

Matrix	Size
Particles	$N \times N_p$
Observation history	$1 \times N_s$

Each algorithm is implemented in a MATLAB script and executed on a PC with an Intel Core i7-4790 CPU. The EKF shows a significant advantage in computational effort when compared to the PF, as shown in Table 5.8. Insulation degradation, however, is a slow process and required computation time is not a significant concern as the degradation will progress slower than the PF computation time.

Table 5.8 Comparison of EKF and PF computational cost with $N_s = 2379$

Algorithm	# of operations per sample	Execution time (sec)	Required values to store in memory
EKF	5	1.65	42
PF, $N = 50$	252	7.66	2529
PF, $N = 100$	502	14.06	2679
PF, $N = 300$	1502	32.14	3279

When estimating RUL using the PF, the number of particles is varied to find if there is an optimal number of particles for this application. No significant impact on accuracy

is found when the number of particles is above 100. As increasing the number of particles can have a significant impact on computational cost, shown in Table 5.8, the insignificant increase in accuracy with more than 100 particles is not a favorable trade-off.

5.2.4 Reduced sampling rate

To reduce the high sampling rate required for an RUL estimate, the peak detector output needs to provide a similar trend for a similar prognosis. The peak detector used, however, only captures the magnitude of the positive peak in the transient response, not the peak-to-peak magnitude. In order to find if the positive peak magnitude is sufficient, an RUL estimate using an EKF with the trend in the positive peak in the leakage current measured from the oscilloscope is compared to the RUL estimate using the peak-to-peak magnitude. Figure 5.10 shows that a prognosis with similar accuracy can be calculated using just the magnitude of the positive peak. The output of the peak detector, therefore, should be able to provide an accurate prognosis.

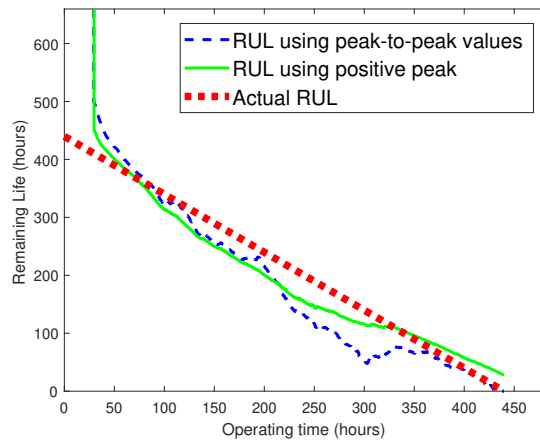


Figure 5.10 Prognosis comparison using peak-to-peak and positive peak magnitude from Machine 2

Trends in the peak-to-peak magnitude, positive peak magnitude and analog circuit output

have a comparable rate of decrease towards the end of life, as shown in Table 5.9. The rate of decrease from the peak detector is similar to that of the positive peak value. RUL estimates using the trends from the peak-to-peak overshoot and the peak detector output result to be similar, as shown in Figure 5.11. Therefore, the output of the peak detector circuit, sampled at a $10x$ lower frequency, is sufficient for insulation failure prognosis.

Table 5.9 Comparison of the rate of decrease from the peak-to-peak trend, positive peak trend and analog circuit output trend for the last 70 hours of life from Machine 4

Peak-to-peak magnitude	Positive peak magnitude	Peak detector output
10.9×10^{-3}	7.9×10^{-3}	7.1×10^{-3}

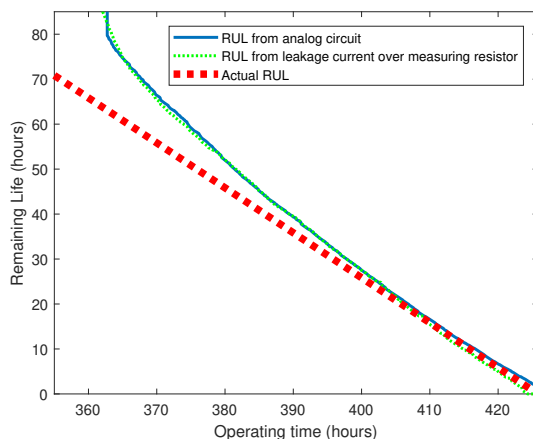


Figure 5.11 Machine 4 RUL from data collected from oscilloscope and analog circuit compared with the actual RUL

5.3 Evaluation of robustness

There are many sources of stress on insulation and any variation between two similar machines can cause the insulation lifetime to vary significantly. The EKF is known to diverge from the true value when measurement data has a significant amount of noise [49]. Three

comparisons are performed to examine robustness of the RUL prediction from the EKF and PF:

1. Errors due to inaccurate training data
2. Varying rate of degradation
3. Variation in insulation system

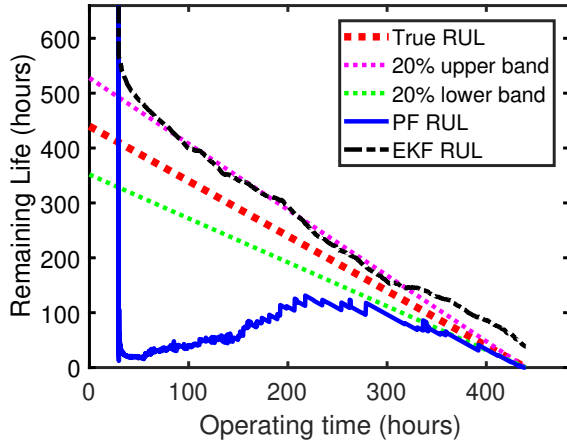
The difference in accuracy of the resulting RUL predictions is compared to evaluate which algorithm is more robust to these three scenarios.

5.3.1 Inaccurate training data

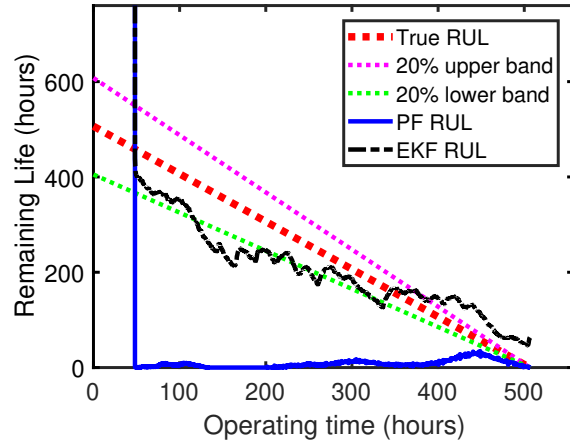
With training data available, it cannot be assumed that all insulation will follow the same degradation trend. After adding an error in the initial parameter estimates, again the EKF provides a more accurate RUL estimate over the entire lifetime as shown in Figure 5.12. The accuracy of the EKF is lower than the accuracy of the RUL produced when accurate training data is available, shown in Table 5.10. The accuracy of the RUL from the PF, however, is similar to the accuracy of the RUL estimate when accurate training data is available.

Table 5.10 Accuracy of RUL estimated using EKF and PF without using accurate training data for Machines 2 and 3

Machine	Algorithm	MSE	R^2	t_{20} (hr)	CI (hr)
2	EKF	3083	98.35	196.8	[460.5, 539.29]
2	PF $N = 50$	35774	0.35	4.7	[68.58, 431.2]
2	PF $N = 100$	36331	0.08	20.7	[69.75, 434.58]
2	PF $N = 300$	35259	0.414	30.83	[68.8, 435.92]
3	EKF	2290	3726	194.25	[391.96, 563.37]
3	PF $N = 50$	67817	40.9	0	[16.2, 115]
3	PF $N = 100$	67806	41.64	0.02	[16.11, 115.45]
3	PF $N = 300$	67797	39.9	0	[16.31, 115.2]



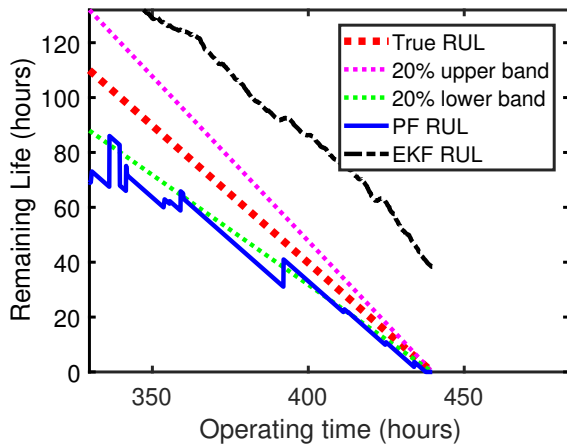
(a) Predicted RUL from EKF and PF compared with actual RUL from Machine 2 when inaccurate data used for training



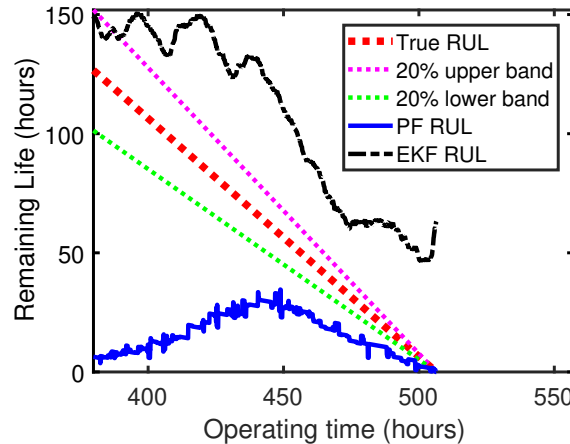
(b) Predicted RUL from EKF and PF compared with actual RUL from Machine 3 when inaccurate data used for training

Figure 5.12 RUL estimated using EKF and PF compared to actual RUL from two sets of experimental data

Towards the actual end of life, the PF is more accurate, shown in Figure 5.13. The EKF now overestimates RUL towards the end of life for Machines 2 and 3. Overestimation is undesired in applications where safety is critical as it leads to unexpected failures.



(a) Predicted RUL from EKF and PF compared with last 25% of actual RUL from Machine 2 when inaccurate data used for training



(b) Predicted RUL from EKF and PF compared with last 25% of actual RUL from Machine 3 when inaccurate data used for training

Figure 5.13 RUL estimated using EKF and PF without accurate training data compared to last 25% of actual RUL with 20% confidence intervals provided

Comparing the accuracy when inaccurate training data is used, in Table 5.11, to the accuracy in Table 5.3 shows that the EKF has a significant decrease in accuracy towards the

Table 5.11 Accuracy of last 25% of RUL estimated using EKF and PF without accurate training data for Machines 2 and 3

Machine	Algorithm	MSE	R^2	t_{20} (hr)	CI (hr)
2	EKF	1895	99.63	0	[478.1, 486.9]
2	PF $N = 50$	341.5	98.44	4.7	[408.25, 433.14]
2	PF $N = 100$	262	97.99	20.7	[413.6, 435.75]
2	PF $N = 300$	320.25	98.04	30.83	[410.25, 437.7]
3	EKF	2217	92.8	0	[538.2, 569]
3	PF $N = 50$	2628	9.0	0	[88.08, 118.78]
3	PF $N = 100$	2626	11.1	0.02	[89.3, 118.45]
3	PF $N = 300$	2615	12.2	0	[88.7, 119.3]

end of life while the accuracy of the PF is maintained.

5.3.2 Varying rate of degradation

In this comparison, the rate of degradation that produced the training data is different than the rate used to degrade the insulation of this machine. As shown in Figure 5.14, when insulation in machines is degraded at different temperatures, the PF is more robust and shows a more accurate RUL estimate over the entire lifetime and towards the end of life.

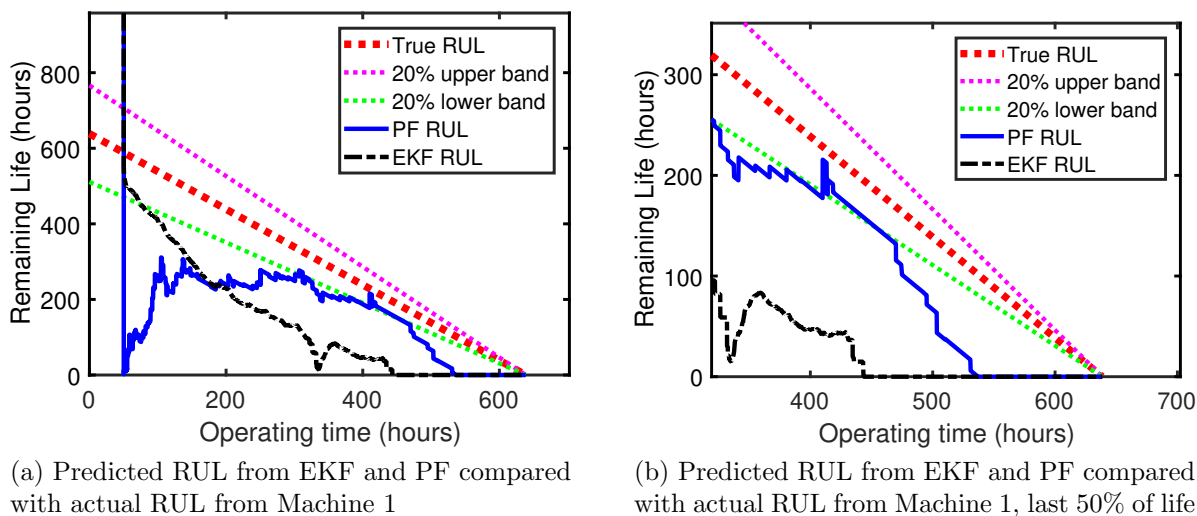


Figure 5.14 RUL estimated using EKF and PF compared to actual RUL of Machine 1 where data sets from Machines 2 and 3 are used for training

Over the entire lifetime, the RUL estimate from the EKF has a lower MSE than the PF, quantified in Table 5.12. However, towards the last half of the insulation lifetime, the PF is significantly more accurate, shown in Figure 5.14b. In this case, where training data is obtained from machines degrading at a higher temperature, the PF is more robust to provide an accurate prognosis towards the end of life.

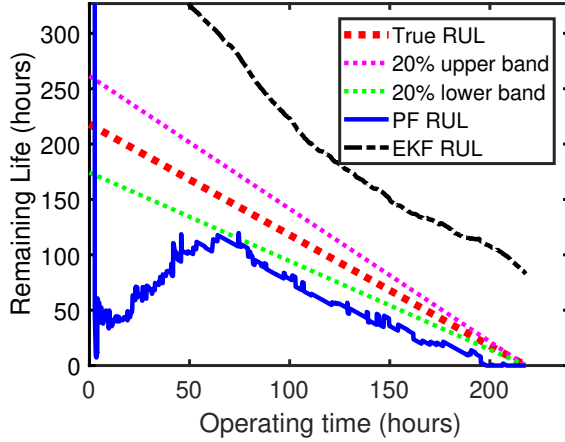
Table 5.12 Accuracy of RUL estimated using EKF and PF for Machines 1 over the whole lifetime and the last 50% of life, where data sets from Machines 2 and 3 are used for training

% of lifetime for calculation	Algorithm	MSE	R^2	t_{20} (hr)	CI (hr)
100%	EKF	29734	86.15	24.75	[413, 608.13]
100%	PF $N = 50$	33804	51.54	55.91	[190.41, 608.6]
100%	PF $N = 100$	33443	50.72	55.17	[184.7, 611.93]
100%	PF $N = 300$	33121	50.87	65.5	[184.4, 616.6]
50%	EKF	21544	69.3	0	[435.3, 624.38]
50%	PF $N = 50$	4019	91.42	55.91	[544.2, 624.38]
50%	PF $N = 100$	3930	91.68	44.7	[542.8, 625.7]
50%	PF $N = 300$	3924	91.48	55.25	[538.9, 624.38]

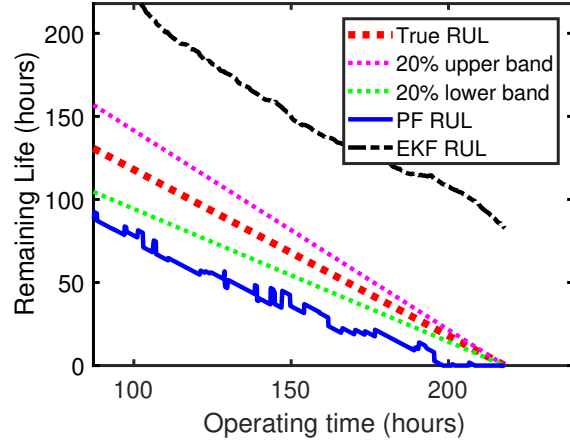
5.3.3 Different insulation system

When the algorithm is trained using data from a machine with a different insulation system and then applied to predict RUL, the PF is again more robust. The PF shows a underestimated RUL initially and converges close to the true RUL while the RUL estimate from the EKF does not converge within 20%, shown in Figure 5.15. Towards the end of life, shown in Figure 5.15b, the EKF is significantly overestimating RUL while the PF slightly underestimates.

In this case, the PF is more accurate than the EKF not only towards the end of life, but over the whole lifetime in Table 5.13.



(a) EKF predicted RUL compared with actual RUL from Machine 5



(b) Predicted RUL from EKF and PF compared with actual RUL from Machine 5, last 60% of life

Figure 5.15 RUL estimated using EKF and PF compared to actual RUL of Machine 5 where data sets from Machines 2 and 3 are used for training

Table 5.13 Accuracy of RUL estimated using EKF and PF for Machine 5 over the whole lifetime and the last 60% of life, where data sets from Machines 2 and 3 are used for training

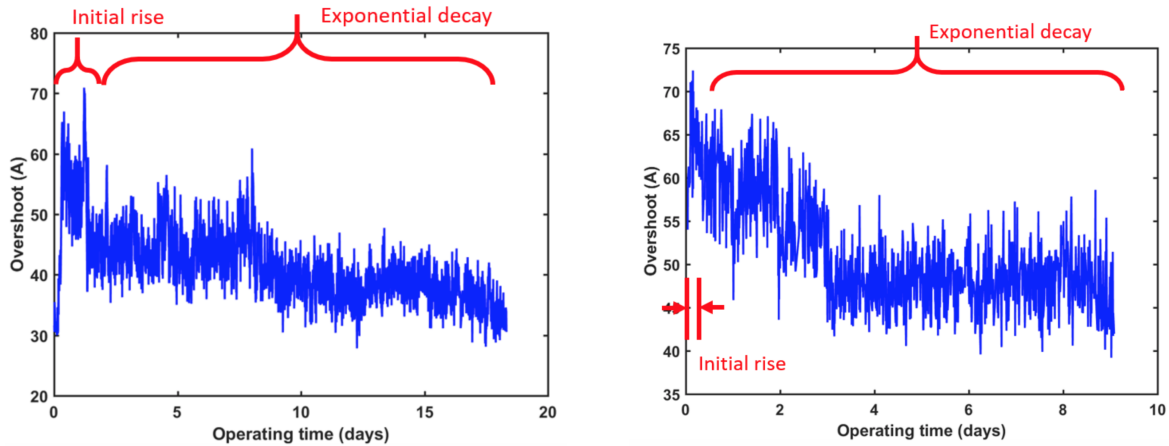
% of lifetime for calculation	Algorithm	MSE	R^2	t_{20} (hr)	CI (hr)
100%	EKF	15176	97.8	0	[299.3, 401.42]
100%	PF $N = 50$	4862	51.91	3.25	[59.75, 208.1]
100%	PF $N = 100$	4830	52.29	0.08	[58.1, 208.41]
100%	PF $N = 300$	4790	51.91	0	[57.58, 201.92]
60%	EKF	8146	98.2	0	[298.8, 328.3]
60%	PF $N = 50$	382.3	85.5	0	[191, 215.5]
60%	PF $N = 100$	328.6	90.5	0	[188.8, 215.5]
60%	PF $N = 300$	347.4	88.2	0	[192.2, 215.5]

5.4 Failure threshold

The trend in leakage current overshoot from the machine with a different insulation system, Machine 5, is different than the trend from the other three data sets used to compare robustness of the algorithms. Data sets from the other three machines follows a trend similar to what is shown in Figure 5.16a: an initial rise from a healthy value to a peak, and then an exponential decay back down near that initial healthy value. Therefore, the failure threshold is set to be when the decaying trend crosses the value of the healthy, initial

overshoot values.

The initial overshoot values from Machine 5, however, are larger in magnitude than the overshoot values towards the end of life, shown in Figure 5.16b. This results in a significant underestimation of lifetime when using the same failure threshold that is used for the other three machines.



(a) Labeled trend in leakage current overshoot from Machine 2

(b) Labeled trend in leakage current overshoot from Machine 5

Figure 5.16 Highlighting the difference in leakage current overshoot trends between two machines with similar ratings and different insulation systems

Instead of using the initial value of overshoot as the failure threshold for Machine 5, the failure threshold is set by assuming a percent decrease from the peak overshoot value. Overshoot trends from the other three machines show that the final overshoot value is 50% lower in magnitude than the peak value, on average. Therefore, for Machine 5, the failure threshold is set to half of the value of the peak in the overshoot magnitude trend.

In this work, leakage current overshoot trends show an initial increase followed by an exponential decay until insulation fails. This initial increase may be due to the applied thermal stress used to accelerate the degradation, as it is also observed in [11]. Under normal operating conditions, this quick increase may not be present, if insulation is degrading from

other sources of stress. Because of this, setting the failure threshold as a percentage of the peak value in leakage current overshoot may be more accurate as the exponential decay is expected to occur as the insulation capacitance decreases with any type of applied stress.

5.5 Proposed prognosis algorithm

As shown in Figures 5.13 to 5.15, the PF gives early false failure indication and the EKF is not always accurate towards the true end of life. In order to provide a prognosis that is more accurate and robust, an algorithm that combines the EKF and PF is proposed.

The algorithm, shown in Figure 5.17, will use the output of the EKF until the PF converges. Convergence is when the current PF RUL estimate is within 1% of the previous two estimates. When the PF converges, there may be a large difference in the EKF and PF estimates. To avoid a sudden step in RUL estimate when the algorithm switches between the EKF and PF, the estimate is slowly ramped between the EKF and PF.

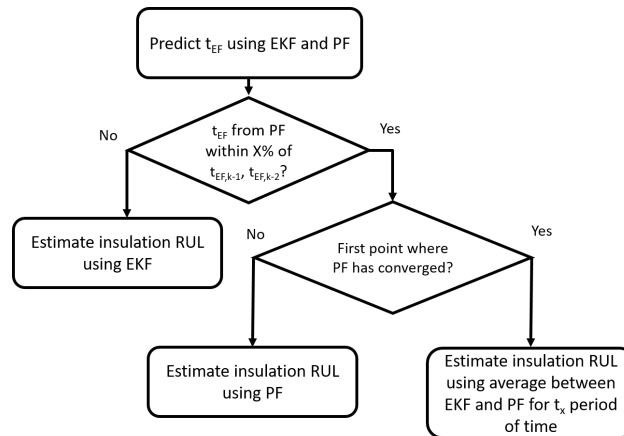


Figure 5.17 Algorithm for the proposed prognosis algorithm where $X\%$ is 1% and t_x is the last two time steps

As shown in Figure 5.18, the proposed algorithm provides an accurate RUL estimate over the entire lifetime even with inaccurate training data. The RUL estimate is accurate,

within 20% of true RUL, at the initial prediction and remains accurate, 40% of true RUL, within the last 100 hours of the end of life without a significant overestimation, as shown in Table 5.14.

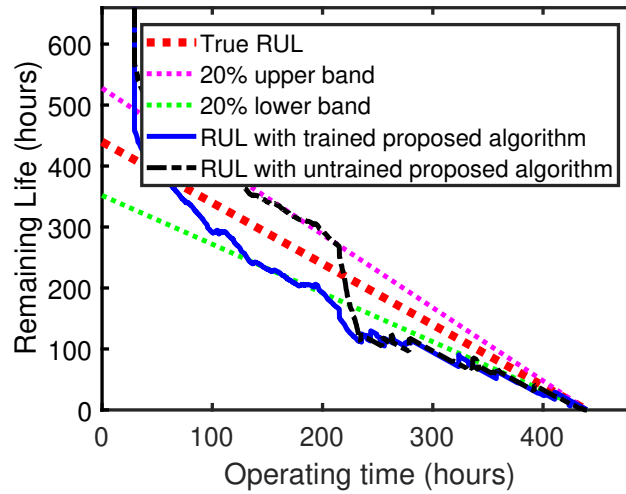


Figure 5.18 Comparison of proposed prognosis algorithm applied to Machine 2 data when accurate training is and is not available used to tune the algorithm

Table 5.14 Accuracy of RUL estimated using EKF, PF and proposed algorithm for Machines 2 with and without accurate training data

Algorithm	Accurate Training Data?	MSE	R^2	t_{20} (hr)	CI (hr)
EKF	Yes	1936	93.5	204.5	[371.75, 452.96]
EKF	No	3083	98.35	196.83	[460.5, 539.29]
PF N=100	Yes	35612	0.3	5.5	[68.9, 433.8]
PF N=100	No	36331	0.08	20.7	[69.75, 434.6]
Proposed	Yes	2103	95	162.08	[20.8, 398.4]
Proposed	No	3413	94.63	123.0	[18.1, 491.3]

As shown in Figure 5.19, the proposed algorithm does not always show a significant improvement when inaccurate training data is used for tuning. Although the PF does not converge until near the time of failure, the overestimation towards the time of failure is reduced. Shown in Table 5.15, the resulting RUL estimate is not significantly improved.

In the case where training data is obtained from machines that degraded at a different rate, the proposed RUL estimation algorithm results in significant improvement in accuracy

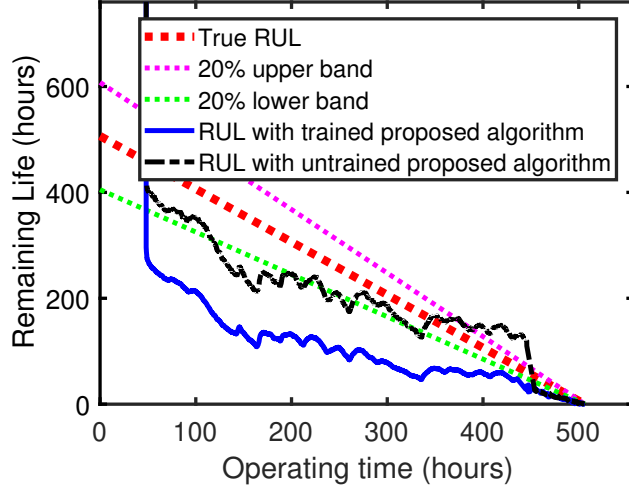


Figure 5.19 Comparison of proposed prognosis algorithm applied to Machine 3 data when accurate training is and is not available used to tune the algorithm

Table 5.15 Accuracy of RUL estimated using EKF, PF and proposed algorithm for Machines 3 with and without accurate training data

Algorithm	Correct Training?	MSE	R^2	t_{20} (hr)	CI (hr)
EKF	Yes	21683	90.0	0	[277.7, 491.6]
EKF	No	3726	91.75	194.25	[392, 563]
PF N=100	Yes	67820	40.15	0	[16.15, 116.2]
PF N=100	No	67806	41.64	0.02	[16.11, 115.45]
Proposed	Yes	21684	90.07	0	[10.81, 236]
Proposed	No	3522	90.86	197	[12.87, 367.7]

over the entire lifetime compared to the estimates in Figure 5.14a, shown in Figure 5.20.

Applying the proposed algorithm over the whole lifetime results in a lower MSE and higher t_{20} , shown in Table 5.16.

Table 5.16 Accuracy of RUL estimated using EKF, PF and proposed algorithm for Machines 1 using data sets from Machines 2 and 3 as training

Algorithm	MSE	R^2	t_{20} (hr)	CI (hr)
EKF	29734	86.15	24.75	[413, 608.1]
PF N=100	33443	50.72	55.17	[184.7, 611.9]
Proposed	16628	85.7	80	[1.89, 445.49]

Applying the proposed prognosis algorithm using training data collected from machines

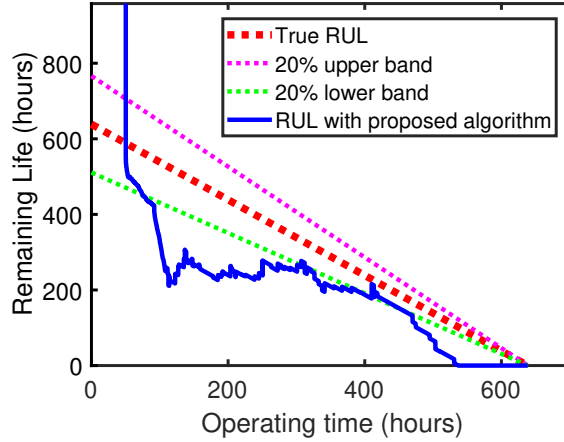


Figure 5.20 Proposed prognosis algorithm applied to Machine 1 using tuning from Machines 2 and 3, where Machine 1 degraded at a different applied temperature

with a different insulation system, shown in Figure 5.21, also shows an improvement in the accuracy of the RUL estimate compared to the those obtained in Figure 5.15a. The MSE obtained is comparable to the results of the PF, but the t_{20} and R^2 are significantly improved, shown in Table 5.17.

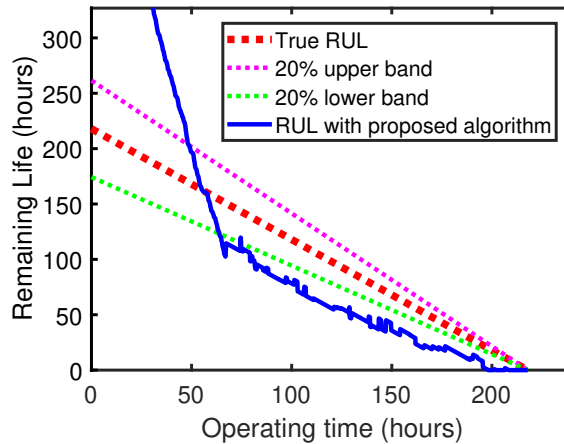


Figure 5.21 Proposed prognosis algorithm applied to Machine 5 using tuning from Machines 2 and 3, where Machine 5 had a different insulation system

The proposed algorithm is shown to improve accuracy of the RUL estimate over the entire life of the insulation. Compared to the EKF and PF algorithms, the proposed algorithm generally results in a lower or comparable MSE while also resulting in a high R^2 and t_{20} .

Table 5.17 Accuracy of RUL estimated using EKF, PF and proposed algorithm for Machines 5 using data sets from Machines 2 and 3 as training

Algorithm	MSE	R^2	t_{20} (hr)	CI (hr)
EKF	15176	97.8	0	[299.3, 401.42]
PF N=100	4830	52.29	0.08	[58.07, 208.4]
Proposed	5800	80.1	15.25	[0.7, 387.7]

The proposed algorithm also maintains robustness as it uses the output of the PF towards the true end of life. It is shown to converge close to the true RUL when training data is inaccurate, obtained from insulation degraded at a different rate or obtained from a machine with a different insulation system.

Chapter 6

Fault Separation

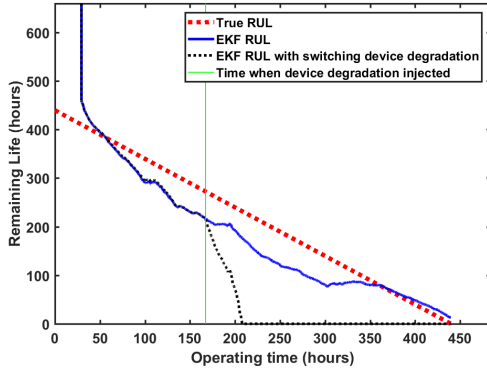
Gate oxide degradation, leads to a significant decrease in leakage current overshoot. This effect may cause underestimation of insulation RUL. Degradation of switching devices has also been shown to cause a change in the harmonic content of the current at the switching transient [5]. The insulation degradation detection method developed in [26, 27] relies on harmonic content at the switching transient to monitor insulation health. As a result, these two features, the overshoot magnitude and harmonic content in the current, can only be used to monitor insulation health with an assumption of healthy inverter switching devices.

A decrease in the overshoot magnitude is observed when gate oxide degradation occurs in a MOSFET, Tables 4.6 and 4.7. Such a decrease in overshoot magnitude results in a significant underestimation of RUL, shown in Figure 6.1.

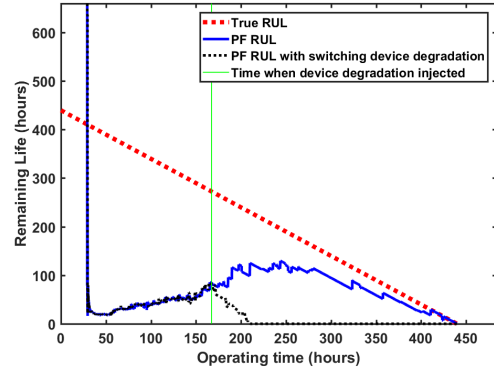
The change in overshoot magnitude from gate oxide degradation may vary across different switching devices; however, any change in overshoot magnitude that is caused by the switching device will lead to a significant underestimation insulation of RUL, shown in Figure 6.2.

6.1 Proposed technique for fault separation

An algorithm to improve robustness of the insulation RUL estimate checks if the change in overshoot is due to insulation degradation or switching device gate oxide degradation prior

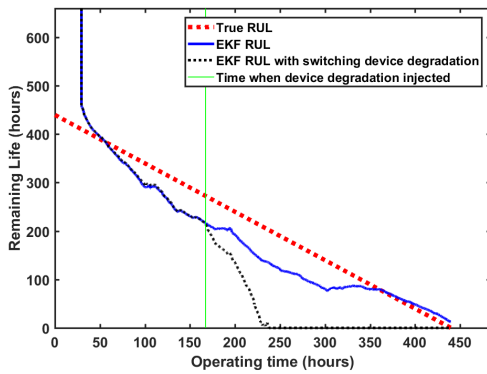


(a) Comparing RUL estimate using EKF when a 30% decrease in overshoot magnitude injected into the data set from Machine 2 to mimic the effect of a degraded switching device

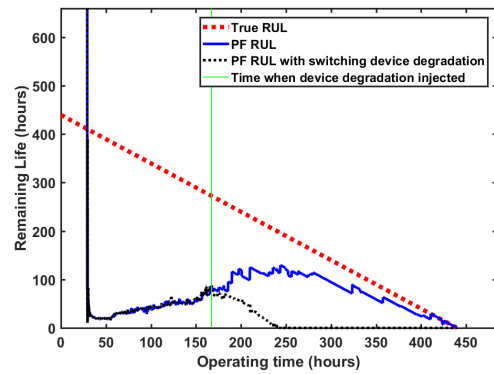


(b) Comparing RUL estimate using PF when a 30% decrease in overshoot magnitude injected into the data set from Machine 2 to mimic the effect of a degraded switching device

Figure 6.1 Effect that degrading switching device has on the RUL estimates from the EKF and PF



(a) Comparing RUL estimate using EKF when a 20% decrease in overshoot magnitude injected into the data set from Machine 2 to mimic the effect of a degraded switching device



(b) Comparing RUL estimate using PF when a 20% decrease in overshoot magnitude injected into the data set from Machine 2 to mimic the effect of a degraded switching device

Figure 6.2 Effect injecting a 20% decrease in overshoot magnitude has on the RUL estimates from the EKF and PF. 20% is lower than the decrease that was found experimentally, and also shows a significant underestimation in RUL.

to RUL estimation, as shown in Figure 6.3. It also calculates an RUL estimate that is robust to error in initial estimates, change in rate of degradation or change in the insulation system.

When a decrease in leakage current is observed, an additional check of the SVPWM duty cycles is made in order to determine if the inverter switching devices are contributing to the leakage current, shown in Figure 6.3a. If not, it is assumed that the insulation is degrading

and the proposed prognosis algorithm is executed to predict RUL. If there is a significant change in SVPWM duty cycles, it is assumed that a switching device is degrading and the insulation is assumed to remain in its current health state.

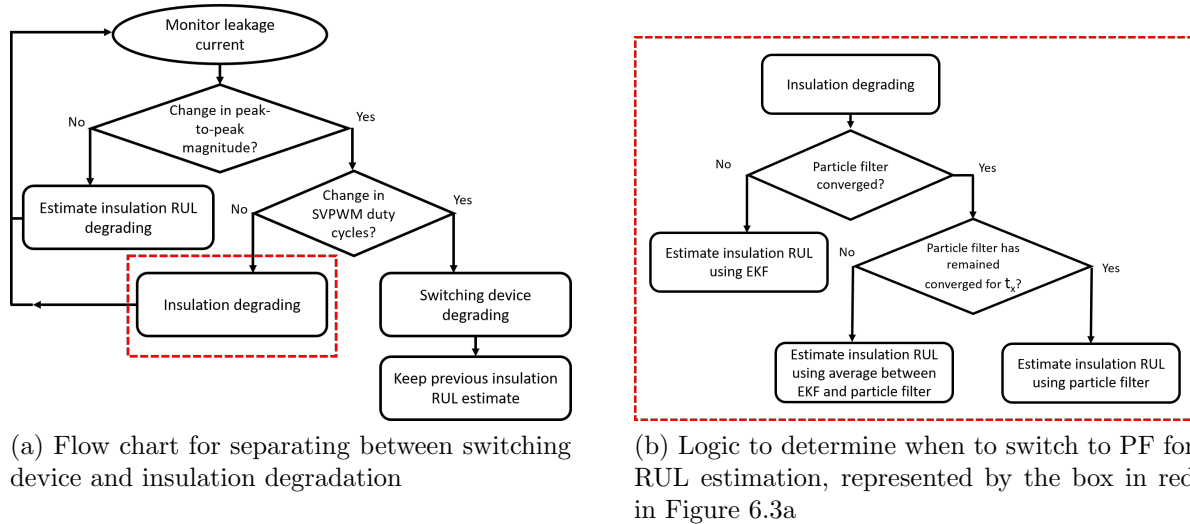
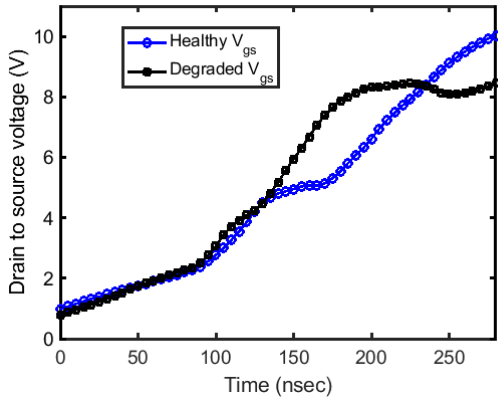


Figure 6.3 Proposed technique to improve the robustness of the insulation failure prognosis

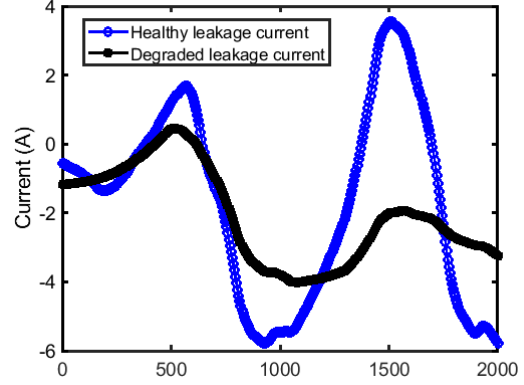
RUL estimation in the proposed algorithm is performed only using the overshoot magnitude of the leakage current, SVPWM duty cycles are only used to confidently determine if the change in leakage current overshoot is due to switching device degradation or not.

Results from accelerated degradation tests show that overshoot magnitude changes with both gate oxide degradation and insulation degradation but only gate oxide degradation produces a change in SVPWM duty cycles. Results show a decrease in the Miller plateau voltage and in the leakage current overshoot as a MOSFET experienced accelerated gate oxide degradation, shown in Figure 6.4. If there is a decrease in leakage current due to the gate oxide degradation, an increase in the Miller plateau voltage occurs. The increase in threshold voltage occurs as the Miller plateau voltage increases, which leads to the increase in current rise delay and change in SVPWM duty cycles.

Accelerated insulation degradation experiments are performed using a switching device



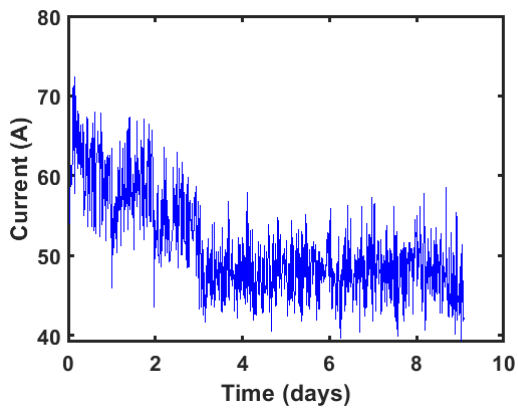
(a) Leakage current overshoot where insulation impedance remained constant and switching device degraded



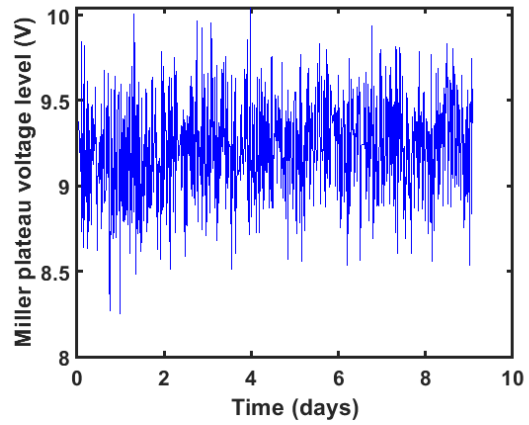
(b) V_{gs} from degraded switching device shows increase in Miller plateau

Figure 6.4 V_{gs} from degraded switching device shows increase in Miller plateau as leakage current decreases

to pulse DC voltage across the insulation. The resulting leakage current overshoot shows a rise followed by an exponential decay. During an experiment, the V_{gs} of the switching device is recorded to show that the leakage current decreases and no significant increase in the Miller plateau voltage occurs, shown in Figure 6.5. This indicates that insulation degradation does not affect the switching device characteristics and does affect the leakage current. Therefore, using the proposed change in SVPWM duty cycles to detect switching device degradation is a robust technique to determine if the switching device contributes to any change in the leakage current overshoot.



(a) Leakage current overshoot trend from Machine 5 as thermal stress is applied to the insulation



(b) Measured Miller plateau voltage in V_{gs} of the device that is applying voltage to the insulation of Machine 5 as it experiences accelerated thermal degradation

Figure 6.5 Switching device applying voltage across insulation of Machine 10 shows no significant change in Miller plateau voltage while the leakage current overshoot rises and decays, indicating that a healthy device and degraded insulation is present

Chapter 7

Conclusion and Future Work

Stator insulation prognosis can be effectively performed using leakage current overshoot magnitude as a feature of insulation degradation and a combination EKF and PF to predict RUL. To improve confidence in the RUL estimate, insulation degradation can be isolated from inverter switching device degradation even though degradation of each component results in a similar change in leakage current overshoot.

Techniques proposed in this work for detecting insulation degradation and switching device degradation can each be performed online, at a reduced sampling rate and without additional sensors. With current sensors on all phases, leakage current is shown to be measurable online. An analog peak detector circuit is implemented during accelerated degradation testing and the output shown to provide sufficient information for an insulation failure prognosis at a reduced sampling rate. Gate oxide degradation in inverter switching devices is detectable using features in the leakage or phase currents. In a current-controlled machine, the increase in phase current delay caused by gate oxide degradation is fed back to the controller and results in a change in voltage commands. As voltage commands are available in the controller, online detection of gate oxide degradation is possible without additional sensors while only sampling at the controller's main calculation loop rate.

As switching device degradation and insulation degradation lead to a similar decrease in the leakage current overshoot, monitoring the steady-state voltage commands is proposed to distinguish when switching device degradation is present. Accelerated degradation of

insulation and switching devices shows that only switching device degradation produces a change in the commanded voltages while insulation degradation does not. Separating between these two faults decreases the likelihood of a false positive detection of insulation failure.

Leakage current overshoot trends collected from accelerated insulation degradation are used to develop a prognosis technique. Applying the PF to these trends resulted in an early indication of insulation failure while the RUL prediction from the EKF is not always accurate towards the end of life. Therefore, an algorithm that uses the prediction of the EKF initially and then transitions to use the PF is proposed for RUL estimation. The proposed algorithm is shown to be robust to varying rates of degradation, variations in insulation system and inaccurate training data. Using the proposed degradation detection and fault separation techniques, an online insulation failure prognosis is possible and can be made more robust with the proposed RUL prediction algorithm.

Future work includes developing an online switching device failure prognosis method. A change in SVPWM duty cycle commands is proposed as the feature of degradation. Further work can use this feature to develop a protocol for RUL estimation which includes defining the behavior model, measurement model and failure threshold that are required for prognosis. The turn-off transient characteristics of the switching device can also be explored for condition monitoring and prognosis.

Accelerated degradation tests of electric machine insulation can be improved. This work used a high temperature to degrade insulation. Other works, however, discuss how insulation properties degrade differently when at different temperatures and that the Arrhenius model is not true for all materials [11]. Changes in the chemical composition and how it affects the insulation properties are unknown, but these changes lead to a change in the electrical

impedance of the insulation material. Detailed rationale for the connection between applied stress and the change in the electrical model for insulation degradation is also future work.

Additional future work includes improving the thermal degradation experimental setup and procedure. Testing relied on visual inspection of insulation to detect defects; however, visual inspection could not determine if insulation is missing has defects within the coil bundles or inside the stator slots. Only the end winding conductors are visible in the current test setup. Insulation could have failed well before failure was determined, and the defect was not noticed. As a result, the trend in insulation degradation may not accurately show the true trend in leakage current overshoot. Accurate information regarding the design of the machines used for testing including insulation materials used can also be used to help justify the differences in insulation lifetime.

Future work also includes improving the prognosis algorithm. In this work, the RUL estimate is taken from the EKF until the PF has converged. Other techniques to determine which algorithm trust can be developed by assigning weights or a Maximum Likelihood Voting algorithm [60]. The EKF and PF themselves can also be improved upon as there are a number of variations of these algorithms that can be implemented to further improve the accuracy and robustness of the insulation failure prognosis [61].

BIBLIOGRAPHY

BIBLIOGRAPHY

- [1] *DuPont Nomex 410 Technical Datasheet*, DuPont, April, 2016.
- [2] P. Neti, K. Younsi, and M. R. Shah, “A novel high sensitivity differential current transformer for online health monitoring of industrial motor ground-wall insulation,” in *2013 IEEE Energy Conversion Congress and Exposition*, Sep. 2013, pp. 2493–2499.
- [3] J. G. Cintron-Rivera, S. N. Foster, and E. G. Strangas, “Mitigation of turn-to-turn faults in fault tolerant permanent magnet synchronous motors,” *IEEE Transactions on Energy Conversion*, vol. 30, no. 2, pp. 465–475, June 2015.
- [4] S. Choi, M. S. Haque, M. T. B. Tarek, V. Mulpuri, Y. Duan, S. Das, V. Garg, D. M. Ionel, M. A. Masrur, B. Mirafzal, and H. A. Toliyat, “Fault diagnosis techniques for permanent magnet AC machine and drives—a review of current state of the art,” *IEEE Transactions on Transportation Electrification*, vol. 4, no. 2, pp. 444–463, June 2018.
- [5] A. E. Ginart, D. Brown, P. W. Kalgren, and M. J. Roemer, “On-line ringing characterization as a PHM technique for power drives and electrical machinery,” in *2007 IEEE Autotestcon*, Sep. 2007, pp. 654–659.
- [6] J. Pyrhonen, T. Jokinen, and V. Hrabovcova, *Design of Rotating Electrical Machines*, 2nd ed. John Wiley & Sons, INC, 2014.
- [7] G. C. Stone, I. Culbert, E. A. Boulter, and H. Dhirani, *Electrical Insulation for Rotating Machines: Design, Evaluation, Aging, Testing, and Repair*, 2nd ed. John Wiley & Sons, INC, 2014.
- [8] V. Sihvo and J. Pyrhonen, “Steam-resistivity of wire insulating materials,” in *2007 IEEE Lausanne Power Tech*, July 2007, pp. 34–38.
- [9] Y. Li, B. Gao, and J. Unsworth, “Degradation of epoxy insulation under combined high humidity and elevated temperature,” in *Proceedings of 1994 4th International Conference on Properties and Applications of Dielectric Materials (ICPADM)*, vol. 2, July 1994, pp. 752–755 vol.2.
- [10] A. Griffo, I. T. syokhla, and J. Wang, “Lifetime of machines undergoing thermal cycling stress,” in *2019 IEEE Energy Conversion Congress and Exposition (ECCE)*, Sep. 2019, pp. 3831–3836.

- [11] D. Kavanagh, K. Gyftakis, and M. McCulloch, “Early-onset degradation of thin-film magnet wire insulation for electromechanical energy converters,” in *2019 IEEE 12th International Symposium on Diagnostics for Electrical Machines, Power Electronics and Drives (SDEMPED)*, Aug 2019.
- [12] N. Lahoud, M. Q. Nguyen, P. Maussion, D. Malec, and D. Mary, “Lifetime model of the inverter-fed motors secondary insulation by using a design of experiments,” *IEEE Transactions on Dielectrics and Electrical Insulation*, vol. 22, no. 6, pp. 3170–3176, December 2015.
- [13] C. Zoeller, T. M. Wolbank, and M. A. Vogelsberger, “Inverter-fed drive stator insulation monitoring based on reflection phenomena stimulated by voltage step excitation,” in *2016 IEEE Energy Conversion Congress and Exposition (ECCE)*, Sep. 2016, pp. 1–8.
- [14] Infineon. (2015, January) IRFB812PbF HEXFET Power MOSFET. [Online]. Available: <http://www.infineon.com/cms/en/product/power/power-mosfet/20v-300v-n-channel-power-mosfet/120v-300v-n-channel-power-mosfet/IRFB812/>
- [15] M. Toudji, S. Duchesne, and G. Parent, “Predictive diagnostic based on HF modeling of electrical machines windings,” in *2019 IEEE International Electric Machines Drives Conference (IEMDC)*, May 2019, pp. 901–906.
- [16] S. Grubic, J. M. Aller, B. Lu, and T. G. Habetler, “A survey on testing and monitoring methods for stator insulation systems of low-voltage induction machines focusing on turn insulation problems,” *IEEE Transactions on Industrial Electronics*, vol. 55, no. 12, pp. 4127–4136, Dec 2008.
- [17] —, “A survey of testing and monitoring methods for stator insulation systems in induction machines,” in *2008 International Conference on Condition Monitoring and Diagnosis*, April 2008, pp. 196–203.
- [18] M. Riera-Guasp, J. A. Antonino-Daviu, and G. Capolino, “Advances in electrical machine, power electronic, and drive condition monitoring and fault detection: State of the art,” *IEEE Transactions on Industrial Electronics*, vol. 62, no. 3, pp. 1746–1759, March 2015.
- [19] A. Bhure, E. G. Strangas, J. Agapiou, and R. M. Lesperance, “Partial discharge detection in medium voltage stators using an antenna,” in *2017 IEEE 11th International Symposium on Diagnostics for Electrical Machines, Power Electronics and Drives (SDEMPED)*, Aug 2017, pp. 480–485.

- [20] H. Kim, T. Kong, S. B. Lee, T. . Kang, N. Oh, Y. Kim, S. Park, and G. C. Stone, “Experience with stator insulation testing and turn/phase insulation failures in the power generation industry,” in *2017 IEEE 11th International Symposium on Diagnostics for Electrical Machines, Power Electronics and Drives (SDEMPED)*, Aug 2017, pp. 21–30.
- [21] P. Zhang, K. Younsi, and P. Neti, “A novel online stator ground-wall insulation monitoring scheme for inverter-fed AC motors,” *IEEE Transactions on Industry Applications*, vol. 51, no. 3, pp. 2201–2207, May 2015.
- [22] J. Yang, J. Cho, S. B. Lee, and J. Yoo, “An advanced stator winding insulation quality assessment technique for inverter-fed machines,” in *Conference Record of the 2006 IEEE Industry Applications Conference Forty-First IAS Annual Meeting*, vol. 3, Oct 2006, pp. 1562–1569.
- [23] V. P. Metelkov, M. Y. Borodin, K. A. Kondakov, and K. E. Nesterov, “Method for monitoring the condition of the motor winding insulation,” in *2018 17th International Ural Conference on AC Electric Drives (ACED)*, March 2018, pp. 1–4.
- [24] Sang Bin Lee, Jinkyu Yang, K. Younsi, and R. M. Bharadwaj, “An online ground-wall and phase-to-phase insulation quality assessment technique for AC-machine stator windings,” *IEEE Transactions on Industry Applications*, vol. 42, no. 4, pp. 946–957, July 2006.
- [25] I. Tsyokhla, A. Griffo, and J. B. Wang, “On-line condition monitoring for diagnosis and prognosis of insulation degradation of inverter-fed machines,” *IEEE Transactions on Industrial Electronics*, pp. 1–1, 2018.
- [26] P. Nussbaumer, M. A. Vogelsberger, and T. M. Wolbank, “Induction machine insulation health state monitoring based on online switching transient exploitation,” *IEEE Transactions on Industrial Electronics*, vol. 62, no. 3, pp. 1835–1845, March 2015.
- [27] C. Zoeller, M. A. Vogelsberger, and T. M. Wolbank, “Monitoring of thermal degraded AC machine winding insulation by inverter pulse excitation,” in *2016 XXII International Conference on Electrical Machines (ICEM)*, Sep. 2016, pp. 1119–1125.
- [28] I. Tsyokhla, A. Griffo, and J. Wang, “On-line motor insulation capacitance monitoring using low-cost sensors,” in *2019 IEEE Energy Conversion Congress and Exposition (ECCE)*, Sep. 2019, pp. 6996–7003.
- [29] J. Cintron-Rivera, “Fault mitigation in permanent magnet synchronous motors under an internal turn-to-turn failure,” Ph.D. dissertation, 2014, copyright

- Database copyright ProQuest LLC; ProQuest does not claim copyright in the individual underlying works; Last updated - 2019-10-19. [Online]. Available: <http://ezproxy.msu.edu.proxy1.cl.msu.edu/login?url=https://search-proquest-com.proxy1.cl.msu.edu/docview/1527595438?accountid=12598>

- [30] M. Sumislawska, K. N. Gyftakis, D. F. Kavanagh, M. D. McCulloch, K. J. Burnham, and D. A. Howey, "The impact of thermal degradation on properties of electrical machine winding insulation material," *IEEE Transactions on Industry Applications*, vol. 52, no. 4, pp. 2951–2960, July 2016.
- [31] M. Hologne, P. Bevilacqua, B. Allard, G. Clerc, H. Morel, H. Razik, A. Barrière, V. Karode, and N. Devadass, "An experimental approach to the health-monitoring of a silicon carbide MOSFET-based power module," in *2017 IEEE International Electric Machines and Drives Conference (IEMDC)*, May 2017, pp. 1–7.
- [32] J. Liu, G. Zhang, Q. Chen, L. Qi, Y. Geng, and J. Wang, "In situ condition monitoring of IGBTs based on the miller plateau duration," *IEEE Transactions on Power Electronics*, vol. 34, no. 1, pp. 769–782, Jan 2019.
- [33] H. Luo, F. Iannuzzo, and M. Turnaturi, "Role of threshold voltage shift in highly accelerated power cycling tests for SiC MOSFET modules," *IEEE Journal of Emerging and Selected Topics in Power Electronics*, pp. 1–1, 2019.
- [34] U. Karki and F. Z. Peng, "Precursors of gate-oxide degradation in silicon carbide MOSFETs," in *2018 IEEE Energy Conversion Congress and Exposition (ECCE)*, Sep. 2018, pp. 857–861.
- [35] N. Stojadinovic, I. Manic, V. Davidovic, D. Dankovic, S. Djoric-Veljkovic, S. Golubovic, and S. Dimitrijevic, "Effects of electrical stressing in power vdmofets," *Microelectronics Reliability*, vol. 45, no. 1, pp. 115 – 122, 2005. [Online]. Available: <http://www.sciencedirect.com/science/article/pii/S0026271404003786>
- [36] U. Karki and F. Z. Peng, "Effect of gate-oxide degradation on electrical parameters of power MOSFETs," *IEEE Transactions on Power Electronics*, vol. 33, no. 12, pp. 10 764–10 773, Dec 2018.
- [37] T. Azoui, P. Tounsi, P. Dupuy, J. M. Dorkel, and D. Martineau, "Numerical and experimental results correlation during power MOSFET ageing," in *2012 13th International Thermal, Mechanical and Multi-Physics Simulation and Experiments in Microelectronics and Microsystems*, April 2012, pp. 1/4–4/4.

- [38] V. Mulpuri and S. Choi, “Degradation of SiC MOSFETs with gate oxide breakdown under short circuit and high temperature operation,” in *2017 IEEE Energy Conversion Congress and Exposition (ECCE)*, Oct 2017, pp. 2527–2532.
- [39] X. Ye, C. Chen, Y. Wang, G. Zhai, and G. J. Vachtsevanos, “Online condition monitoring of power MOSFET gate oxide degradation based on Miller platform voltage,” *IEEE Transactions on Power Electronics*, vol. 32, no. 6, pp. 4776–4784, June 2017.
- [40] Z. Ni, Y. Li, X. Lyu, O. P. Yadav, and D. Cao, “Miller plateau as an indicator of SiC MOSFET gate oxide degradation,” in *2018 IEEE Applied Power Electronics Conference and Exposition (APEC)*, March 2018, pp. 1280–1287.
- [41] F. Erturk, E. Ugur, J. Olson, and B. Akin, “Real-time aging detection of SiC MOSFETs,” *IEEE Transactions on Industry Applications*, vol. 55, no. 1, pp. 600–609, Jan 2019.
- [42] S. Pu, F. Yang, E. Ugur, C. Xu, and B. Akin, “SiC MOSFET aging detection based on miller plateau voltage sensing,” in *2019 IEEE Transportation Electrification Conference and Expo (ITEC)*, June 2019, pp. 1–6.
- [43] S. Pu, E. Ugur, F. Yang, G. Wang, and B. Akin, “In-situ degradation monitoring of SiC MOSFET based on switching transient measurement,” *IEEE Transactions on Industrial Electronics*, pp. 1–1, 2019.
- [44] Vishay. (2011, March) IRF520,SiHF520 Power MOSFET. [Online]. Available: <http://www.vishay.com/docs/91017/91017.pdf>
- [45] CREE. (2017, March) C3M0280090D Silicon Carbide Power MOSFET C3M MOSFET Technology. [Online]. Available: <https://www.wolfspeed.com/media/downloads/825/C3M0280090D.pdf>
- [46] A. S. Babel and E. G. Strangas, “Condition-based monitoring and prognostic health management of electric machine stator winding insulation,” in *2014 International Conference on Electrical Machines (ICEM)*, Sep. 2014, pp. 1855–1861.
- [47] F. Schemmel, K. Bauer, and M. Kaufhold, “Reliability and statistical lifetime- prognosis of motor winding insulation in low-voltage power drive systems,” *IEEE Electrical Insulation Magazine*, vol. 25, no. 4, pp. 6–13, July 2009.
- [48] J. R. Celaya, A. Saxena, C. S. Kulkarni, S. Saha, and K. Goebel, “Prognostics approach for power mosfet under thermal-stress aging,” in *2012 Proceedings Annual Reliability and Maintainability Symposium*, Jan 2012, pp. 1–6.

- [49] R. K. Singleton, E. G. Strangas, and S. Aviyente, “Extended Kalman filtering for remaining-useful-life estimation of bearings,” *IEEE Transactions on Industrial Electronics*, vol. 62, no. 3, pp. 1781–1790, March 2015.
- [50] G. L. Plett, “Extended kalman filtering for battery management systems of LiPB-based HEV battery packs: Part 3. state and parameter estimation,” *Journal of Power Sources*, vol. 134, no. 2, pp. 277 – 292, 2004. [Online]. Available: <http://www.sciencedirect.com/science/article/pii/S0378775304003611>
- [51] Q. Miao, L. Xie, H. Cui, W. Liang, and M. Pecht, “Remaining useful life prediction of lithium-ion battery with unscented particle filter technique,” *Microelectronics Reliability*, vol. 53, no. 6, pp. 805 – 810, 2013. [Online]. Available: <http://www.sciencedirect.com/science/article/pii/S0026271412005239>
- [52] B. Saha, K. Goebel, and J. Christophersen, “Comparison of prognostic algorithms for estimating remaining useful life of batteries,” *Transactions of the Institute of Measurement and Control*, vol. 31, no. 3-4, pp. 293–308, 2009. [Online]. Available: <https://doi.org/10.1177/0142331208092030>
- [53] D. A. Pola, H. F. Navarrete, M. E. Orchard, R. S. Rabié, M. A. Cerda, B. E. Olivares, J. F. Silva, P. A. Espinoza, and A. Pérez, “Particle-filtering-based discharge time prognosis for lithium-ion batteries with a statistical characterization of use profiles,” *IEEE Transactions on Reliability*, vol. 64, no. 2, pp. 710–720, June 2015.
- [54] A. El Mejdoubi, H. Chaoui, J. Sabor, and H. Gualous, “Remaining useful life prognosis of supercapacitors under temperature and voltage aging conditions,” *IEEE Transactions on Industrial Electronics*, vol. 65, no. 5, pp. 4357–4367, May 2018.
- [55] J. Wang and R. X. Gao, “Multiple model particle filtering for bearing life prognosis,” in *2013 IEEE Conference on Prognostics and Health Management (PHM)*, June 2013, pp. 1–6.
- [56] M. Jouin, R. Gouriveau, D. Hissel, M.-C. Péra, and N. Zerhouni, “Particle filter-based prognostics: Review, discussion and perspectives,” *Mechanical Systems and Signal Processing*, vol. 72-73, pp. 2 – 31, 2016. [Online]. Available: <http://www.sciencedirect.com/science/article/pii/S088832701500504X>
- [57] Y. Hu, P. Baraldi, F. D. Maio, and E. Zio, “A particle filtering and kernel smoothing-based approach for new design component prognostics,” *Reliability Engineering and System Safety*, vol. 134, pp. 19 – 31, 2015. [Online]. Available: <http://www.sciencedirect.com/science/article/pii/S0951832014002439>

- [58] J. Devore, *Probability and Statistics for Engineering and the Sciences*. Belmont, CA: Brooks/Cole Cengage Learning, 2009.
- [59] D. Montgomery, *Design and Analysis of Experiments*. Hoboken, NJ: John Wiley & Sons Inc., 2013.
- [60] Yiu-Wing Leung, “Maximum likelihood voting for fault-tolerant software with finite output-space,” *IEEE Transactions on Reliability*, vol. 44, no. 3, pp. 419–427, Sep. 1995.
- [61] J. Sikorska, M. Hodkiewicz, and L. Ma, “Prognostic modelling options for remaining useful life estimation by industry,” *Mechanical Systems and Signal Processing*, vol. 25, no. 5, pp. 1803 – 1836, 2011. [Online]. Available: <http://www.sciencedirect.com/science/article/pii/S0888327010004218>